THÈSE DE DOCTORAT
DE L'UNIVERSITÉ PIERRE ET MARIE CURIE
PARIS 6

Spécialité :
ÉLECTRONIQUE

Pour obtenir le grade de :
DOCTEUR DE L'UNIVERSITÉ PIERRE ET MARIE CURIE

Présentée par :
François CHAUVET

RÉSEAU D'ANTENNES CONFORME PHASÉ, LARGE BANDE ET BIPOLARISÉ POUR APPLICATIONS RADAR UHF SUR DIRIGEABLE

Soutenue le :
11 janvier 2008

Devant le jury composé de :

Pr. Raphaël GILLARD, INSA de Rennes	Rapporteur
Pr. Odile PICON, Université de Marne la Vallée	Rapporteur
Pr. Victor FOUAD HANNA, Université Pierre et Marie Curie	Examinateur
Pr. Hugh GRIFFITHS, University College London	Examinateur
Dr. Régis GUINVARC'H, Encadrant SONDRA	Examinateur
Pr. Marc HÉLIER, Université Pierre et Marie Curie	Directeur de thèse
M. Marc LESTURGIE, Directeur SONDRA	Invité
Dr. Muriel DARCES, Université Pierre et Marie Curie	Invitée

Remerciements

This work has been led at Sondra (Supélec, Onera, NUS, DSTA, Research Alliance), a French-Singaporean laboratory. First of all, I would like to thanks the DSTA of Singapore for showing a great interest for this work and support for this research. Also, I am very grateful to Lim Kah Bin, the first director of Sondra, to have given me the opportunity to join the SONDRA team. Many thanks to Marc Lesturgie, the current director, for his constant work and all his efforts to build this lab since the beginning . Thanks to Walid Tabarra, the technical manager, for having providing me everything I required for my research.

Merci aux rapporteurs de cette thèse, Raphaël Gillard et Odile Picon pour avoir accepté de relire mon manuscrit et pour l'intérêt qu'ils ont manifesté pour ce sujet dans leurs rapports extrêmements bien écrits et détaillés. Merci également aux autres membres du jury qui ont accepté de juger ce travail, Victor Fouad Hanna, Muriel Darces et en particulier Hugh Griffiths pour sa présence et pour son déplacement depuis l'Angleterre.

Je tiens à exprimer toute ma reconnaissance à Marc Hélier, mon directeur de thèse, pour son soutien constant apporté au cours de cette thèse, pour le partage de ses connaissances ainsi que pour sa grande disponibilité et générosité qui le caractérisent. Il a su me guider tout en respectant mes choix. Cela a été un réel plaisir et un véritable enseignement de travailler à ses côtés.

Un grand merci à Régis Guinvarc'h, mon encadrant SONDRA, qui a su me faire confiance. De nos approches éventuellement divergentes, il a su faire preuve d'écoute et de patience afin de me faire profiter de sa propre expérience. Outre les grommèlements, le verbe minimaliste et son humour subtil, je garderai en mémoire nos formidables discussions passionnées qui ont su rendre ce travail toujours plus motivant tout au long de la thèse.

Je tiens aussi à souligner la contribution des personnes du département EMG (Electromagnétique Supelec) qui, par leur expérience, ont permis de concrétiser le projet de mesures. Merci tout

spécialement à Nicolas Ribière-Tharaud-Hunk, qui a activement participé à cette étape et m'a aidé dans l'utilisation de la base de mesure. Je lui suis également reconnaissant pour les efforts qu'il a consacré à clarifier la "partie calcul de rotation". Un grand merci à Andréa, qui par son enthousiasme et son intérêt, a toujours su être disponible pour délivrer de précieux conseils pour la conception du prototype. Enfin un grand merci à Joël pour le temps consacré à assembler les pièces du prototype. Sans oublier Luc, merci pour ton ineffable sagacité.
J'aimerais maintenant citer et remercier mes collègues de SONDRA qui ont permis que cette expérience de trois ans se déroule dans une ambiance exceptionnelle.
En premier lieu vient Rémi, qui en partageant mon bureau, mon transport et mon quartier a du par la force des choses partager tous les instants de cette aventure. Pour sa patience chaque jour mise à l'épreuve et sa bonne humeur contagieuse, je tiens à le remercier. Cette thèse restera aussi associée à mon autre "frère thésard" avec qui j'ai eu l'immense plaisir de partager les premiers instants de Sondra : Anthony/Tonio. Merci tout simplement à tous les deux, grâce à qui ces années resteront inoubliables.

Merci aux "mamans Sondraliennes" de la première heure. Merci à Anne-Hélène pour son dévouement et son souci du travail bien fait, qui discrètement ont contribué au bon déroulement administratif de cette thèse. Merci à Laetitia, qui par son engagement, sa ténacité et sa rigueur au quotidien, m'ont également guidé et montré un certain exemple.

Merci à tous les autres thésards Sondra; je leur souhaite de poursuivre l'aventure de ce laboratoire à leur manière en gardant la fantastique énergie que j'ai connue pendant ces trois années. Tout spécialement, je remercie Karim, que j'ai eu la chance d'encadrer et former pendant 6 mois afin qu'il poursuive mes travaux. Il a su faire preuve d'une formidable capacité à apprendre et à se passionner rapidement. Je dois également remercier Cyril, qui restera non seulement l'affreux post-doc martyrisé, mais aussi celui avec qui j'ai eu la chance d'avoir des discussions scientifiques ou autres, la plupart aussi interminables qu'instructives. Un petit mot aussi pour Marc Lambert dont l'impertinence inusable pimente avec une touche humoristique le quotidien des personnes qui ont le malheur de le côtoyer.

Je voudrais terminer en remerciant mes parents, qui depuis toujours, ont su m'offrir le soutien et les encouragements qui m'ont permis d'en arriver jusque là.

Enfin, merci à SooYee qui partage ma vie, qui sait comprendre et accepter mes choix. Du début à la fin de thèse, à mes côtés ou à distance, elle a été à chaque moment une source d'inspiration et de stabilité. Je lui dédie cette Thèse.

Résumé étendu

Introduction

De nouveaux types de dirigeables sont actuellement en cours de développement dans plusieurs pays. Ils atteignent des tailles gigantesques (environ 150 m de longueur), comparables à celles des premiers appareils de ce type volant au début du 20^e siècle. Cependant, ces dirigeables n'ayant rien à voir avec leurs ancêtres, volent dans la stratosphère, à 20 km au-dessus du sol. Ils sont connus sous le nom de "dirigeable à très haute altitude" (HAA: High altitude airship). L'hélium a remplacé l'hydrogène, très inflammable, qui était en partie responsable du déclin de ces engins vers le milieu du 20^e siècle. Ces dirigeables de nouvelle génération sont remplis de capteurs de pression et de température, couverts de cellules solaires et peuvent embarquer jusqu'à une tonne de matériel. Ils bénéficient donc d'un fort intérêt en raison de leur potentiel comme plate-forme de télédétection ou de télécommunications, à un coût nettement plus faible que celui des satellites.

Ce fort intérêt, joint au caractère novateur du sujet, a suscité la création d'un programme de recherche entre la France et Singapour. Dans le cadre de SONDRA, nouveau laboratoire franco-singapourien commun à Supelec et à l'ONERA (Office National d'Etudes et de Recherches Aérospatiales) pour la partie France ainsi qu'à NUS (National University of Singapore) et à la DSTA (Defence Science and Technology Agency) pour la partie Singapour, une thèse financée par le DSTA a donc été proposée portant sur la faisabilité de l'utilisation d'une telle plate-forme pour des applications radar, en s'intéressant tout spécialement à la conception du réseau d'antennes. Ce genre de technologie étant encore en plein développement, notre étude s'est focalisée sur des dirigeables commerciaux, utilisés généralement pour de la publicité aérienne. Ces derniers se révèlent moins complexes, de taille plus petite (50 m de long) et ne volent qu'à une centaine de mètres au-dessus du sol.

Pour nos applications, le réseau d'antennes doit fonctionner dans la partie basse de la bande UHF (Ultra Hautes Fréquences). Il doit être utilisé pour la formation de faisceaux, doit être également large bande et doit distinguer la polarisation. À basses fréquences, les dimensions du réseau sont comparables à celles du dirigeable. On choisit donc d'utiliser l'enveloppe du ballon pour poser les antennes. La grande place disponible permet alors de considérer des réseaux de grande taille et

Figure 1: *Le Voliris 900. Dirigeable non rigide ayant servi comme modèle pour notre étude.*

d'avoir une bonne résolution. Cela permet par ailleurs de laisser intacte la structure d'origine du ballon et de s'adapter à des modèles de formes différentes. Le réseau doit respecter l'aérodynamisme du ballon et doit donc épouser la forme du dirigeable. Ce type de réseau est appelé réseau conforme. Sa forme non plane va poser un certain nombre de problèmes de conception et d'analyse qu'il va falloir résoudre. La première difficulté concerne le choix du type d'antennes ainsi que celui de leur positions sur le ballon. La deuxième est lié au calcul du rayonnement d'un tel réseau et une dernière est de trouver la manière d'alimenter les éléments du réseau pour dépointer le diagramme de rayonnement dans différentes directions.

Chapitre 1 : Présentation des domaines abordés

Le premier chapitre donne un certain nombre d'informations sur les différents domaines abordés pour cette étude : les dirigeables, les réseaux conformes et les technologies large bande.

Les dirigeables

Surtout utilisés au début du 20^e siècle, les dirigeables servaient à différentes applications, notamment le transport de passagers. Cependant, en raison de nombreux accidents dont celui du tristement célèbre Hiddenburg en 1937 et également en raison des développements de l'aviation, leur utilisation est devenue maintenant quasi anecdotique. Les dirigeables appartiennent à la famille des "plus légers que l'air". En fonction de leur structure interne, ils peuvent être qualifiés de rigides, semi-rigides et non rigides. Cette dernière catégorie correspond aux ballons utilisés de nos jours. Ils servent de supports publicitaires, mais peuvent aussi être utilisés pour le transport d'objets lourds. Ils peuvent, par ailleurs, accueillir des caméras embarquées pour l'observation ou la retransmission en télévision.

Dans notre application, on considère un dirigeable semblable au Voliris 900 (voir figure 1). Son

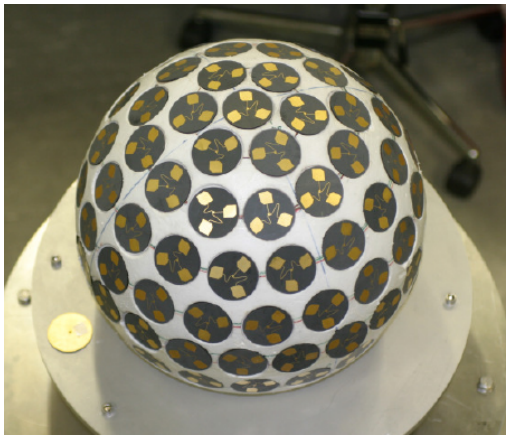

Figure 2: *Exemple de réseau conformé sur une sphère [1].*

enveloppe est remplie d'hélium dont la pression interne est très légèrement supérieure à celle de l'air ambiant. Il faut noter qu'en cas de perforations dans l'enveloppe, l'hélium s'échappera ainsi très doucement, ce qui permettra de voler un moment avant de se poser en toute sécurité. Cette plate-forme est non rigide, ce qui veut dire qu'il y a peu de parties métalliques, hormis la nacelle, les ailerons et d'autres petites pièces d'arrimage. L'enveloppe est très peu épaisse (quelques mm), on considère donc qu'il n'y a pas d'interaction entre le dirigeable et les antennes. Le réseau peut donc être modélisé sans tenir compte de la plate-forme.

Les réseaux conformes

La difficulté réside essentiellement dans la forme non-plane du réseau conforme. Les réseaux conformes suscitent un grand intérêt en raison de leur capacité à être intégrés sur n'importe quelle plate-forme sans la modifier et ont fait l'objet de nombreuses études. On appelle couramment réseau conforme tout réseau non planaire (voir exemple figure 2), c'est-à-dire avec une forme circulaire, sphérique, conique ou d'autre formes canoniques. On peut distinguer deux raisons d'utiliser ce genre de réseaux. La première apparait lorsqu'il n'est pas possible d'utiliser un réseau plan, à cause de contraintes pratiques. La seconde est lorsque l'on souhaite tirer profit des avantages du réseau conforme tels que la possibilité de balayer sur des angles très larges. Le réseau conforme peut aussi être utilisé pour réduire la surface équivalente radar.

Cependant, le réseau conforme est plus complexe que son homologue planaire. Le calcul de ses performances doit prendre en compte non seulement le fait que la structure ne soit pas uniforme, mais aussi l'interaction possible de la plate-forme. La périodicité du réseau ne peut être toujours respectée, surtout dans le cas d'une géométrie à double courbure non développable. Les couplages

sont eux aussi plus difficiles à modéliser du fait de la non homogénéité du réseau. De plus, les éléments ne sont pas tous orientés dans la même direction, ce qui signifie que des éléments sont orientés dans des directions ne contribuant pas au rayonnement principal. En outre, il n'est pas possible de simplifier le calcul en utilisant un facteur de réseau.

Il existe de nombreuses méthodes de calcul développées spécialement pour ce type de réseau. Les avancées technologiques ont permis un accroissement en puissance de calcul et ont ainsi conduit à de grands progrès dans la modélisation des réseaux conformes. De plus, des méthodes approchées ont été dévelopées afin de tenir compte de la plate-forme sur laquelle sont conformées les antennes. Les méthodes numériques traditionnelles ont également été adaptées afin de tenir compte des différents paramètres caractérisant ces réseaux.

Réseaux large bande

Le réseau à conformer sur le dirigeable doit être large bande, c'est-à-dire qu'il doit être composé d'antennes qui puissent avoir les mêmes caractéristique d'impédance et de rayonnement sur une certaine largeur de bande. Cependant, il faut différencier le fonctionnement "large bande", où une antenne rayonne instantanément sur une large bande de fréquences et le fonctionnement "multi-bande", où l'antenne a plusieurs bandes passantes instantanées étroites, comprises dans une bande plus large. Dans notre cas, on se contentera de performances multibandes. Dans la littérature, on trouve un très grand nombre d'antennes large bande. Cependant, les réseaux large bande obéissent à des règles particulières et sont plus difficiles à concevoir dès lors qu'un dépointage de diagramme est nécessaire.

Plusieurs principes sont utiles pour obtenir des performances large bande. Afin de rendre minimale l'énergie réfléchie par l'antenne, on peut utiliser des transitions douces, comme dans le cas des antennes Vivaldi ou biconiques. Les dipôles large bande imprimés, dont l'exemple le plus connu est le "bowtie" [2], sont l'adaptation à deux dimensions de l'antenne biconique et sont très largement utilisés. Des antennes fractales, dont la forme est composée de motifs identiques à plusieurs échelles, ont aussi des performances large bande. Enfin, les antennes auto-complémentaires sont des structures indépendantes de la fréquence faites d'une partie conductrice et d'une partie non conductrice ayant exactement la même forme. Ainsi, leur impédance est toujours égale à une constante théorique d'environ 188.8 Ω selon le principe de Babinet [3]. L'exemple le plus connu est celui de l'antenne spirale.

Le réseau large bande est bien sûr formé d'éléments eux-mêmes large bande. Cependant, la périodicité du réseau réduit la largeur de bande. En effet, afin de dépointer dans tout l'espace sans créer de lobes de réseau, la distance entre éléments doit être inférieure à une demi longueur d'onde. Cela impose donc d'avoir des éléments de petite taille ce qui permet de les rapprocher le plus possible. Néanmoins, la taille de l'antenne doit être suffisamment grande pour rayonner à basse

fréquence. Ces deux conditions sont donc antagoniques. En résumé, il est préférable de choisir des éléments compacts, c'est-à-dire avec une fréquence de rayonnement la plus basse possible pour une taille donnée. Des techniques permettent par ailleurs d'élargir la bande passante du réseau. On peut par exemple utiliser des éléments dont la direction principale de rayonnement est dans le même plan que l'antenne, comme l'antenne Vivaldi. Les éléments n'ont donc pas une largeur contraignant leur insertion dans le réseau. Il est aussi possible d'avoir deux réseaux partageant une même ouverture, avec deux tailles différentes d'éléments fonctionnant donc à deux bandes de fréquences différentes [4]. Le fait d'utiliser des réseaux non périodiques réduit aussi les lobes de réseau et permet d'élargir la bande passante du réseau.

Chapitre 2 : choix du réseau

Le chapitre 2 concerne le choix de l'élément à intégrer dans le réseau et l'emplacement des antennes sur le ballon. Il existe de nombreuses possibilités d'antennes large bande, cependant il faut tenir compte également de la polarisation croisée et de la possibilité d'être conformé sur le dirigeable. En effet, l'élément doit être parfaitement plat et rayonner dans une direction perpendiculaire à son plan. Quatre types d'antennes ont été retenus (voir figure 3) : trois antennes sont des dipôles à large bande qui diffèrent par leur forme et la quatrième antenne est une spirale d'Archimède. On utilise l'outil de modélisation FEKO, basé sur la méthode des moments, afin de caractériser ces antennes et de choisir l'élément le mieux adapté au cahier des charges.

Choix de l'élément de réseau

On évalue tout d'abord la bande passante de chacun des éléments en s'intéressant à la valeur du taux d'onde stationnaire (TOS). Une valeur de TOS inférieure à 2 signifie que l'antenne est bien adaptée et rayonne correctement. Les simulations ont montré que l'antenne spirale et l'antenne QBARC (quadrate bowtie antenna with round corners [2]) ont les meilleures bandes passantes, d'environ 37 % et 19 % respectivement, pour un TOS inférieur à 2.

Les diagrammes de rayonnement obtenus pour les dipôles large bande sont en forme de "donut" avec un rayonnement nul dans leur grand axe de symétrie, tout comme pour un dipôle. L'antenne spirale a elle un diagramme en forme de "huit" en volume, avec deux lobes bien distincts, perpendiculaires au plan et un rayonnement nul dans le plan de l'antenne. On peut donc remarquer que dans une configuration conforme, l'avantage revient au diagramme en "huit" qui possède une symétrie de révolution et rayonne ainsi de manière homogène selon l'angle d'azimut.

L'étude de la polarisation de ces antennes dipôle large bande montre que, dans les plans principaux de polarisations électrique et magnétique des antennes dipôles large bande, la polarisation croisée est quasi inexistante. Ce n'est pas le cas de l'antenne spirale qui n'atteint qu'environ -10 dB.

En revanche, lorsqu'on s'éloigne de ces plans principaux, la polarisation croisée des dipôles large bande remonte fortement et n'a que quelques dB de différence avec la polarisation principale, alors que la spirale maintient un niveau de polarisation croisée inférieur à -10 dB.

En conclusion, on peut remarquer que les antennes de type "bowtie" et tout spécialement la QBARC s'intègrent mieux dans un réseau bi-polarisé car leur forme permet un pavage compact intégrant les deux types de polarisation. L'antenne spirale ne rayonne qu'un seul type de polarisation par côté, ce qui nécessite d'utiliser au moins deux réseaux de spirales : un pour la polarisation droite et l'autre pour la gauche. Le réseau total occupe donc une surface deux fois plus grande. Toutefois, la surface disponible n'étant pas un facteur limitant et la polarisation étant par contre un paramètre important, on choisit l'antenne spirale pour constituer le réseau.

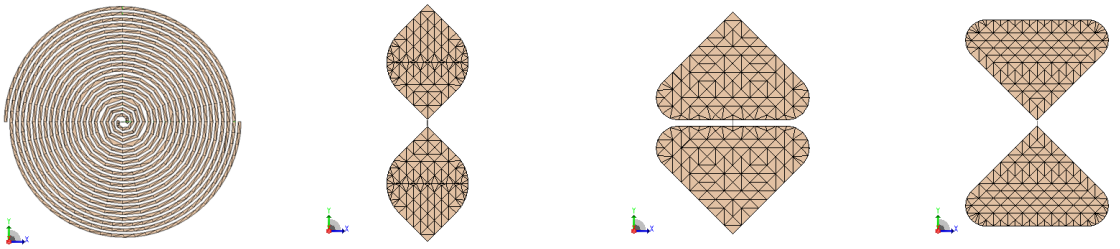

(a) Spirale. (b) (QBARC). (c) (ITBARC). (d) (TBARC).

Figure 3: *Antennes considérées pour le choix de l'élément de réseau*

Fabrication et mesure d'une antenne spirale

Afin de valider les résultats obtenus par simulation, on réalise une antenne spirale pour effectuer des mesures. Neuf exemplaires ont été donc fabriqués et huit seront mis à part pour former un réseau courbé. La conception de l'antenne est réalisée à l'aide d'un logiciel de CAO (Computer Aided Design) avant impression sur un substrat (voir figure 4(a)). L'antenne spirale doit être alimentée de manière symétrique et adaptée sur 200 Ω, alors que le câble d'alimentation est asymétrique et adapté sur 50 Ω. On utilise alors un transformateur qui assure à la fois la symétrisation et l'adaptation d'impédance. L'antenne est ensuite mesurée en chambre anéchoïque. L'antenne rayonne des deux côtés à la fois (voir figure 4(b)) et le câble d'alimentation perturbe donc les caractéristiques de l'antenne. Il est important de garder le câble aussi perpendiculaire que possible par rapport au plan de l'antenne afin de limiter son influence.

Les mesures de S_{11} montrent que l'antenne fabriquée souffre de réflexions plus importantes que prévues par la modélisation. Ces réflexions pourraient être dues à l'ajout du transformateur dont le coefficient de réflexion atteint quelques dB. La dispersion entre les différentes antennes mesurées

est acceptable : environ 1 dB en amplitude et quelques degrés en phase. Les mesures de gain sont effectuées pour une antenne. Quelques dB de différence apparaissent par rapport à la simulation, ce qui correspond aux caractéristiques du transformateur utilisé.

Enfin, les diagrammes de rayonnement de chacune des antennes sont mesurés à plusieurs fréquences, pour les deux polarisations. On remarque que, dans la plupart des cas, la forme du diagramme est reconstruite, même si des perturbations importantes apparaissent, dues à la présence du câble. On retrouve aussi les propriétés de polarisation de la spirale.

Les mesures ont donc bien confirmé les résultats de modélisation avec des valeur proches. La présence du câble et du transformateur sont des éléments très perturbateurs qui dégradent les performances de l'antenne.

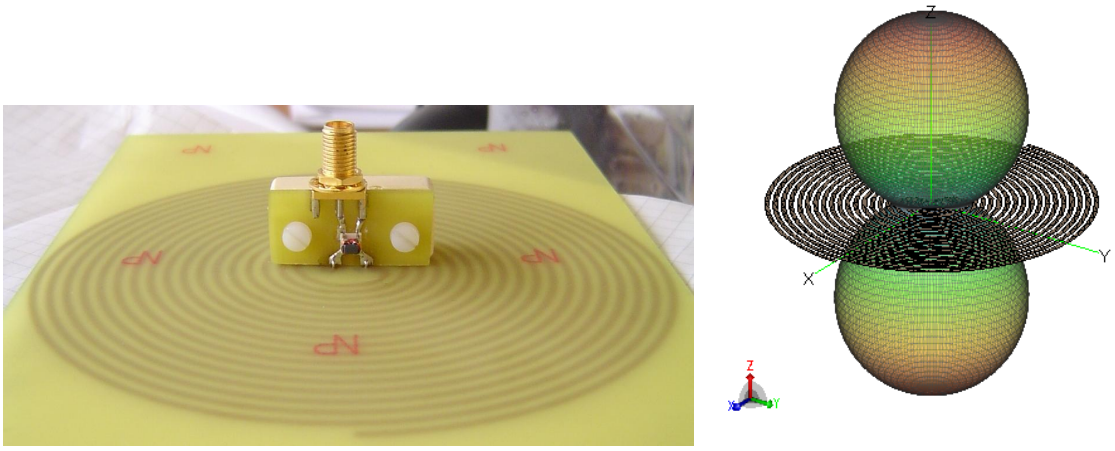

(a) Prototype de l'antenne spirale, intégrant le transformateur. (b) Diagramme de rayonnement simulé de l'antenne spirale.

Figure 4: *Antenne spirale réelle et antenne simulée.*

Solutions d'excitation coplanaire

Les mesures ont mis l'accent sur un problème fondamental lié à la réalisation pratique d'un réseau d'antennes spirales sur dirigeable : l'alimentation. En effet, il n'est pas question de faire passer des câbles à l'intérieur du ballon, ni au dessus des antennes, ce qui les empêcherait de rayonner correctement.

La solution pourrait alors venir de l'optique qui n'interagit pas avec les antennes hormis le boîtier du composant assurant la conversion. Le signal délivré par chaque antenne serait échantillonné, converti en signal optique, puis acheminé dans la nacelle pour être traité. Cependant tout ceci doit

être réalisé localement au centre de l'antenne et impose donc une miniaturisation difficile à réaliser en pratique.

Müller et Sarabandi [5] ont proposé une solution très intéressante, où la spirale est alimentée par l'extérieur des bras (voir figure 5(a)). Cela permet de rester dans le plan de l'antenne et d'y accéder facilement. La conversion optique pourrait alors être faite à l'extérieur de la spirale. Ce type d'antenne a donc été étudié dans le cadre du stage de Master de Karim Louertani [6].

Néanmoins, l'étude de cette antenne montre que sa limite basse en fréquence est plus haute que la fréquence maximale autorisée par le réseau. Cette solution fonctionne donc très bien si l'antenne est utilisée toute seule ou lorsque le réseau ne dépointe pas. De plus, le diagramme de rayonnement et la pureté de polarisation sont fortement dégradés.

L'analyse de la répartition de courant sur l'antenne montre qu'à haute fréquence le courant se situe en périphérie de l'antenne (voir figure 5(a)), alors que pour une antenne excitée au centre, le courant se situe au milieu de l'antenne. De plus, la longueur de piste est différente selon le bras, ce qui signifie que les courants ne parcourent pas la même longueur avant d'arriver au centre. La symétrie de rotation est brisée par cette nouvelle forme et le fonctionnement en est perturbé.

Sachant que les courants symétriquement opposés doivent se retrouver en phase pour qu'il y ait un rayonnement, on cherche à modifier la géométrie de l'antenne. Ainsi, une antenne à quatre bras préservant la symétrie de rotation est proposée (voir figure 5(b)). Lorsque le mode d'excitation est bien choisi, les courants symétriquement opposés se retrouvent en phase et l'antenne peut alors rayonner. Les simulations montrent que cette nouvelle antenne retrouve à une bande passante correspondant à une spirale excitée par le centre. Cependant, son niveau de polarisation croisée est un peu moins bon. Cette nouvelle antenne paraît très prometteuse et permet d'envisager un réseau complètement planaire qui pourrait alors être conformé à la surface du dirigeable.

Cependant, l'antenne spirale classique a été utilisée tout au long de ces travaux, l'antenne à quatre bras n'ayant été conçue que très récemment. Le réseau choisi est un réseau d'antennes spirale de 134 éléments, conformé sur une demi-ellipse avec toutes les antennes orientées de la même façon vers l'extérieur.

Chapitre 3 : Calcul du diagramme de rayonnement du réseau conforme

Le chapitre 3 s'attaque au calcul du diagramme de rayonnement du réseau conforme qui est indispensable pour estimer ses performances. Le logiciel de modélisation ne peut plus être utilisé car le temps de calcul pour tout le réseau serait bien trop long. De plus, il est important de développer un modèle de calcul du diagramme de rayonnement à partir des excitations des antennes. En effet, pour la synthèse de diagramme, ce modèle pourra être utilisé afin de trouver les excitations correspondantes.

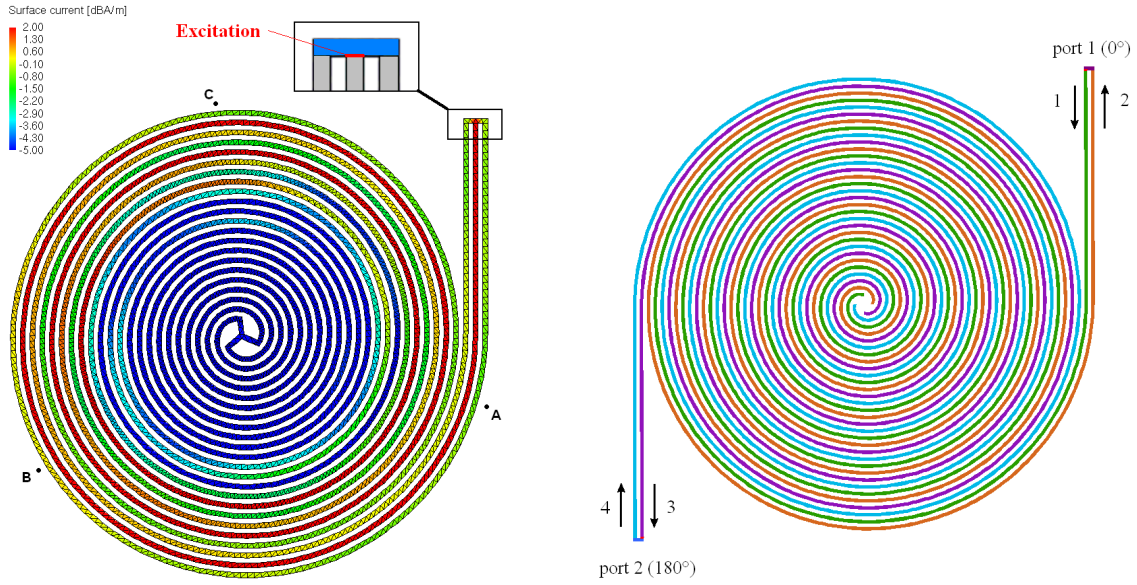

(a) Spirale à 3 bras, à excitation coplanaire [5].

(b) Spirale à 4 bras, à double excitation coplanaire.

Figure 5: *Solutions d'alimentation coplanaire d'une antenne spirale.*

Dans le cas du réseau plan, les antennes ont la même orientation et on peut donc mettre en facteur la caractéristique de rayonnement de l'élément du réseau. Cela revient à faire la somme vectorielle des contributions de chaque antenne du réseau en négligeant les couplages. De la même manière, on propose de sommer la contribution de chaque élément du réseau conforme, tout en tenant compte de l'orientation de chaque élément. Ainsi, il est seulement nécéssaire de modéliser un élément du réseau au lieu des 134.

Dans un premier temps, on étudiera les couplages du réseau afin d'estimer leur influence. Ensuite, on développera une méthode de calcul approchée qui devra être validée par des mesures.

Estimation du couplage

On peut distinguer plusieurs zones dans le réseau considéré (voir figure 6) et également plusieurs types de couplage : entre éléments face à face (zone A avec zone B), entre éléments côte à côte avec faible courbure (zone A ou zone B), entre éléments côte à côte avec une forte courbure (zone C). À l'aide du logiciel de modélisation, on cherche à estimer la valeur de ces couplages par la valeur du coefficient de transmission S_{21}. Comme il n'est pas possible de simuler le réseau en entier, des approximations sont faites.

La première approche consiste à considérer un réseau de huit éléments, pour plusieurs courbures

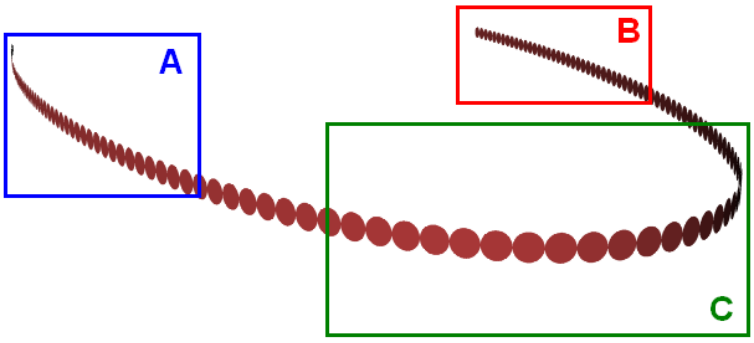

Figure 6: *Réseau formé de 134 antennes spirales, conformé sur une demi-ellipse où on distingue différentes zones de courbure.*

représentant les différentes zones du réseau de 134 éléments. La seconde consiste à remplacer les antennes modélisées en surface par des triangles par des spirales filaires divisées en segments. Ainsi, un réseau de 18 éléments peut être modélisé avec une forme se rapprochant du réseau de 134 éléments si la taille de l'ellipse est réduite. Ces deux types de modélisation montrent que, quel que soit le type de couplage, les valeurs de S_{21} sont inférieures à -10 dB. Il est intéressant de constater que le couplage le plus fort, parmis les trois types de couplages étudiés, est celui entre deux antennes voisines. L'évolution du couplage en fonction de la fréquence est moins simple.

Une étude sur l'influence de la courbure est également réalisée en considérant deux spirales voisines. Deux cas ont étés traités : le premier où les spirales sont orientées de la même façon, le deuxième cas où les spirales ont des polarisations opposées pour une même direction. On constate, pour les deux cas, que le fait d'augmenter la courbure n'augmente que très faiblement la valeur du couplage. En conclusion, les valeurs de couplages étant estimées suffisamment faibles, on le négligera dans la méthode approchée.

Fabrication et mesure du réseau conforme

Deux réseaux de réseau de huit antennes ont été construit avec une courbure différente afin de pouvoir confirmer les résultats de la modélisation. Comme pour la mesure des antennes seules, le problème du positionnement des câbles d'excitation se pose à nouveau. Il faut remarquer que, dans le cas d'un réseau courbé, il n'est pas possible de placer les câbles perpendiculairement au plan des antennes car chacune de ces dernières est dans un plan différent. Le câble ne reste donc perpendiculaire que localement (voir figure 7(b)). La plate-forme en polystyrène (voir figure 7) permet d'assurer une bonne rigidité à l'ensemble du réseau et de contrôler précisément la courbure du réseau et les positions des antennes. On effectue les mesures de réseaux avec une courbure de 5° et de 20°.

De plus, chacune des antennes doit rayonner exactement de la même manière, afin que le réseau réel puisse être comparé au modèle du réseau uniformément excité. Le circuit d'alimentation (voir figure 7(d)) est composé de diviseurs de puissance choisis, entre autres, pour leur faible écart en amplitude et en phase sur les accès de sortie. Ils sont placés en cascade, comme montré sur la figure 7(d), de manière à former huit voies. Les caractéristiques en transmission du réseau d'alimentation sont mesurées à l'aide d'un analyseur de réseau afin de permettre une correction ultérieure, si besoin.

On mesure la matrice de couplage du réseau pour comparer le comportement du couplage avec les résultats donnés par la simulation. Les résultats des mesures sont globalement similaires à ceux de la simulation sur toute la plage de fréquence étudiée. L'odre de grandeur est respecté, excepté pour les antennes voisines où le couplage mesuré est inférieur d'environ 10 dB. Néanmoins, les deux approches montrent que le couplage ne dépasse pas les -10 dB. La présence des câbles et le coefficient de réflexion non négligeable introduisent des perturbations non maîtrisées dans les mesures et dont l'influence est difficile à évaluer.

Par ailleurs, il est intéressant de noter que les valeurs obtenues par la simulation sont données en fonction de valeurs discrètes de la fréquence. En revanche, les mesures permettent d'échantillonner plus finement en fréquence et révèlent l'existence de pics de réflexion et de transmission à certaines fréquences. Ces pics sont caractéristiques des résonances de la spirale. Ainsi, les valeurs données par la simulation doivent être interprétées avec précaution, sachant que la fréquence choisie peut correspondre à une résonance ou au contraire masquer un effet de résonance.

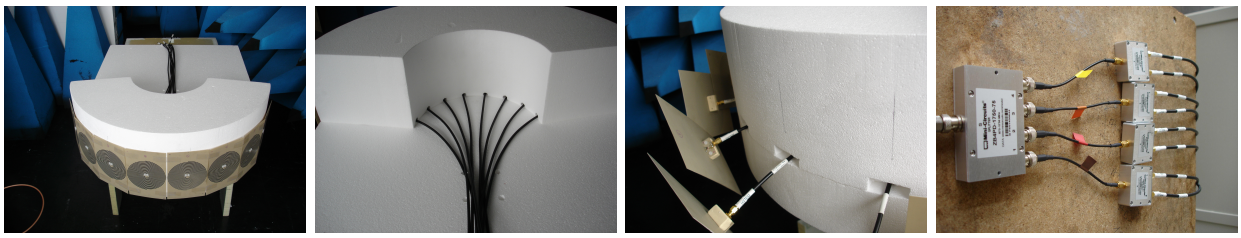

(a) Vue de face. (b) Vue arrière. (c) Détails. (d) Circuit d'alimentation.

Figure 7: *Réalisation du réseau conformé à* 20° *de courbure.*

Méthode approchée

On fait donc l'approximation de couplages suffisamment faibles pour être négligés. Ainsi, le diagramme de rayonnement du réseau conforme peut être calculé en faisant la somme vectorielle des contributions de chaque élément, en y intégrant le décalage de phase dû à la position relative de l'élément. De plus, les éléments n'ayant pas tous la même orientation, on effectue une rotation de chaque élément avant de l'intégrer dans la somme. L'idée est assez simple, cependant, il faut tenir

compte des changements de référentiel et de la nature vectorielle du champ électrique donné dans une base de polarisation qui dépend du logiciel de modélisation.

On distingue le référentiel principal qui est celui du réseau, le référentiel local qui est celui de l'élément et le référentiel de polarisation qui dépend de la direction considérée dans le diagramme de rayonnement. En pratique, on calcule le diagramme de rayonnement de l'élément choisi en utilisant le logiciel de modélisation. Les résultats sont donnés pour chaque direction dans la base de polarisation associée. On effectue ensuite une rotation de la caractéristique de rayonnement selon un angle qui dépend de l'orientation de l'élément dans le repère principal. Cela nécessite donc des passages de coordonnées sphériques à polaires et inversement pour pouvoir effectuer correctement la rotation.

De plus, il est important de remarquer que les directions pour lesquelles sont calculés les champs prennent des valeurs discrètes. Cela signifie, qu'après rotation, les nouvelles directions ne correspondent pas forcément à une direction du diagramme de départ. En conséquence, une technique d'interpolation doit être utilisée.

La méthode approchée qui a été développée permet d'exprimer la caractéristique vectorielle de rayonnement d'une antenne pour n'importe quelle orientation. Il suffit d'avoir modélisé au préalable la caractéristique vectorielle de rayonnement pour une seule orientation.

On mesure donc le diagramme de rayonnement du réseau dans la base de mesure de Supélec, comme montré sur la figure 8. Les résultats obtenus par la méthode approchée sont comparés à ceux des mesures et à ceux de la simulation pour un réseau de huit antennes, à différentes fréquences et à différentes courbures.

On peut voir sur la figure 9 que les résultats de la méthode approchée et ceux de la simulation sont très proches. Le lobe principal est parfaitement reconstruit et le niveau du lobe secondaire est assez bien respecté. La méthode approchée avec corrections utilise les coefficients de transmission du circuit d'alimentation préalablement mesurés. On peut remarquer que ces corrections ne font pas beaucoup varier le diagramme de rayonnement. Les mesures confirment donc la forme du diagramme de rayonnement, même si le diagramme est fortement perturbé par les câbles d'alimentation. De plus, la polarisation est bien respectée dans les mesures. Les résultats donnés par la méthode approchée sont en accord avec les mesures et la méthode exacte ce qui permet de l'utiliser par la suite afin de prédire le comportement du réseau soumis à diverses excitations.

Chapitre 4 : performances du réseau phasé

Le choix de la forme, de l'emplacement et du type de réseau sont décrits dans le Chapitre 2 et une méthode de calcul pour évaluer ses performances a été développée dans le Chapitre 3. Le Chapitre 4 s'intéresse aux possibilités de dépointage du réseau en faisant la distinction entre les polarisations. On cherche donc les jeux d'excitations correspondant à des dépointages différents.

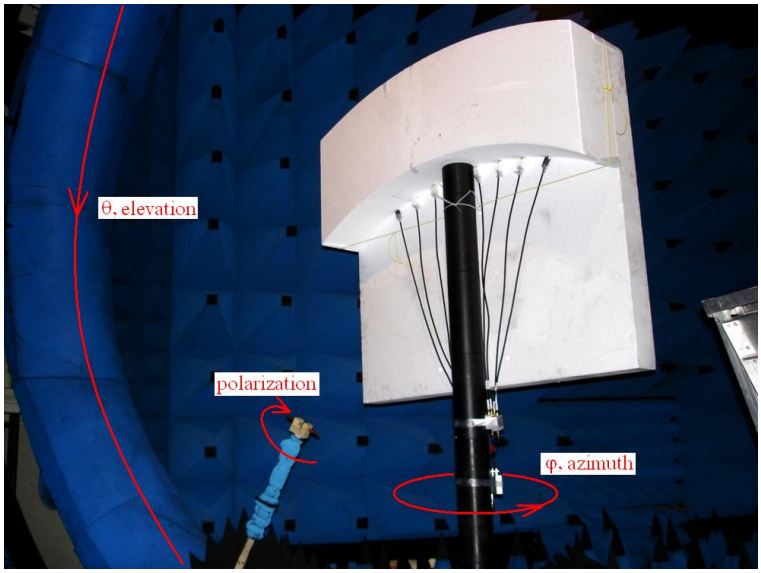

Figure 8: *Réseau à 5° de courbure, mesuré dans la base de mesure de Supélec.*

Après une étude de la configuration du réseau, on utilisera une méthode de synthèse de diagramme, puis les positions des antennes seront optimisées pour former un réseau hétérogène permettant d'améliorer les performances du réseau conforme.

Configuration du réseau

La grande originalité de ce réseau est qu'il n'y a pas de plan de masse ni de plate-forme métallique empêchant le rayonnement à l'intérieur même de la structure. Ceci est tout à fait inhabituel car les antennes sont généralement conformées à une plate-forme rigide, où l'insertion d'un plan de masse est possible, voire il en existe déjà un (voiture, avion, etc.). Il faut donc souligner le fait que peu de supports autorisent les antennes à rayonner dans toutes les directions de l'espace. La conception et le fonctionnement du réseau se trouvent alors considérablement modifiés et les considérations généralement appliquées pour les réseaux plans ne peuvent être qu'en partie transposées.

Concrètement dans notre cas, lorsqu'une antenne est alimentée, il faut à la fois considérer son rayonnement vers l'extérieur mais aussi vers l'intérieur. Des interactions sont alors possibles entre les antennes situées de part et d'autre du dirigeable. Cependant, il a été montré dans le Chapitre 3 que ce type de couplage n'est pas prépondérant.

À cela, il faut rajouter les mécanismes de polarisation qui interviennent dans le fonctionnement du réseau. La polarisation est en effet l'un des facteurs les plus complexes, limitant la conception et l'analyse d'un réseau conforme. En effet, chaque antenne a sa propre orientation et donc sa propre

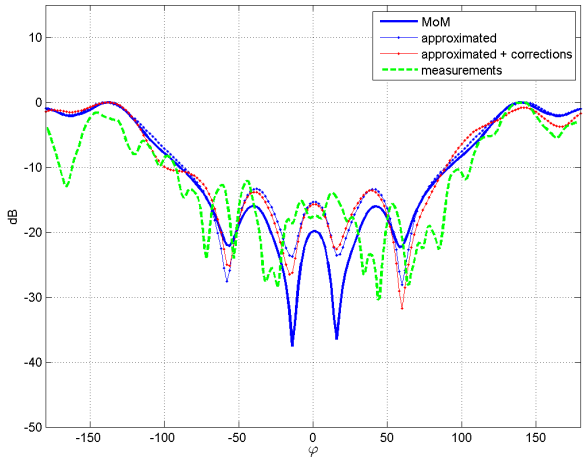

(a) Composante polarisée circulaire gauche.

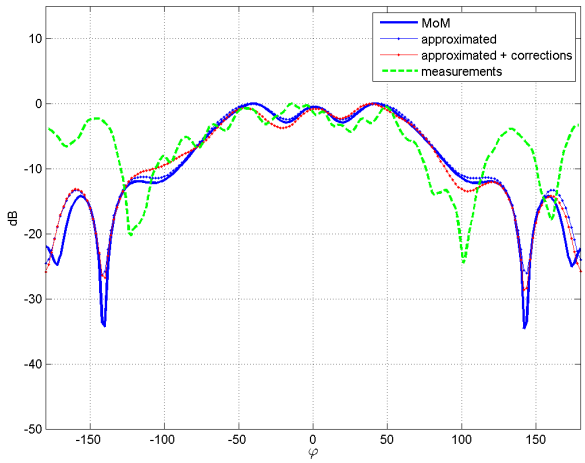

(b) Composante polarisée circulaire droite.

Figure 9: *Comparaisons entre les différentes méthodes. Diagramme de rayonnement à 1200 MHz, pour la courbure de* 20°.

caractéristique de polarisation. Il est donc très difficile de faire contribuer tous les éléments du réseau, sachant que chacun aura sa propre polarisation. L'antenne spirale a justement été préférée pour sa caractéristique de polarisation quasi-homogène sur un demi-espace, ce qui devrait simplifier la gestion de la polarisation. La figure 10 représente la configuration du réseau choisi en rappelant

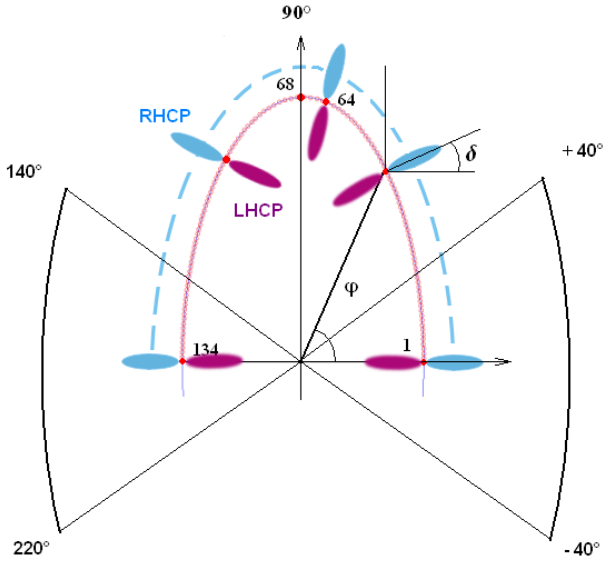

Figure 10: *Configuration du réseau de 134 spirales. Le rayonnement polarisé circulaire droit (RHCP) est représenté en bleu, le rayonnement polarisé circulaire gauche (LHCP) est représenté en rouge.*

la polarisation des éléments. Chaque antenne rayonne ainsi une polarisation circulaire droite à l'extérieur et circulaire gauche à l'intérieur.

On s'intéresse maintenant de plus près aux mécanismes de polarisation intervenant dans le fonctionnement de ce réseau. L'antenne spirale étant un objet chiral, c'est-à-dire non superposable à son image dans un miroir, il en résulte certaines propriétés intéressantes. Une face rayonne un polarisation circulaire droite l'autre un polarisation circulaire gauche.

La figure 11 récapitule les types de polarisations de deux antennes situées sur des faces opposées du ballon. Un rayonnement vers la gauche à $\varphi = 0°$, en polarisation circulaire droite, est possible en utilisant le rayonnement extérieur de l'antenne 2 située à droite. Il est intéressant de noter qu'en utilisant le rayonnement intérieur de l'antenne 1 située à gauche, il est également possible de rayonner une polarisation circulaire gauche, toujours pour la même direction à $\varphi = 0°$. Ainsi, en utilisant à la fois les rayonnements intérieurs et extérieurs de la spirale, une seule ligne d'antennes, conformée sur le tour du dirigeable en demi-ellipse, est suffisante pour avoir les deux polarisations. Cela est vrai si l'on considère les directions perpendiculaires aux flancs du dirigeable, l'extension à d'autres directions reste à démontrer.

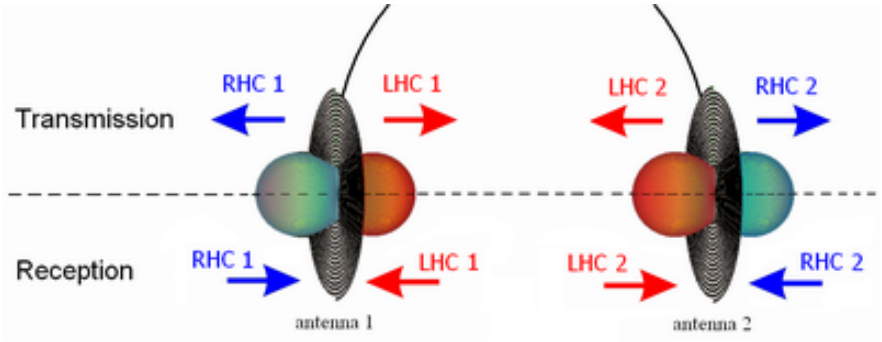

Figure 11: *Récapitulatifs des types de polarisation intervenant dans le réseau.*

Synthèse de diagramme

Afin de trouver les excitations nécessaires pour balayer les différentes directions de l'espace, on utilise une méthode de synthèse de diagramme. Parmi les différentes méthodes existantes, dédiées aux réseaux conformes, on a choisi la méthode des projections alternées (AP) [7]. Cette méthode itérative a déjà fait ses preuves dans plusieurs applications et converge rapidement. Le diagramme réalisable est calculé de la manière suivante : $\mathbf{F}_r(\theta,\varphi) = \sum_{m=1}^{M} \mathbf{a}_m \mathbf{g}_m(\theta,\varphi)$ avec $\mathbf{a}_m$ l'excitation appliquée à l'antenne m. La matrice $\mathbf{g}_m$ prend en compte la caractéristique de rayonnement de l'antenne m après correction de l'orientation et du centre de phase, telle que décrite dans le Chapitre 3. La méthode approchée développée est donc intégrée dans la synthèse de diagramme.

À partir du diagramme réalisable, on construit un diagramme souhaité $\mathbf{F}_d$ en projetant les valeurs de diagramme sur un gabarit prédéfini. Puis on inverse la matrice afin de calculer les excitations $\mathbf{a}_m$ correspondantes suivant : $\mathbf{a}_m = \mathbf{g}_m^{-1}\ \mathbf{F}_d(\theta,\varphi)$. Cela est répété jusqu'à ce que le diagramme réalisable rentre dans le gabarit souhaité.

On utilise donc la méthode AP combinée avec la méthode approchée de calcul de diagramme de rayonnement pour trouver les excitations pour différents angles de dépointage. Les gabarits sont construits de manière à avoir un niveau de lobe secondaire de -25 dB, une largeur de lobe principale de 2°, pour des angles allant de 0 à 360 degrés, par pas de 10°. Le calcul est effectué indépendamment pour chacune des polarisations.

La figure 12 illustre le résultat de cette méthode, en montrant le diagramme polarisé circulaire droit obtenu pour la direction 10°, ainsi que le diagramme de la polarisation croisée associée. On remarque que le niveau de la polarisation croisée atteint jusqu'à -15 dB. La partie droite de la figure 13 montre les positions des antennes qui contribuent le plus à l'obtention de ce diagramme. Pour cela, on trace uniquement la position des antennes dont l'amplitude du coefficient d'excitation correspondant est supérieure à un tiers du maximum. On constate que, comme prévu, une po-

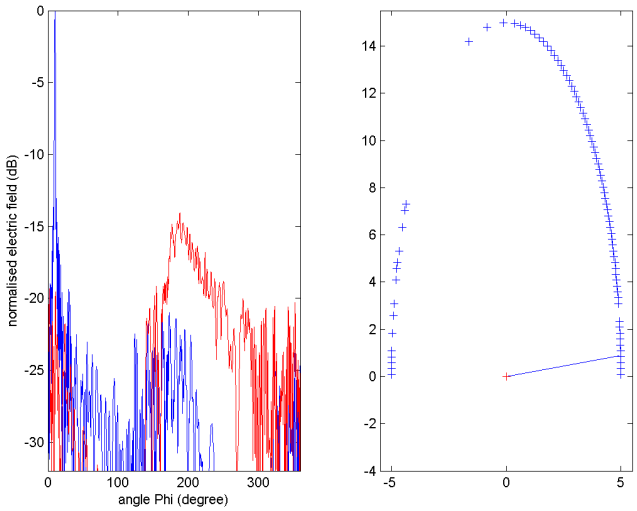

Figure 12: *Diagramme de rayonnement polarisé circulaire droit avec le niveau de polarisation croisée. Optimisation pour un angle de* 10°*. Partie droite : positions des antennes participant le plus au rayonnement.*

larisation circulaire droite provient principalment des antennes situées dans la direction principale de rayonnement. En effet le rayonnement extérieur est utilisé. Des résultats complémentaires ont montré que cela reste vrai dans le cas où un diagramme polarisé circulaire gauche doit être obtenu, le rayonnement vers l'intérieur étant alors considéré.

On s'intéresse maintenant au niveau de polarisation croisée en fonction de l'angle de dépointage, tracé pour chaque polarisation sur la figure 13. On s'aperçoit que lorsque l'on souhaite focaliser un faisceau polarisé droit vers l'arrière du dirigeable, autour de 270°, le niveau de polarisation croisée remonte fortement. Ceci est prévisible car les antennes sont toutes orientées avec la polarisation circulaire droite vers l'extérieur et il n'y a pas d'antennes rayonnant cette polarisation vers l'arrière du dirigeable. On constate le même phénomène pour la polarisation circulaire gauche vers l'avant du dirigeable.

Réseau conformé hétérogène

On a constaté que si l'on considère un réseau dont tous les éléments rayonnent la même polarisation vers l'extérieur, il n'est pas possible de former un faisceau dans certaines directions car une demi-ellipse seulement est utilisée. Il est donc nécéssaire d'avoir des antennes co-polarisées et des antennes cross-polarisées orientées dans toutes les directions possibles. On modifie alors le réseau en considérant cette fois ci deux types d'antennes. Les antennes de type A rayonnent une polarisa-

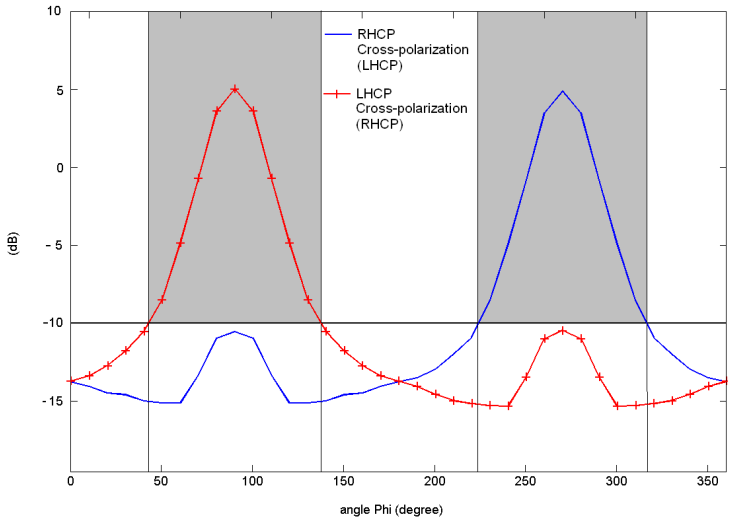

Figure 13: *Niveau de polarisation croisée, pour chacun des deux diagrammes de polarisation en fonction de l'angle de dépointage du réseau.*

tion circulaire droite vers l'extérieur et gauche vers l'intérieur comme précédemment. Les antennes de type B sont des antennes de type A retournées. Elles rayonnent donc une polarisation circulaire gauche vers l'extérieur et circulaire droite vers l'intérieur. On est donc en présence de deux sous-réseaux entrelacés avec des polarisations orthogonales entre elles.

On construit donc un réseau de 134 éléments à partir d'un demi-réseau de 67 éléments dont la séquence antenne type A et antenne type B est choisie aléatoirement. On construit la seconde moitié du réseau en prenant le complémentaire symétrique de chaque antenne. Cela permet ainsi d'avoir le même nombre d'antennes A et B conduisant des performances équivalentes de chaque coté du dirigeable. Les deux sous-réseaux sont lacunaires, ils comportent des éléments non équi-distants qui cassent la périodicité du réseau et ont donc des propriétés intéressantes comme la diminution des lobes de réseaux ou encore l'annulation du deuxième lobe arrière.

La méthode AP est de nouveau appliquée pour le réseau hétérogène en utilisant les mêmes gabarits que précédemment, dans plusieurs directions et chacune des polarisations. Les figures 14 montrent les positions et le type d'antennes qui contribuent au rayonnement polarisé circulaire gauche, dans les directions 10° et 240°. On remarque que, conformément à ce qui a été expliqué auparavant, les antennes type A (bleues) sont utilisée pour leur rayonnement intérieur alors que les antennes type B (rouges) sont utilisée pour leur rayonnement extérieur car la polarisation principale est circulaire gauche. Si la polarisation principale avait été circulaire droite, l'inverse aurait été observé.

On remarque par ailleurs que les niveaux de la polarisation croisée atteignent -10 dB pour

les deux cas exposés. Sur la figure 15 est tracé le niveau de polarisation croisée pour les deux polarisations de diagramme possibles en fonction de la direction du lobe principal. Losqu'on compare ces résultats à ceux de la figure 13, on s'aperçoit que le problème de remontée de polarisation croisée, qui apparaissait auparavant pour les directions arrière et avant du dirigeable, se trouve fortement réduit grâce à l'utilisation d'un réseau hétérogène. Grâce à cet agencement de réseau, il est possible de former un faisceau fin dans la polarisation choisie quel que soit la direction, avec un niveau de polarisation croisée inférieur à -10 dB.

De plus, en étudiant les poids appliqués à chacune des antennes, on s'aperçoit que certain de ceux-ci ont une amplitude très faible. En éteignant les poids les plus faibles, on peut alors diminuer le nombre d'antennes à utiliser pour former le faisceau. On montre ainsi qu'un niveau de polarisation croisé inférieur à -10 dB est toujours possible pour n'importe quelle direction en n'utilisant qu'environ la moitié des antennes disponibles. Lorsque le réseau est utilisé en réception, cette réduction a l'avantage de simplifier la formation de faisceau par le calcul du fait de la diminution du nombre de données à traiter.

Conclusion

L'objectif de ce travail était de montrer la possibilité d'associer dirigeable et antennes radar UHF. Les applications radar envisagées nécéssitent la conception d'un réseau d'antennes large bande et bipolarisé tout en étant compatible avec le dirigeable comme plate-forme d'accueil. Quatre axes de travail peuvent être distingués :

- le choix du type d'élément à large bande, bipolarisé;
- le développement d'une méthode de calcul approchée du rayonnement d'un réseau conforme;
- la réalisation de prototypes et de mesures validant la théorie;
- l'analyse des possibilités de dépointage du réseau.

L'antenne spirale s'est révélée être le meilleur compromis entre les performances large bande et un faible niveau de polarisation croisée. De plus, cette antenne permet de conserver la même polarisation sur un demi-espace, contrairement aux autres antennes étudiées. Une nouvelle sorte d'antenne spirale alimentée de manière coplanaire a également été proposée pour résoudre l'impossibilité d'alimenter l'antenne spirale classique lorsqu'elle est montée sur le dirigeable.

Les couplages entre éléments du réseaux ont été étudiés et jugés suffisamment faibles pour être négligés dans une méthode approchée de calcul de diagramme de rayonnement de réseau conforme. Cette méthode, basée sur les rotations des diagrammes de rayonnement de chacun des éléments, permet d'obtenir les performances du réseau et ne requiert qu'une seule simulation d'élément de

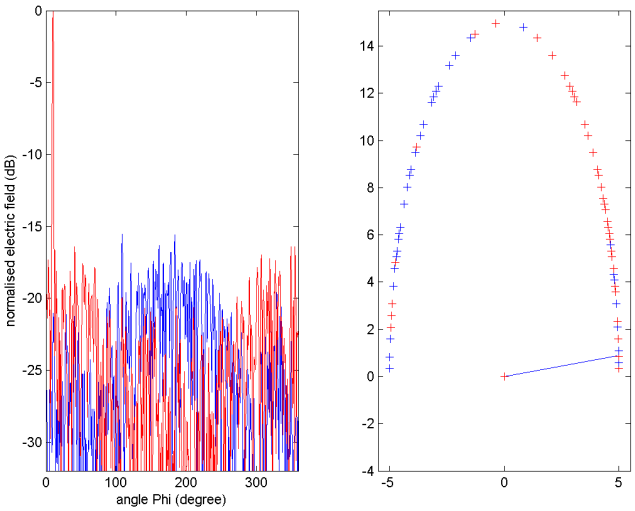

(a) 10°

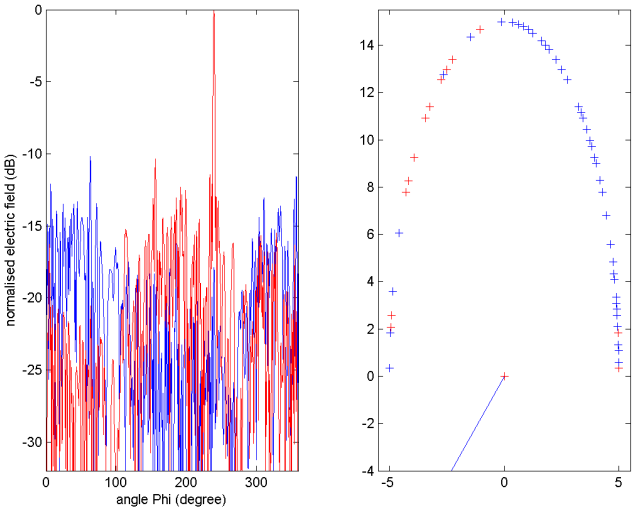

(b) 240°

Figure 14: *Diagramme de rayonnement polarisé circulaire gauche avec le niveau de polarisation croisée correspondant. Partie droite: positions des antennes participant le plus au rayonnement (bleu type A, rouge type B).*

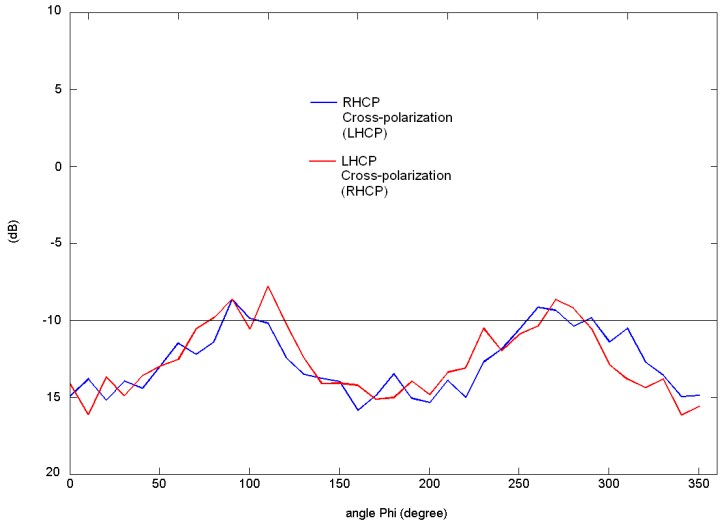

Figure 15: *Niveau de polarisation croisée en fonction de l'angle de dépointage pour chacune des polarisations considérées.*

réseau au préalable. Une comparaison des résultats de cette méthode avec ceux de la simulation et ceux des mesures a permis de valider notre approche.

Une campagne de réalisation et de mesures d'antennes a été menée afin de valider la théorie. Malheureusement, le réseau considéré n'ayant pas de plan de masse, les câbles d'alimentations perturbent inévitablement le fonctionnement des antennes. Malgré cela, les résultats des mesures réalisées ont permis de valider la méthode approchée, étant en même temps en accord les résultats de modélisation.

Enfin, l'analyse du réseau considéré a permis de mettre en évidence certaine spécificités. En effet contrairement aux réseaux classiques, les antennes rayonnent dans toutes les directions de l'espace. Cet aspect peut apparaître comme un inconvénient, en raison de sa complexité. Cependant, en exploitant le rayonnement interne des éléments du réseau, ainsi que les polarisations respectives des éléments, on peut dépointer dans plusieurs directions en n'utilisant qu'une seul réseau linéaire de spirales. De plus, en considérant un réseau hétérogène fait de spirales n'ayant pas toutes la même face vers l'extérieur, on obtient des dépointage sur 360° tout en gardant un faible niveau de polarisation croisée.

Ce travail étant le premier effectué au laboratoire sur ce sujet, a permis de mettre en avant plusieurs pistes de travail pour l'avenir. Premièrement, dans le cas d'un réseau prenant en compte l'alimentation, le couplage peut devenir non négligable et il faudrait alors l'intégrer dans la méthode approchée. De plus, le travail effectué sur un réseau linéaire peut être adapté à un réseau surfacique

qui permettrait alors également un dépointage en élévation. Enfin, la spirale â double excitation coplanaire rend possible l'alimentation d'un réseau sur un dirigeable. Son développement et son intégration en réseau parfaitement plan constituent une perspective prometteuse.

Ph.D THESIS
OF THE UNIVERSITY PIERRE ET MARIE CURIE
PARIS 6

Specialty
ELECTRICAL ENGINEERING

Thesis Submitted for the Degree of
DOCTOR OF PHILOSOPHY

By
François CHAUVET

CONFORMAL, WIDEBAND, DUAL POLARIZATION PHASED ANTENNA ARRAY FOR UHF RADAR CARRIED BY AIRSHIP

Defended
january, the 11^{th} 2008

Jury:

Pr. Raphaël GILLARD, INSA Rennes	Reviewer
Pr. Odile PICON, Université de Marne la Vallée	Reviewer
Pr. Victor FOUAD HANNA, Université Pierre et Marie Curie	Examiner
Pr. Hugh GRIFFITHS, University College London	Examiner
Dr. Régis GUINVARC'H, SONDRA	Supervisor
Pr. Marc HÉLIER, Université Pierre et Marie Curie	Supervisor
Mr. Marc LESTURGIE, Directeur SONDRA	Invited
Dr. Muriel DARCES, Université Pierre et Marie Curie	Invited

Contents

List of Figures

Glossary

AP: Alternate Projection
HAA: High Altitude Airship
CAD: Computer Aided Design
LHCP: Left Handed Circularly Polarization
MoM: Method of Moment
RHCP: Right Handed Circularly Polarization
UHF: Ultra High Frequency
VSWR: Voltage Standing Wave Ratio
VNA: Vectorial Network Analyser

Introduction

Airships are commonly known as advertising platforms, floating in the sky. But they also benefit from a renewed interest for applications like low-altitude surveillance, communication relay and air mega-transport or near space operations [8]. New type of blimps called "high altitude airships" (HAA), are under development in various countries. A HAA is an unmanned, non-tethered, helium-filled, solar-powered craft and would stay aloft 20 km above the Earth for up to a year while carrying 1000 kg of equipment [9]. With a length of roughly 150 m and a diameter of 50 m, these kind of airships reach dimensions comparable to the famous airships flying at the beginning of the 20^{th} [10].

This stratospheric platform, full of high-technology sensors, photovoltaic cells and innovative materials, should provide a cheap alternative to satellites and unmanned aerial vehicles (UAVs) for earth observations of a local area. Moreover, they can offer higher resolution than what is available from satellites in space, thanks to the large space available for the sensor. It is also expected to be a new infrastructure for the new generation system of information and communications.

As a matter of fact, the association of airship and radar seems very promising and several HAA prototype designs have been proposed for various purposes. For instance, the project known as ISIS (Integrated Sensor is Structure) [11] is investigating the integration of very large antennas into airships for a system that would be both sensor and airship.

Several issues limit the realization of HAA, like the pressure and temperature control within the hull, the storage of energy, the deformation and distortion of the airship during the flight and its ability to stay on station. Nevertheless, our work will only focus on the antennas and electromagnetic aspects, taking into account, as much as possible, the compatibility with the other issues. The antennas will be designed for radar applications in the lower part of the UHF band. For instance, this radar could be used for foliage penetration (FOPEN), where low frequencies can penetrate the canopy to detect hidden target.

The large size of an array working in the UHF band has to be stressed. At such frequencies, the array is as large as the airship itself. Our approach is to mount the array on the hull, outside the airship. It has the advantage of using the maximum space available to achieve high resolution radar and to leave intact the airship structure. Hence, no modifications of the host platform area

are required and the array could be mounted directly on airships of different shapes like a "wearable array". As a result, the shape of the array will follow the ellipsoidal shape of the airship and is not planar. Furthermore, radar applications require more and more complex antenna array for efficient detection performances. Thus, wideband and dual-polarization capabilities must be included in the design.

Finally, the idea of using HAA as host platforms is very interesting, but no stratospheric airships, ready for flight, are available at the moment. In addition, detailed informations about HAA technology are limited by this field of research linked to the defense area. Consequently, a commercial blimp is considered in this report to focus on existing technology and to propose a feasible design. The main differences from HAA are its reduced dimensions and lower operating altitudes.

Considering the potential valuable applications of these HAA, along with their originality, Singapore and France have decided to launch together a research program. This has been done within the framework of SONDRA, a joint research laboratory between Singapore and France, made of four partners, Supelec and ONERA from France and the National University of Singapore and the Defence Science and Technology Agency from Singapore. A PhD thesis funded by DSTA has then be started which has mainly aimed at investigating the feasibility of combining antennas and airship. It is first important to define whether airship structure is suitable for a UHF radar antenna array. The location of the antennas on the platform is especially challenging and must be optimized to scan properly all around the structure. Then, a model has to be found to relate the interactions between the antenna and the inflatable structure. It must be also pointed out that the non-planar shape of the airship leads to use curved arrays known as conformal arrays. The conformal arrays are designed according to the platform requirements before electromagnetic consideration and thus can be evermore challenging to achieve and model. Thus, the question of electromagnetic interactions between the platform and the antennas, but also between the elements of the array, has to be solved. At last, the feasibility of beam forming for both polarizations has to be demonstrated.

Chapter 1 describes the technology used for this project: airships, conformal arrays and wideband technology. Details are given about airships history, applications and internal structure, in order to point out their advantages for some applications. Some possible issues when using it as a host platform are also highlighted and some assumptions are done to model the interactions between the platform and the antennas. Then, conformal antenna topic is discussed. The conformal antennas advantages and drawbacks are presented. The computation of a conformal array characteristics requires dedicated numerical methods that are explained. Finally, wideband technology is defined and described. Examples of existing wideband antennas are given to illustrate the origin of the wideband mechanisms. Furthermore, the limitations of the bandwidth for a scanning array are emphasized and lead to requirements on the array element size .

Chapter 2 deals with the design of the conformal array. An array achieving wideband performances, dual polarization, compatible with the platform requirements has to be found. Hence, the size, number of elements, location on the airship, wideband specification have to be defined. First, since various wideband elements have been proposed in the first chapter, the choice of the array element is investigated. Pre-selected antenna candidates are compared using the commercial modeling tool FEKO, based on the Method of Moments (MoM). The chosen antenna design is built in order to be measured for a validation of the modeled results. Thus, results obtained from measurements and modeling are compared. Finally, the issue of feeding the elements mounted on the airship surface is discussed and some new array element designs are investigated.

Chapter 3 tackles the array electromagnetic characterization as well as the computation of the radiation performances. A first part describes the electromagnetic interactions between the array elements using the FEKO modeling tool. Then, a prototype of a small conformal array has been built. The practical feasibility and the issues encountered in measurements are also explained. Finally, an approximated method is developed in order to provide a fast and simplified computation method of the radiation pattern of the conformal array. The validation of the developed approximated method is done through comparisons with measurements and modeling results.

Chapter 4 explains how beamforming can be performed by exploiting the array and the platform configuration. First, the specificity of the host platform and the antennas considered are detailed. The polarization mechanisms are highlighted and taken into account to achieve the polarized pattern synthesis. Some numerical pattern synthesis methods are reviewed and one of them is selected and described for our purpose. A first step considers a classic homogeneous distribution of the elements within the array, where all elements are the same, to underline the capabilities of the pattern synthesis. A second step focuses on the array design and changes the element distribution to achieve better performances. The level of cross-polarization is particularly examined. Hence, results of the pattern synthesis at various scan angles for both polarizations are plotted.

Chapter 1

General Review

1.1 The Airships

Widely used at the beginning of the 20^{th} century, airships have shown their ability in various applications. However, the development of airplanes and a high number of accidents led to the decrease in their interest. Nowadays, if airships are no longer used for passenger transportation, they are still considered for purposes such as advertising and sightseeing. Although they offer particular advantages that cannot be provided by traditional aircrafts, their functioning is not well known and they still suffer of a non-safe easy target image. The airships belong to the "lighter than air" family like the aerostats and can have various shapes and internal structures.

1.1.1 Brief description

First called dirigible balloons, airships were the first aircrafts to make controlled, powered flights, flying throughout the 19^{th} century. Three categories of airships can be differentiated according to their structure [12]: rigid, semi-rigid and non-rigid (see Fig. 1.1). The name rigid airships refers to their internal frame. The Zeppelins and the USS Akron (Fig. 1.2) were famous examples of rigid airships. Their rigid structure, traditionally an aluminium alloy, holds up the form of the airship. In order to have a good weight to volume ratio, the rigid airships must be longer than 120 m. Indeed, a solid frame would be too heavy for a small airship. The semi-rigid airships, more popular in the early 20^{th} century, used a rigid lower keel construction and a pressurized envelope above. The rigid keel can be attached directly to the envelope or hung underneath it. Finally, the non-rigid airships, known as blimps, are the most common form nowadays. They are basically large gas balloons. Their shape is maintained by the internal pressure of the lifting gas.

A serie of tragic rigid airship accidents in the 1920s and 1930s led to the use of smaller and non-rigid airship. The most spectacular and widely remembered airship accident is the burst into

flames of the Hindenburg (Fig. 1.3). In 1937, after making ten transatlantic crossings in regular commercial service, the famous German-built Hindenburg, long of 245 m, crashed when it was landing in Lakehurst, New Jersey. The disaster has been well recorded because of an extraordinary amount of newsreel coverage and photographs. This is why this accident is widely remembered as one of the most dramatic of modern time.

Nevertheless, unlike Zeppelins of fifty years ago, actual blimps are filled with helium, an inert gas. Although hydrogen is a better lifting gas, lighter and more abundant than helium, it is terribly flammable, even explosive. A modern airship's advanced construction and sophisticated control system make it extremely safe to operate even in bad weather. The hull of airships is thought to be its main weakness because of possible holes. However, the lifting gas of a blimp is at a very low pressure, just sufficient to keep its shape. In case of a small hole the gas escapes very slowly and in case of a large hole, the airship is generally capable of remaining aloft for some time before a return to the base [13]. These reasons, plus the advances of technologies, give to the airship a safety guarantee able to deal with various applications.

The current research on airships focuses on one hand on long distance transport of very large payloads at lower cost and, on the other hand, on a long duration, sensor and communications platforms at high altitude.

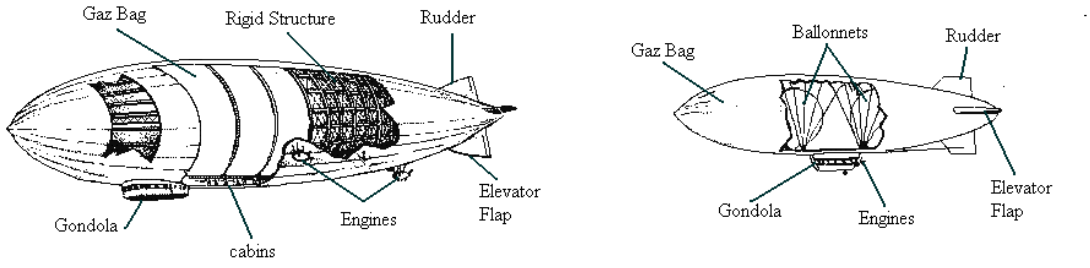

(a) Rigid airship

(b) Non rigid airship

Figure 1.1: *Two various airship internal structures.*

1.1.2 Applications and advantages

In the past, airships have shown their capabilities in both military and civilian roles [14] [15]. Today they are used in a variety of niche applications, like advertising, TV camera platforms at sporting events or as very stable scientific observation platforms [16]. Airships can be also used in surveillance, border patrols, fire-watching and bulky cargo transportation.

Indeed, the airships exhibit various advantages for surveillance purposes. First, the initial cost

Figure 1.2: *USS Akron (ZRS-4) flying over the southern end of Manhattan Island, New York City.*

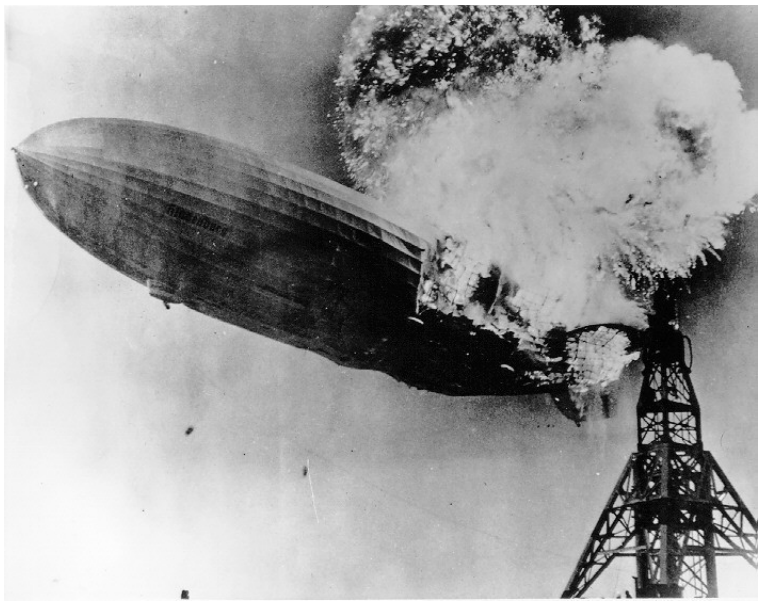

Figure 1.3: *Crash of the Hindenburg in 1937. One of the most spectacular airship accident causing the decrease of the airship activity.*

of an airship is considerably lower than that of any comparable aircraft, helicopter or, of course, satellites. Furthermore, the cost of support and maintain on a day-to-day basis is also lower. Plus, they are highly fuel-efficient.

Then, the airship's lift allows it to remain on station for days at a time. Stationary, noiseless, vibration free, low-speed flight allows on-board surveillance systems to operate in the best conditions. Such abilities give also to the airships considerable advantages as observation platforms over other types of aircraft.

Finally, since it contains only few metallic parts, the airship itself has a very low radar signature, roughly equivalent to a light twin-engined aeroplane. Some designs [17] propose to mount the radar within its envelop and, thus, airships can carry large-aperture radars more effectively and for a much lower cost than any fixed-wing aircraft. The shape and size are then not restricted by the aerodynamic constraints governing externally mounted radar assemblies on aeroplanes.

Airships for surveillance and sport coverage are already in activity [14], they usually use a small video camera. The scanning device is small enough to be placed in the gondola. This configuration has neither specific issues related to the interaction with the platform, nor weight limitations. However, a radar array, with dimensions of several meters is more difficult to carry. In the internal mounted case within the hull [13], a classical and simple planar array antenna technology can be chosen because the envelop acts as a radome and no aerodynamic limitation are taken into account. A radio-controlled blimp is presented in [18] as a new platform for microwave remote sensing. Synthetic aperture radars (SAR), altimeters and scatterometers have been mounted on the airship for geological studies. However, the size of the SAR system has been miniaturized and is not conformed to the airship.

Our approach is different in a sense that we do not want to modify the host platform. The purpose is to build an array able to be conformed on the surface of any airship. In that case, the antenna array and its electronics must lie outside the hull leading to major technological and designing issues.

1.1.3 Airship as a host platform for UHF radar

In our application, we will consider an available non-rigid airship similar to the Voliris 900 [19] that can be viewed in Fig. 1.4 and 1.5. Before deciding how and where to place the antennas, it is first mandatory to analyze its structure and its basic functioning.

As a blimp, the lifting gas is a non-flammable helium and the internal pressure is really low. Internal air compartments (ballonets) are inflated or deflated with air to compensate for ambient pressure differences depending of the altitude. Few pieces of aluminum plus the passenger cabin are usually made of metal, as seen in Fig. 1.6. Furthermore, the airship hull is made of a thin dielectric layer of few millimeters that should not interact with the antenna radiations at few hundreds MHz.

Figure 1.4: *Voliris blimp outdoor.*

The antenna will be conformed on the half front part of the airship in order to avoid the metallic rudder and elevator flap shadowing on the back. Thus, an airship as a host platform for a UHF band airborne radar is a good choice since it can reduce the problem of interactions between the antenna radiators and the platform. At least, composite material solutions, in case of possible remaining interactions, could be an efficient alternative to aluminum.

Unfortunately, the use of an inflatable platform in order to conform the antennas is quite challenging and requires a specific technology. This kind of technology already exists for satellites projects [20], that proposes a large, lightweight structure with photonic data links and a RF/optical transducer. This design consists of a copper foil bounded directly to the skin. Plus, RF-transparent multi-layer insulation jacket is added to protect the inflatable structure in flight. Technological aspect could be inspired by such existing inflatable designs.

Another problem resulting from the non rigid platform is the deformations that could be a source of disturbances. The deformation may come from the ballonets which are required to compensate for the pressure of the airship to keep its shape constant. But, at a constant altitude, during the observation flight, the ballonets have a minor action. Thus this source of disturbances may be overcome. However, due to the speed of the airship - around 70 km/h - a pressure occurs on the airship nose, leading to small deformations. So, the shape of the airship above the ground and in the air, during the flight, should not be exactly the same. As a consequence, the functioning of the array has to be merely calibrated during the flight. For our study, the deformation and mechanical aspects will not be taken into account since it requires other fields of competencies and could be electronically compensated afterward.

1.2 Conformal Array

Conformal arrays are defined by the IEEE Standard Definition of Terms for Antennas (IEEE Std 145-1993) as following: “A conformal antenna is an antenna that conforms to a surface whose

Figure 1.5: *Voliris blimp indoor.*

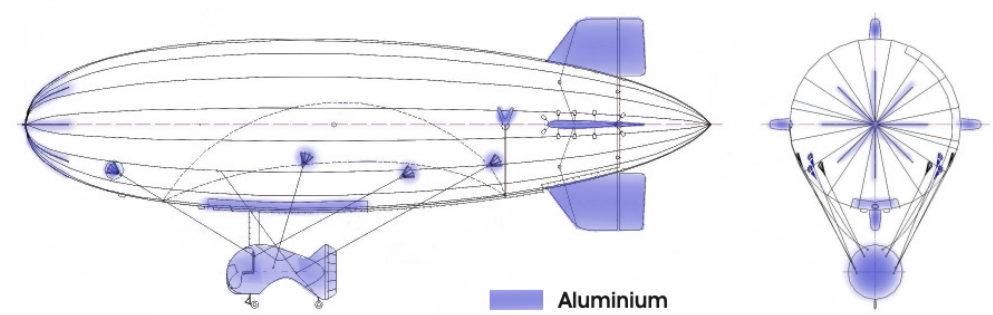

Figure 1.6: *Internal structure of the airship Voliris 900*

shape is determined by considerations other than electromagnetic; for example, aerodynamic or hydrodynamic". In our case, the antenna array is designed to be mounted on the airship hull which offers a large place for a big size radar allowing high resolution performance. Thus, the shape of the array follows the ellipsoidal shape of the airship and becomes a "conformal array". Conformal antenna arrays are typically designed in order to be integrated on various platforms (cars, aircrafts, satellites) and are shaped to fit to the vehicle shape.

The typical motivation for using conformal antenna is to reduce the place taken by the mounted device. Furthermore the antenna does not need additional requirements that would change the initial shape of the vehicle (e.g. AWACS mounted atop an aircraft fuselage in a rotating dome). Furthermore, for some applications, it can be interesting to lower the backscattered microwave radiations when the antenna is illuminated by radar transmitters. Whatever the motivation, a conformal antenna defines the conformation of an array to an arbitrary shaped structure.

An important parameter to specify the conformation is the ratio of the platform radius to the antenna size. Some designs use conformal antennas with platform radius of curvature equal to or lower than the element size [21]. Hence, the radiation pattern of the antenna is strongly modified. In Fig. 1.7(c), an example of a wraparound antenna can be seen [22], where the radius of curvature is small compared to the antenna size. A single feed-point is used and no external splitters, combiners or cable harnesses are required for installation. This antenna is conformal and may be mounted flush, or on the exterior of the vehicle.

However, in most cases, the platform radius of curvature is higher than the size of the array element. Thus, the array characteristics are more affected by the deformation than the element characteristics themselves. Fig. 1.7(a) shows a conical conformal array with a locally planar array, for Earth observation satellites in low Earth orbit. Fig. 1.7(b) and 1.7(d) give recent design examples of conformal arrays on respectively paraboloid and spherical host platform shapes. So, conformal antenna stands usually for non planar arrays that require new and challenging techniques

of analysis.

(a) Conical shape satellite antenna, designed to generate three simultaneous and independently steered beams around for data transmission. Alcatel [23].

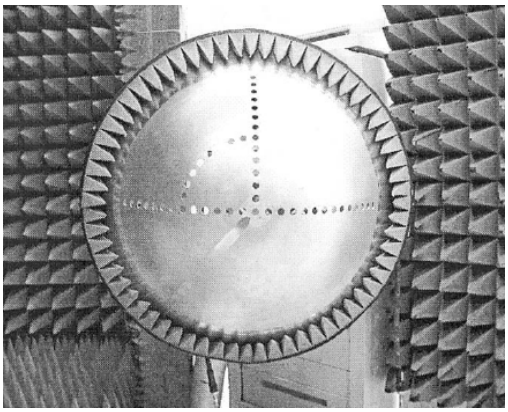

(b) General paraboloid of revolution with circular waveguide-fed apertures built at Ericsson Microwave Systems AB, Molndal, Sweden [24]

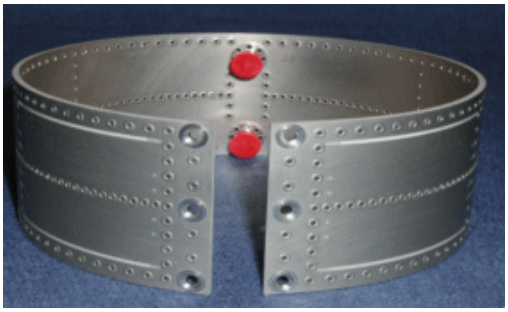

(c) $Haigh - FarrWraparound^{TM}$ conformal antenna. Self-contained and omnidirectional for cylindrical or conical shaped bodies (atmospheric rockets, high speed drones and targets, oil rigs).

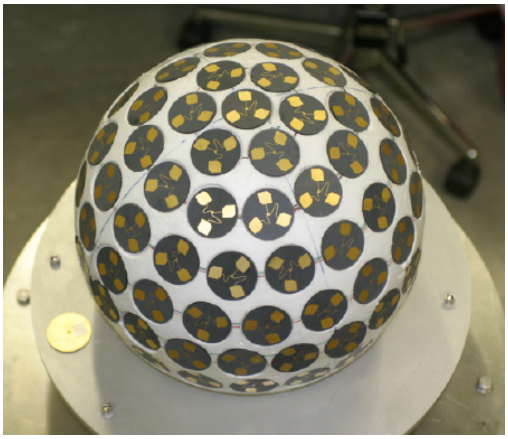

(d) Spherical geometry of a conformal antenna sub-array structure carrying 3 circularly polarized patch antennas [1].

Figure 1.7: *Various shapes of conformal arrays.*

1.2.1 History

First designs of conformal array can be found in the literature and its history is well described in books like [25] or [26]. The research in conformal arrays field is not new: it actually rose up in the 1970's and then followed the breakthroughs of planar phased arrays. Integrated circuit, monolithic microwave integrated circuits (MMIC) helped in using evermore complex shaped arrays and thus conformal arrays. Various canonical shape configurations appear successively in the literature and have been extensively studied: circular, cylindrical and spherical. Besides, conformal array on cones [27] proposed solutions to use nose-mounted antennas on missiles or aircrafts and have been also a center of interest in this area of research. The difficulty of analyzing the conformal array performances is also linked to the lack of powerful computers, slowing down the interest in this field. Finally, the development of the digital technology and the use of more powerful computers conduct to a new interest. Recently, several editions of the European Workshop on Conformal Antenna, starting from 1999 [28], every two years, highlight the concern of the scientific community toward this topic. The future conformal antenna could be viewed as a "smart skin" including every elements of the array, the feed network and the electronics components, shaped as multilayer conformable to any body shape [29].

1.2.2 Advantages and drawbacks

Conformal arrays have many applications and can be preferred to planar arrays in some cases. Two reasons can be distinguished for using conformal antenna instead of their planar equivalent. The first is when it is not possible to use planar array because of design constraints. Indeed, some structures require an antenna to be conformed geometrically to respect payload space limitations or aerodynamic reasons. The second case is to take advantage of the specific conformal array performances. Indeed, when the planar array achieves a $\pm 60^\circ$ scanning angle, the non-planar antenna could allow to scan in a larger domain thanks to the elements orientated at various directions (keeping however in mind that some gain losses can appear). Hence, for instance a circular array has a potential of 360° coverage, like the Wullenweber array (see Fig. 1.8) developed for direction finding [30]. This array is able to form a beam oriented radially outward.

However, the use of conformal array is at the cost of increasing the design complexity. The first and most obvious difference between planar and conformal array is the geometry. The non-planar geometry of the conformal array leads to more complex configurations and thus more complex computations. Indeed, a planar array may be a regular and periodic lattice, simplifying the calculations when analyzed as an infinite array. Consequently, a planar array is generally simpler and cheaper to manufacture than the conformal one.

Then, the use of conformal antennas introduces a higher level of complexity caused by different aspects. The first is that each element has its own environment and its coupling with neighbors

depends on the element position but also on its orientation. As a consequence, the conformal array can be seen as an array constituted of different antenna elements and the element pattern cannot be factored out of the array factor. That implies a computation time increasing with the size of the array that can be sometimes not manageable with the available computer resources.

Conformal array radiation pattern can also be very challenging. Because of the various element orientations, some elements contribute in wrong directions. Hence the array pattern control requires to choose which element must be activated or not. Furthermore, the polarization homogeneity is no longer respected because of the radiator orientation diversity.

The case of doubly curved surfaces increases the level of difficulty due to the non-developable surface characteristic. The array lattice geometry is not simple and triangle or hexagonal lattice may be required. Then, the distribution of the elements on the surface may not be as homogeneous as possible and the constant spatial distribution of the elements may be no longer respected. Furthermore, coupling depends on the local curvature geometry and the difficulty is enhanced in the case of the double curvature. Geodesic in the UTD formulation can be considered for the mutual coupling calculations on a doubly curved surface [31].

Furthermore, the manufacturing and design of such arrays must take into account the whole structure. So, the antenna must include the host platform with the radiating elements. Typically, the host platform has to be modeled with the radiating element, increasing the computation time. Then, the conformal configuration may not facilitate the integration of the electronic circuit feeding and the data link. Also, in most cases the compactness requirement of the curvature space limits the component size.

Finally, a conformal array requires special calculations. Thus, specific analysis methods must be developed in order to predict the array performances. The array pattern synthesis required for radar applications has also to be customized to the conformal case.

1.2.3 Conformal antenna analysis methods

Predicting the properties of conformal arrays is of a great interest, as well as developing new methods of designing the antennas taking into account the platform. Basically, it consists in modeling both the host structure and the antenna array geometry. Two approaches can be considered [32]: simplifying the geometry by choosing approximated models or simplifying the electromagnetic field formulation, starting from a rigorous formulation. Approximated models of the conformal structure have first been proposed, like transmission line models or cavity models. These models lead to very simple closed form equation. However, these approximations are mostly valid for low curvatures or for thin substrates and when practical curved surfaces are described as parts of a simple geometrical surface.

A lot of analysis methods based on full-wave numerical approaches devoted to conformal cases

Figure 1.8: *A large-aperture radio direction finding system known as a Wullenweber array at the Bondville Road Field Station, October 1960.*

have been proposed. The traditional numerical methods like Green's function and integral equation techniques, associated with Method of Moments (MoM), in the frequency domain or time domain, have been applied in many canonical cases. In [21], a numerical routine for calculating Green's functions of general structures is implemented in the MoM program, allowing the analysis of a cylindrical patch antenna printed on a multilayer dielectric structure. Hybrid MoM/Green's function technique in the spatial domain has been used in [33]. In this paper it is shown that the efficiency and the accuracy of the method come directly from the computation of the Green's function, which is the kernel of the electric field integral equation (EFIE) to be solved using the MoM. Therefore, relatively large arrays on electrically large coated cylinders can be analyzed rigorously in which the mutual coupling through both the space and surface waves has been incorporated.

The analysis of a finite array of microstrip patch antennas loaded with dielectric layers on a cylindrical structure is presented using a method of lines (MoL) numerical algorithm in cylindrical coordinates [34]. It is shown that this model has no limitation on antenna array geometry and excitation.

The discrete-mode-matching method (DMM) using a general solution of the wave equation (GSDMM) is extended in [35] to the analysis of microstrip structures embedded in arbitrarily shaped multilayers. It requires discretization and artificial boundaries in only two dimensions, whereas the continuous analytical solutions are used in the remaining direction between the interfaces of the layers.

Hybrid technique methods have also been developed to solve the computation of the antenna radiation mounted on a big size structure. An hybrid UTD-MoM is used in [36] in order to improve the accuracy of the mutual coupling modeling between apertures on a perfectly conducting circular cylinder. It allows to include higher order aperture modes. It is also used in [37] to present

a trade-off between gain and radar cross section for waveguide aperture antennas mounted on a circular cylinder. Then, a hybrid method that combines the MoM with the physical optics (PO) approximation is described in [38]. The PO-current is expressed as a linear superposition of basis functions as well, leading to a very efficient and flexible approach. The potential saving of memory and CPU-time of this method is highlighted. Finite-difference time-domain (FDTD), finite element (FE), as well as high frequency numerical methods like the geometrical theory of diffraction (GTD), geometrical optics (GO) can also be used.

Another approach is to minimize the current induced by the antenna on the platform. The near field is reduced at some points in a synthesis procedure in order to obtain a specific radiation pattern. In [39], far-field pattern specifications are given by masks while near-field constraints are given by prescribing the maximum allowable field intensity at points arbitrarily located in a given near-field region. But this method necessitates to isolate the platform from the array and it is not always possible. Furthermore, mitigating the platform/element interactions is not always a good choice since the platform could be used to reinforce or improve the radiating system performances. In [40], a three-dimensional formulation of the MoM, which models the currents induced on the platform and the antennas, combined with an optimization procedure is proposed. Both the mutual coupling between the array elements and their interaction with the mounting platform are considered and introduced into a synthesis procedure. A reciprocity approach has been also proposed in [41] for the calculation of the radiation patterns of arbitrarily shaped microstrip antennas mounted on circular platforms. The coupled antenna/platform problem is decomposed into two much simpler problems that can be solved independently and the results are combined via the reciprocity theorem.

1.3 Wideband technology

Wideband antennas radiate with an input impedance that remains essentially constant over a wide frequency range [3]. Thus, the antenna bandwidth is defined from a maximum VSWR value which depends on the application requirements (e.g. VSWR less than 2 over the considered bandwidth). The radiation pattern stability is also an important parameter to take into account over the desired frequency bandwidth. However, if the impedance stability is an easy parameter to measure, it is not simple to define a criteria of pattern stability. A Pattern Stability Factor (PSF), based on the correlation of patterns in the frequency domain, has been proposed in [42] to define a pattern-stable bandwidth. More generally, wideband antennas have a radiation pattern suitable for a specific application within the considered bandwidth.

A distinction has to be done between wideband and multiband antennas. A wideband antenna is able to deal with all frequencies at the same time, while for a multiband antenna, only one narrow band over a wide frequency band can be received or transmitted at the same time [43]. Furthermore, a wideband antenna is preferably non-dispersive, having a fixed phase center. Typically, it is

desirable to radiate similar waveforms in all directions.

Wideband performances are required in radar applications to perform efficient and accurate detection. Furthermore, a wideband multifunction RF system can be also an attractive solution to replace several narrowband devices and thus to solve the issue of the lack of place onboard. So, wideband antenna design is a very common field of research and many designs already exist. In our application, a wideband scanning array antenna is also required. Therefore, the main existing wideband concepts will be described and illustrated with some antenna examples, in order to give an insight of wideband principles. Then, wideband performances of antenna arrays will be discussed.

1.3.1 Wideband antenna elements

Various antenna designs have been proposed for wideband applications and historical survey can be found in [44]. In [45], wideband antennas are classified by shape and radiating types. The following designs are presented according to wideband principles in order to understand how wideband performances can be achieved. Nevertheless, some designs can combine various principles at the same time and some principles can be viewed as a particular case or a generalization of another one.

Travelling wave antenna

In order to obtain large bandwidth, it is necessary to minimize the reflected energy over a wide band of frequencies [3]. Thus, traveling wave antenna have been developed, where little energy is reflected from the open end so the input impedance remains constant over a wide bandwidth. This can be achieved using antenna geometry with a smooth transition. Examples of antenna with smooth transition can be seen in Fig. 1.9(a), Fig. 1.9(b). The biconical antenna, as well as the Vee antenna, behave like a guide for the outgoing spherical wave, minimizing the reflected energy. The Vivaldi antenna is a well known wideband antenna and is a special type of a tapered slot antenna with an exponential flare profile. The balanced Vivaldi antenna Fig. 1.9(c) is an enhanced design of the first Vivaldi antenna design that forms an overall balanced structure. Vivaldi profile could be also used in horns (see Fig. 1.9(d)) to bring wideband performances to its directionality capability.

Planar monopole and dipoles

Planar monopoles and dipoles are very popular wideband antennas because of their conformal ability and simple design. The most famous example of planar dipole antenna is the bow-tie antenna, that can be seen as the planar equivalent of the biconical antenna [3], [46]. Various planar monopole and dipole wideband antennas have been studied with various arm shapes: elliptical, square, rectangular, hexagonal, etc. Some dipole design examples are illustrated in Fig. 1.10. The radiating element consists in one plate with a customized shape and a voltage excitation between this plate and the ground plane (monopole) or two identical arm plates (dipoles). The excitation can take place

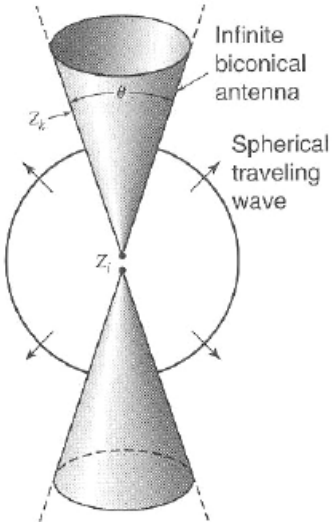

(a) Bicone antenna.

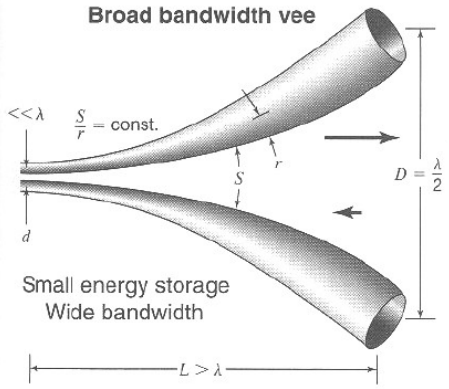

(b) Vee antenna.

(c) Balanced vivaldi antenna.

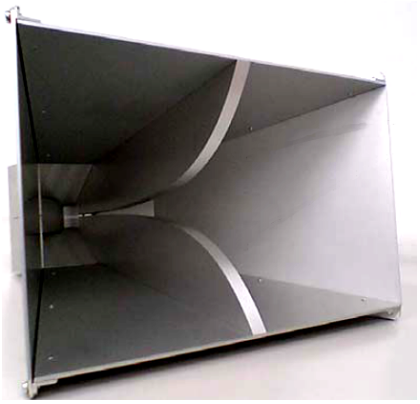

(d) Double ridge horn antenna

Figure 1.9: *Travelling-wave antennas.*

between the short ends (bowtie-like) or the larger ends (diamond-like) of the plate (see fig. 1.10). Recent works [47] compare different shapes and give analysis for a better comprehension of the wideband mechanisms. The plate has generally a progressive shape like a triangle to resonate at different frequencies and minimize the reflected waves. Furthermore, it has been shown that the existence of round corners improves the return loss and the flatness of the input impedance and can enhance the stability of radiation patterns more or less at the same time [2].

Planar antennas have also been analyzed using the "Theory of Characteristic Modes", defined in [48], that helps to give an insight into the wideband mechanism. Based on the observation of the

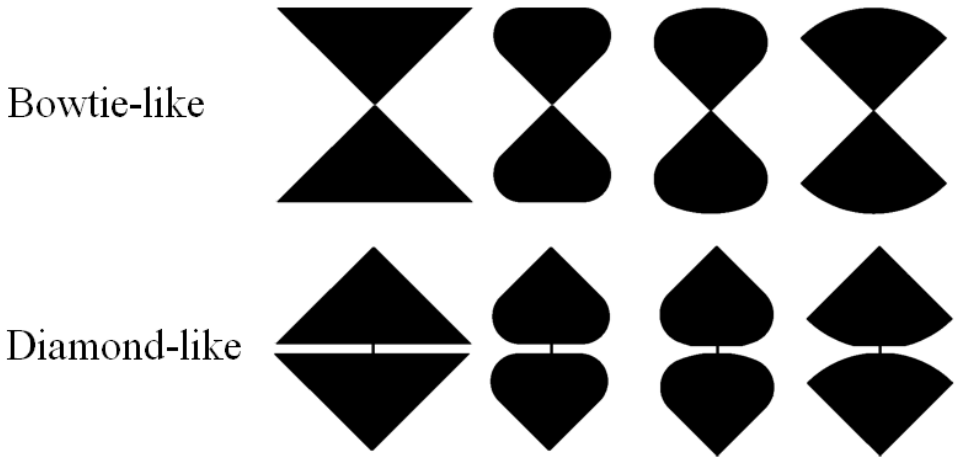

Figure 1.10: *Planar dipoles wideband antennas.*

currents on an arbitrarily shaped surface, it gives informations about resonant frequencies and the achievable bandwidth of the antenna. In [49], it is explained that having the feeding gap at the base of the monopoles is one of the key to obtain wideband behavior. Hence, wideband performances can be also increased by using more than one feeding points.

Fractal antenna

Fractal antennas benefit from two main common properties: self-similarity and fractional dimensions. A self-similar object is exactly or approximately similar to a part of itself. Thus, it contains many copies of itself at several scales and should operate in a similar way at several wavelengths. So, the antenna should keep similar radiation parameters through several bands. Then, the fractional dimensions allow to maximize the length, or to increase the perimeter (on inside sections or the outer structure) of a given total surface area or volume. This leads to a space-filling property which allows fractally shaped small antennas to better take advantage of the small surrounding space. For this reason, fractal antennas are very compact, multiband or wideband. The first fractal antenna elements have been designed in [50]. Furthermore, fractal antenna examples can be also found in [51] and Sierpinski designs are shown in Fig. 1.11(b) and Fig. 1.11(c).

In fact, the first fractal antennas were fractal arrays, with fractal arrangements of antenna elements known as log-periodic invented in last 50' [52]. Elements with a 180° phase shift from the last element are wired alternatingly to the two wires in a balanced transmission line (see Fig. 1.11(a)). The length and spacing of the elements of a log-periodic antenna increase logarithmically from one end to the other. The result of this structural conditions is that the input impedance will follow

periodic variations according to the log-function of the frequency. The log periodic antenna is used in a number of applications where a wide bandwidth is required with directivity and modest level of gain. It is also used at VHF and UHF for a variety of applications, including some uses as a television antenna.

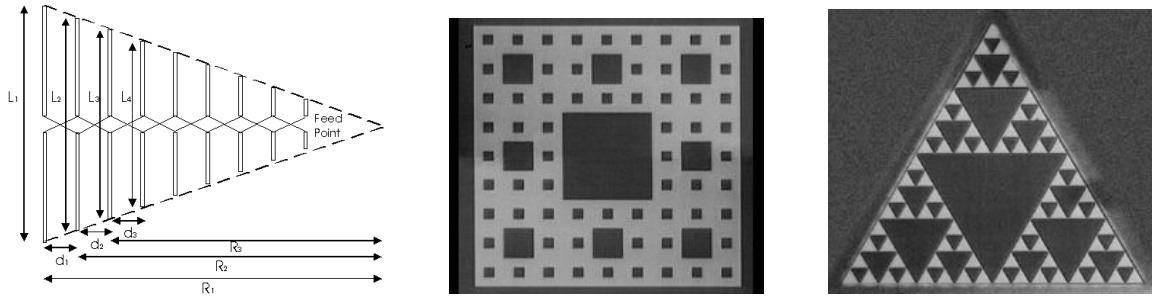

(a) Log periodic antenna. (b) Sierpinski carpet order 4. (c) Sierpinski triangle order 4.

Figure 1.11: *Examples of fractal array (Log periodic antenna) and fractal antennas (Sierpinski designs).*

Self-complementary antennas

The self-complementarity property gives also wideband properties. When the shape of a planar conducting sheet for a slot antenna is exactly identical to the shape of its complementary planar antenna, this antenna can be seen as two complementary antennas and thus is self-complementarity. The input impedance of the conducting sheet antenna Z_1 and the impedance of its complementary Z_2 are linked by the relation $Z_1 Z_2 = (Z_0/2)^2$ according to Babinet's principle [53]. $Z_0 = \sqrt{\mu_0/\epsilon_0} = 120\pi$ is the intrinsic impedance of the medium. So, a self-complementary antenna is such that $Z_1 = Z_2 = Z_0/2 \approx 60\pi \approx 188.4\Omega$ in theory. This means that the input impedance of the self-complementary antenna is always constant, independent of the source frequency. There are infinite varieties of self complementary shapes obtained by axial symmetry (e.g. Fig. 1.12(a)) or either by rotational symmetry (e.g. Fig. 1.12(b)). Rumsey [54] uses this property to introduce the frequency independent antennas with the following principle: impedance and pattern properties of an antenna will be frequency independent if the antenna shape is specified only in terms of angles.

Spiral antennas

The spiral antennas are well known frequency-independent antenna, arranged as a spiraled two-wire transmission lines that gradually transforms itself into a radiating structure. Several variations exist but the simplest is the Archimedean spiral antenna shown in Fig.1.13(a). It has the shape of a self-complementary antenna, in which arm metalization is as thick as the space between arms. The

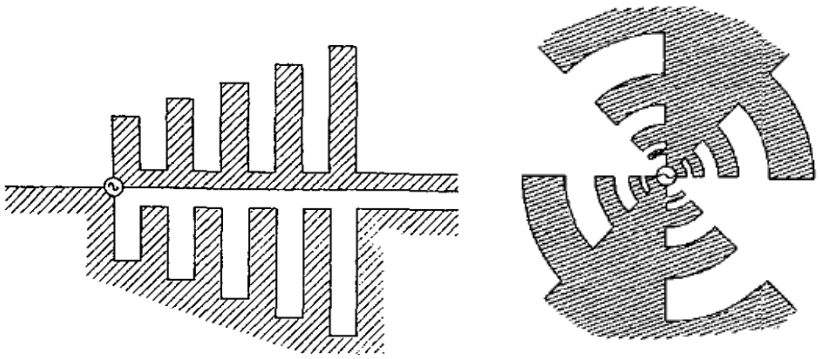

(a) Axial symmetry. (b) Rotational symmetry.

Figure 1.12: *Self-complementary antennas.*

sinuous antenna shown in Fig. 1.13(b), invented in [55], is the most recent frequency independent antenna. It offers several advantages such as wide bandwidth and dual-linear or dual-circular polarization with low-profile geometry [56].

The case of planar N-arm rotationally symmetric antennas is described in [57]. The N-arm antennas are more complex antennas, commonly used in applications that demand wideband, multiple-mode, dual-polarization and conformal geometries. For a N-arm antenna, (N-1) modes are available. Designs examples can be seen in Fig 1.13(b) and Fig 1.13(c)

However, when changing the arm width to gap ratio, the spiral antenna is no more self-complementary. In [58], an analytic expression for the modal impedances used for complementary planar structures is extended to the non-complementary planar antennas. The equations are based on quasi-TEM coplanar stripline theory and provide a band-averaged approximation of the input impedance of the antenna for each characteristic mode of operation.

In conclusion, spiral antennas commonly produce broad main beams perpendicular to the plane of the spiral. The input impedance is constant over a wide bandwidth. Cavity backing is required to obtain a directional pattern. Nevertheless, the fixed distance between the antenna and the metallic plane of the cavity degrades the wideband performances. For multi-octave applications, the cavity is typically filled with lossy material to absorb the backward radiation. However, at least half of the antenna gain is lost, but the antenna maintains its broadband characteristics. Nevertheless, spiral antenna suffers of dispersive effects, meaning a non fixed center of phase.

(a) Archimedean spiral. (b) 4-arm sinuous spiral. (c) 4-arm spiral antenna.

Figure 1.13: *Spiral antennas designs.*

1.3.2 Wideband array

Although antenna elements have been widely studied and a large diversity of designs exist, wideband arrays require specific design attention and are more challenging. First, an array that must achieve wideband performances would require obviously wideband radiating elements. However, the periodic nature of the array is not really compatible with wideband properties. The effect of inter-element spacing is an inherent problem in designing wideband array. Indeed, to avoid the undesirable grating lobes, the inter-element distance must be small, but the minimum spacing is limited by the antenna element size and mutual coupling effects. Nevertheless, if the planar condition is not required, elements with small dimensions in the array plane can be used. The Vivaldi antenna is a favorite candidate for array applications, thanks to its end-fire radiation characteristic: the main lobe is radiated in the plane of the antenna, thus the antenna elements can be mounted as close from each other as desired (Fig. 1.14(a)).

But, for planar element configuration, the array bandwidth is limited by the element size at the lower frequency and the formation of grating lobes at the upper frequency. For a typical array this frequency range may corresponds to an inter-element spacing between a half wavelength and one wavelength or a 2:1 bandwidth.

Hence, some methods have been developed to increase the array bandwidth like the unequally spaced array or the shared aperture array. The effects of various unequal spacing schemes such as logarithmic spacing, non-monotonically increasing spacing and elimination of multiple spacing, have been investigated by [59]. It shows that compared to an equally spaced array, fewer elements of an unequally spaced array are required for a desired bandwidth and grating lobes are replaced by sidelobes. Theoretical models for designing and analyzing unequally or randomly spaced arrays

were introduced in [60]. It is shown that using Poisson's sum formula and a new function called the "source position function", unequally spaced arrays with a desired radiation pattern could be designed. Other techniques, such as shared aperture and non-rectangular grids, can also improve the array bandwidth. A shared aperture array containing elements in L, S, and C frequency bands has been built and measured in [61]. Reconfigurable aperture antenna is also possible to provide wideband performances, in which a planar array of electrically small, metallic patches are interconnected by switches [62]. A Wideband Array with Variable Element Sizes (WAVES) has been proposed in [4] and a 2D-WAVES example design is represented in Fig. 1.14(b). It is a shared aperture technique that uses different element sizes to cover each octave of the desired bandwidth. This technique has been developed in [63] with spiral antenna in order to cover a large bandwidth.

It must be also noticed that wideband array designs are limited by wideband performances of the feeding. Then, the polarization aspect is usually not taken into account in the wideband performances characterization of arrays.

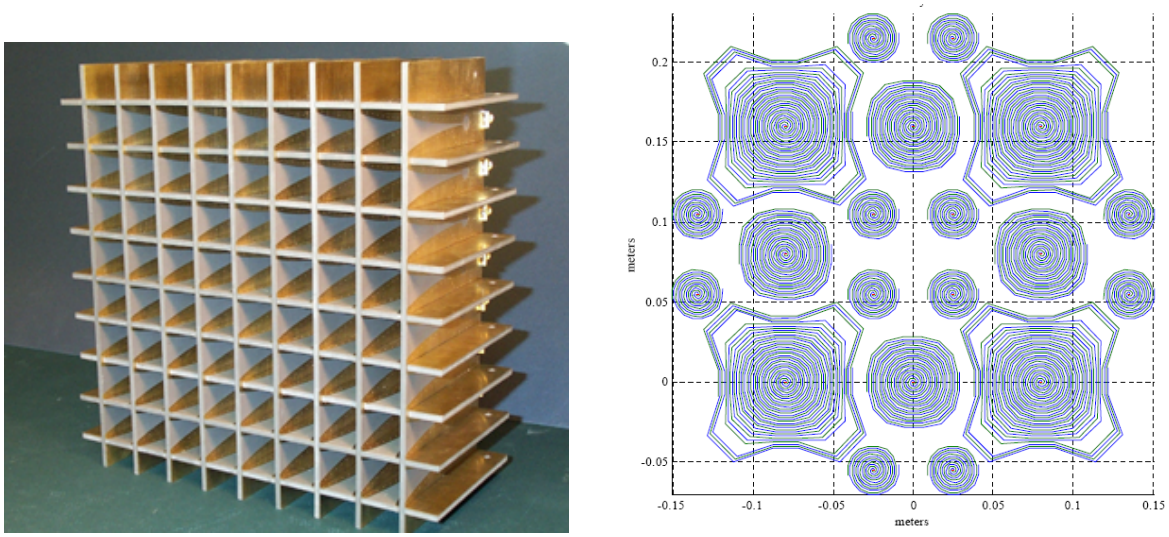

(a) Vivaldi array (144 elements).

(b) WAVES (wideband array with variable element sizes) design proposed by [63].

Figure 1.14: *Wideband array designs.*

Chapter 2

Design of a Wideband, Dual Polarization Phased Array

Radar applications require antenna array that are more and more complex, for efficient detection performances. In our application, both wideband and low level of cross-polarization are required. The other conditions come from the choice of an airship as a host platform leading to new array design conditions. Indeed, conformal antenna array must fulfill the platform compatibility, i.e. flatness, lightweight and compact devices conditions. In this chapter, an array design that fulfills the initial requirements must be proposed to be mounted on the airship.

Numerous antenna element designs exist to achieve an antenna array, and the choice of the element should be done according to the precise definition of the requirements. The modeling tool FEKO based on the Method of Moments (MoM) suits perfectly to the characterization of the antenna element performances, in order to choose the most appropriate design. The array lattice in a non planar surface implies also new limitations that must be also discussed to decide the final array configuration.

Then, measurements should be carried out to validate the modeling results, as well as the practical feasibility of the array measurements. Thus, an antenna prototype will be manufactured and some issues related to the measurements in a conformal configuration will be specially highlighted. In particular, the design issue of the feeding circuit will be discussed.

2.1 Choice of the element

The characteristics of the antenna array intrinsically depend on the choice of the antenna element.

Three requirements will conduct to the choice of the antenna array element:

- its ability to be mounted on the host platform
- its wideband performances
- its low cross-polarization level

First, the array element must be chosen according to the host platform. Indeed, the antenna array must respect some aerodynamic and mechanical conditions to be mounted on the airship hull. So, only planar, compact and lightweight antenna designs can be used. Then, in order to design an array able to scan around the airship, the element radiation characteristic must have its main radiation at broadside, i.e. perpendicular to the antenna plane.

Second, wideband ability of the element must be respected. Chapter 1 gives a lot of examples of antenna designs in section 1.3. The four designs of Fig. 2.1 seem to provide good characteristics for our application and are selected for the comparative study. The cross-polarization level condition will be determined using the modelling tool.

The Archimedean spiral antenna is the simplest antenna among spiral antennas and is well known for its multiband ability. The three other candidates are wideband dipoles, commonly used and extensively studied, described in the section 1.3.1 of the first chapter. Three shapes from [2] have been selected and will be considered: the Quadrate Bowtie Antenna with Round Corners (QBARC) (Fig. 2.1(b)), the Triangular Bowtie Antenna with Round Corners (TBARC) (Fig. 2.1(d)) and the Inverse Triangular Bowtie Antenna with Round Corners (ITBARC) (Fig. 2.1(c)).

The four selected antenna designs will be compared in terms of bandwidth and polarization characteristics in free space. Using FEKO, the planar antenna geometry are meshed using triangles. The voltage excitation is provided through a segment element between the two planar arms of dipoles or spiral. The size of the antenna is chosen to radiate in the chosen frequency band. For scanning arrays, the upper bound of the frequency bandwidth is fixed by the distance between array elements. Gratings lobes can be avoided if a maximum distance $\frac{\lambda}{1+|\cos(\phi)|}$ is respected, with θ the scan angle and λ the wavelength. Pratically, a $\lambda/2$ distance is chosen for scanning array designs. Thus, for a maximum frequency of 600 MHz, a maximum of antenna length equal to 0.25 m has to be respected. So, all antenna elements are designed to have the same length or diameter and are modeled using FEKO.

2.1.1 Wideband performances of the element

Bandwidth

The bandwidth of an antenna can be defined as the frequency range within which the antenna exhibits a low reflection level [3]. Thus, either the S_{11} coefficient or the VSWR value of the antenna

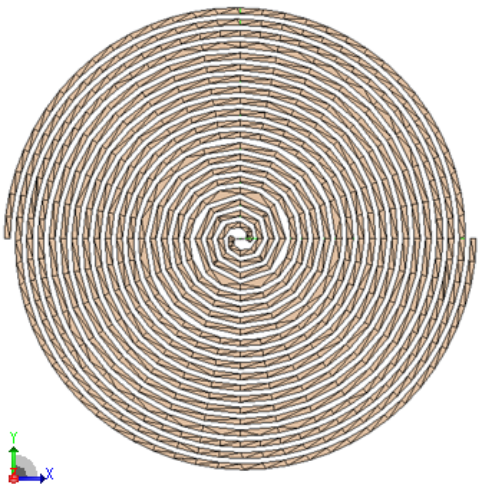

(a) Archimedean spiral.

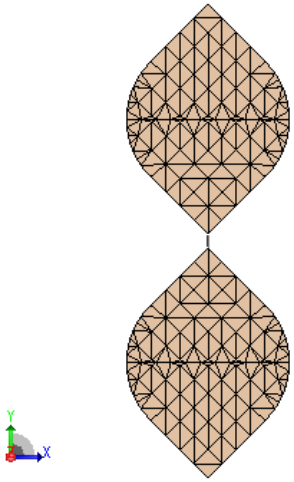

(b) Quadrate bowtie antenna with round corners (QBARC).

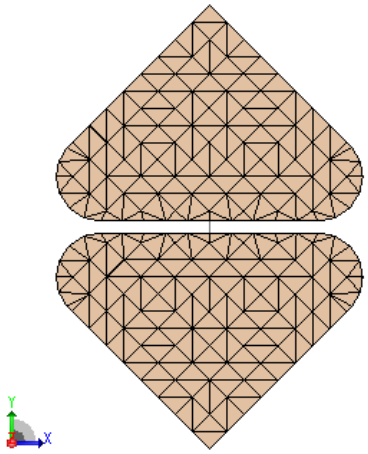

(c) Inverse triangular bowtie antenna with round corners (ITBARC).

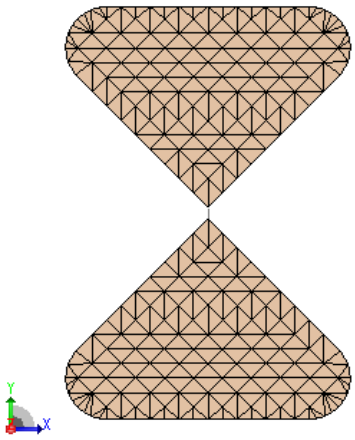

(d) Triangular bowtie antenna with round corners (TBARC).

Figure 2.1: *Geometry and FEKO discretization of the planar wideband antennas under study in free space.*

can be used. The VSWR is the ratio between the sum of standing waves V_{max} and the differences of the standing waves V_{min} (Eq. 2.1). It can also be expressed as a function of the reflection coefficient

VSWR ≤ 3	Spiral	QBARC	TBARC	ITBARC
Z_0	200 Ω	100 Ω	75 Ω	75 Ω
F_{min}-F_{max} (MHz)	400-600	470-790	320-450	440-650
Relative bandwidth	40 %	50 %	34 %	38 %
VSWR ≤ 2	Spiral	QBARC	TBARC	ITBARC
Z_0	200 Ω	50 Ω	50 Ω	50 Ω
F_{min} - F_{max} (MHz)	410-600	460-560	330-370	470-540
Relative bandwidth	37 %	19 %	11 %	14 %

Figure 2.2: *Comparative study of relative bandwidth value obtained from the modeling of the four antenna candidates. Both VSWR $\leq$ 2 and VSWR $\leq$ 3 are considered at the best matching values.*

ρ. So, it also depends on the antenna input impedance Z_{in} and the line characteristic impedance Z_0 (Eq. 2.2). When the feeding cable is matched to the antenna impedance, the VSWR becomes very small and usually the bandwidth is defined for a VSWR ≤ 2

$$VSWR = \frac{V_{max}}{V_{min}} = \frac{1 + |\rho|}{1 - |\rho|} \tag{2.1}$$

with:

$$\rho = \frac{Z_{in} - Z_0}{Z_{in} + Z_0} \tag{2.2}$$

The VSWR is plotted in Fig. 2.3, for each antenna candidate and for various values of matching corresponding to the feeding line impedance Z_0. According to the application, the VSWR criteria can be less demanding. Thus, the array element used for a receiving radar may be suitable with poorer matching. Hence both VSWR ≤ 3 and VSWR ≤ 2 will be considered and compared to define the bandwidth of the antenna, even if the VSWR ≤ 3 criterion means more mismatching and more reflections.

Table 2.2 sums up the relative bandwidth of each antenna with criteria VSWR ≤ 2 and VSWR ≤ 3. It can be observed that the QBARC has a better bandwidth (50 %) than the other candidates, if the VSWR ≤ 3 criterion is considered. However, if we consider a VSWR ≤ 2 criterion, the spiral has the largest bandwidth.

In an array configuration, the bandwidth is limited to 600 MHz due to the antenna size and the distance between elements center to center. As a consequence, the ITBARC design which have a

better relative bandwidth compared to the TBARC design would be limited to 600 MHz instead of 650 MHz. Thus the new relative bandwidth of an ITBARC array would be reduced to 31%, i.e. less than the bandwidth of a TBARC array design.

The TBARC design has the advantage of smaller dimensions compared to its minimum frequency, allowing a higher maximum frequency in an array configuration. Anyway, the bandwidth of the array is limited by the element bandwidth. It must be also noticed that some advantages are provided by its small relative size. Indeed, in an array configuration the coupling between neighbored elements might be reduced.

Considering the bandwidth given by the VSWR values, the best designs are the QBARC and the Archimedean spiral. The QBARC has a good bandwidth if a VSWR ≤ 3 is considered. Furthermore, its design allows a compact lattice with vertical and horizontal elements easily manageable. The spiral design has the best performances if we consider the VSWR ≤ 2 criterion. However, its matching impedance is equal to 200 Ω and is four times that of QBARC antenna a (50 Ω for VSWR ≤ 2) and thus requires an efficient matching circuit. Furthermore, the dimension and shape of the spiral traditionnaly do not allow lattice with orthogonally polarized elements.

Impedance

The bandwidth is also linked to the antenna input impedance stability. The more flat the input impedance is, the easier the design of the matching circuit. So, an analysis of the four designs impedance must confirm the results found in the VSWR study. The impedance of the four antenna designs according to the frequency can be seen in Fig. 2.4. It reveals that the ITBARC, TBARC and QBARC impedances have a quite similar behavior according to the frequency. Both imaginary and real part of the input impedance increase. The real part of the impedance within the frequency band corresponds to the matching impedance chosen for an optimized VSWR level (with a VSWR$\leq$3 criterion).

The input impedance of the spiral, both for the imaginary and real parts, is nearly constant at high frequencies. It must be noticed that within the 400-500 MHz band, the real part is quasi-constant but not the imaginary part. So, the Archimedean spiral, as a frequency independent antenna, exhibits better impedance stability over the antenna bandwidth than the bowtie like antennas.

2.1.2 Radiation characteristics

Radiation pattern

The shape of the radiation pattern is an important parameter to consider for a conformal array on a doubly curved surface. The array can radiate in a given direction if some elements of this array radiate in this direction. Thus, an element with an omnidirectional radiation pattern would

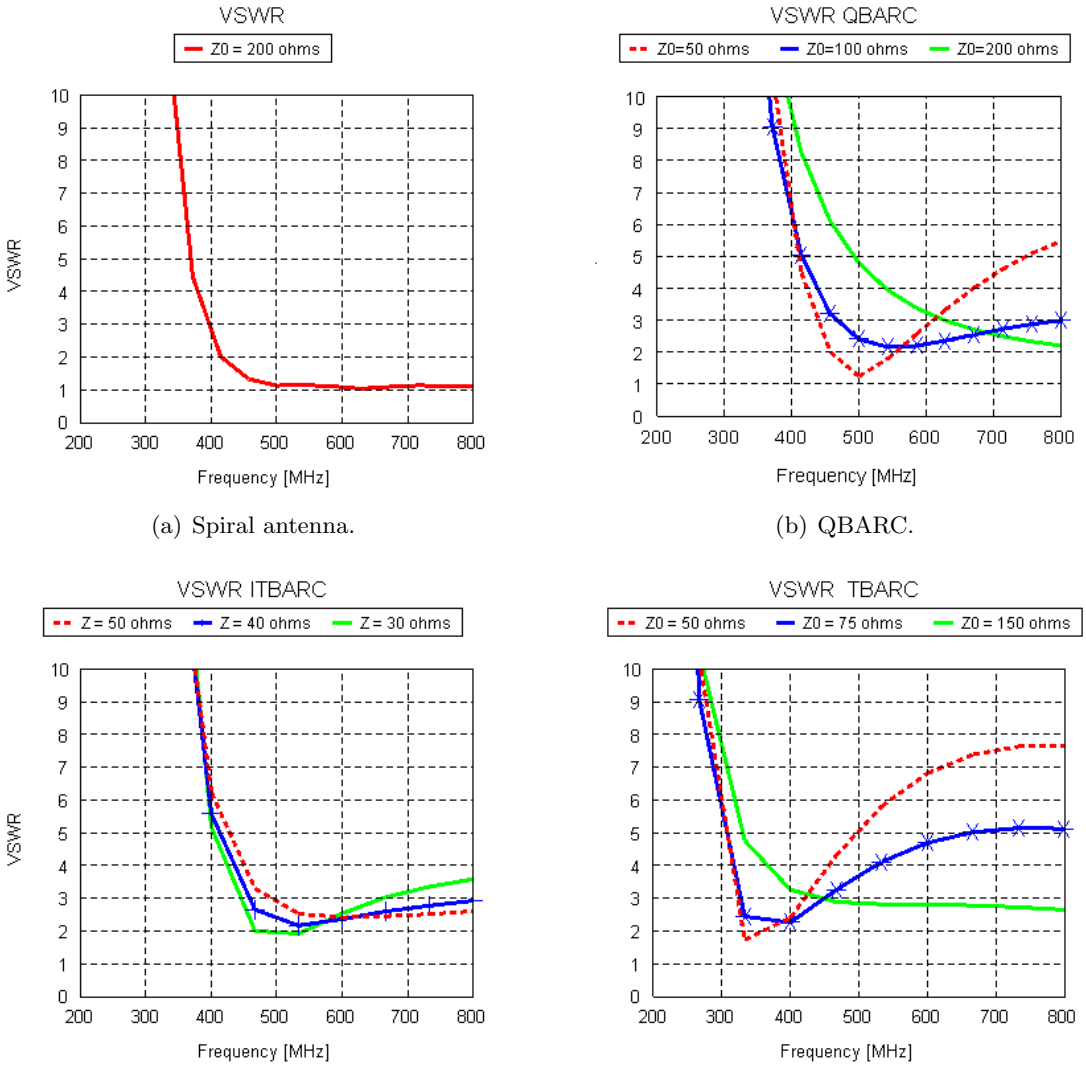

(a) Spiral antenna.

(b) QBARC.

(c) ITBARC.

(d) TBARC.

Figure 2.3: *VSWR computed by FEKO.*

be preferred, in order to design an array able to scan in any direction. The difficulty comes from the fact that each element of the conformal array has its own orientation. So, for a given direction, the radiation contribution can be different for identical elements positioned at different places.

The antenna elements have been chosen to radiate a maximum of energy in the direction perpendicular to the plane of the antenna and thus perpendicular to the local plane of the array. Fig. 2.5

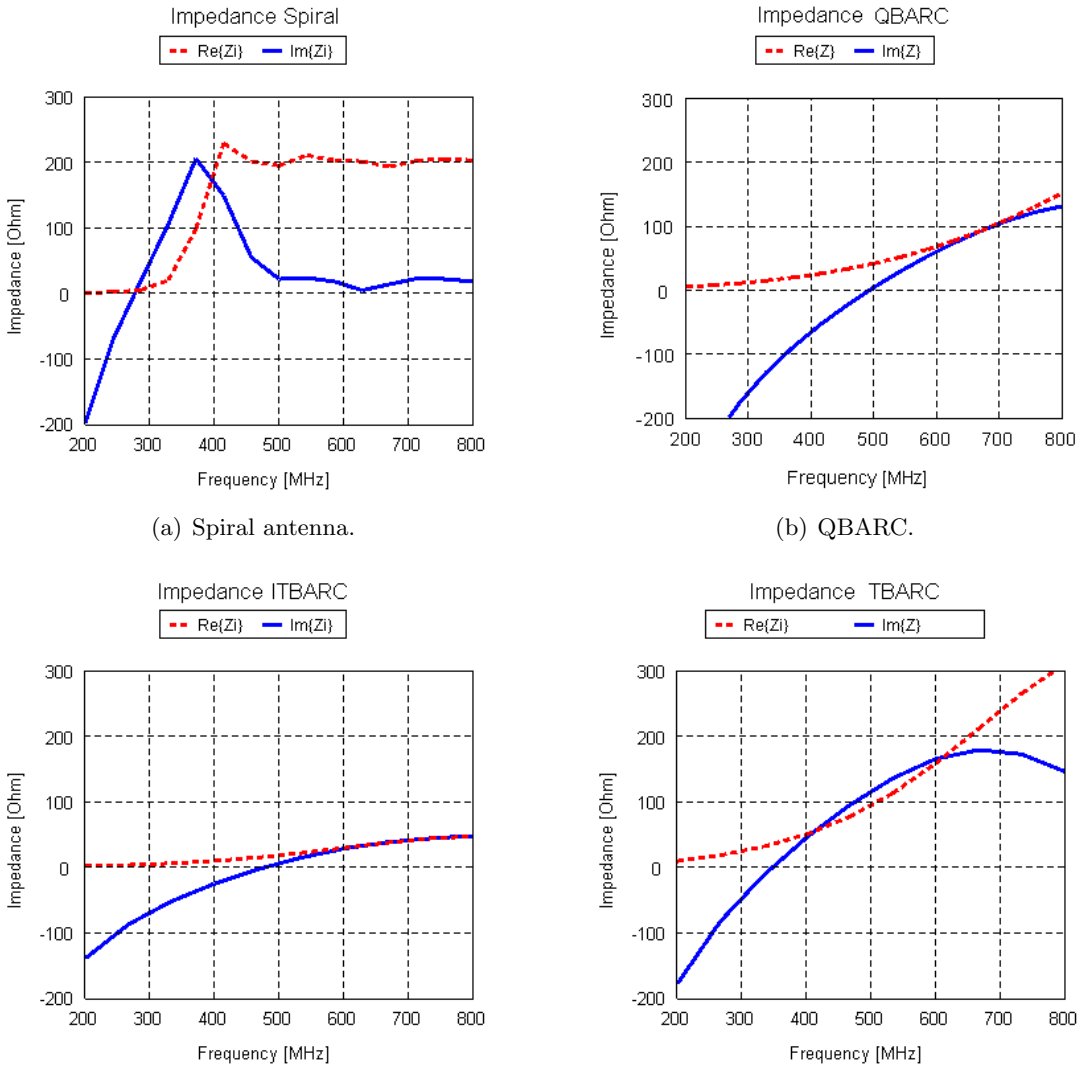

(a) Spiral antenna.

(b) QBARC.

(c) ITBARC.

(d) TBARC.

Figure 2.4: *Input impedance computed by FEKO.*

gives the 3D radiation pattern with the antenna geometry. Two types of radiation pattern shapes can be distinguished for the four candidates: a "donut" shape for the bowtie-like antennas and a "8" shape for the spiral. The "donut" shape has a **xz** plane of symmetry which presents the advantage to radiate the same magnitude at any θ at $\varphi = 0$. It can be very useful if the curvature of the array is in this plane. But it is only the case for simply curved array and not for the doubly curved one.

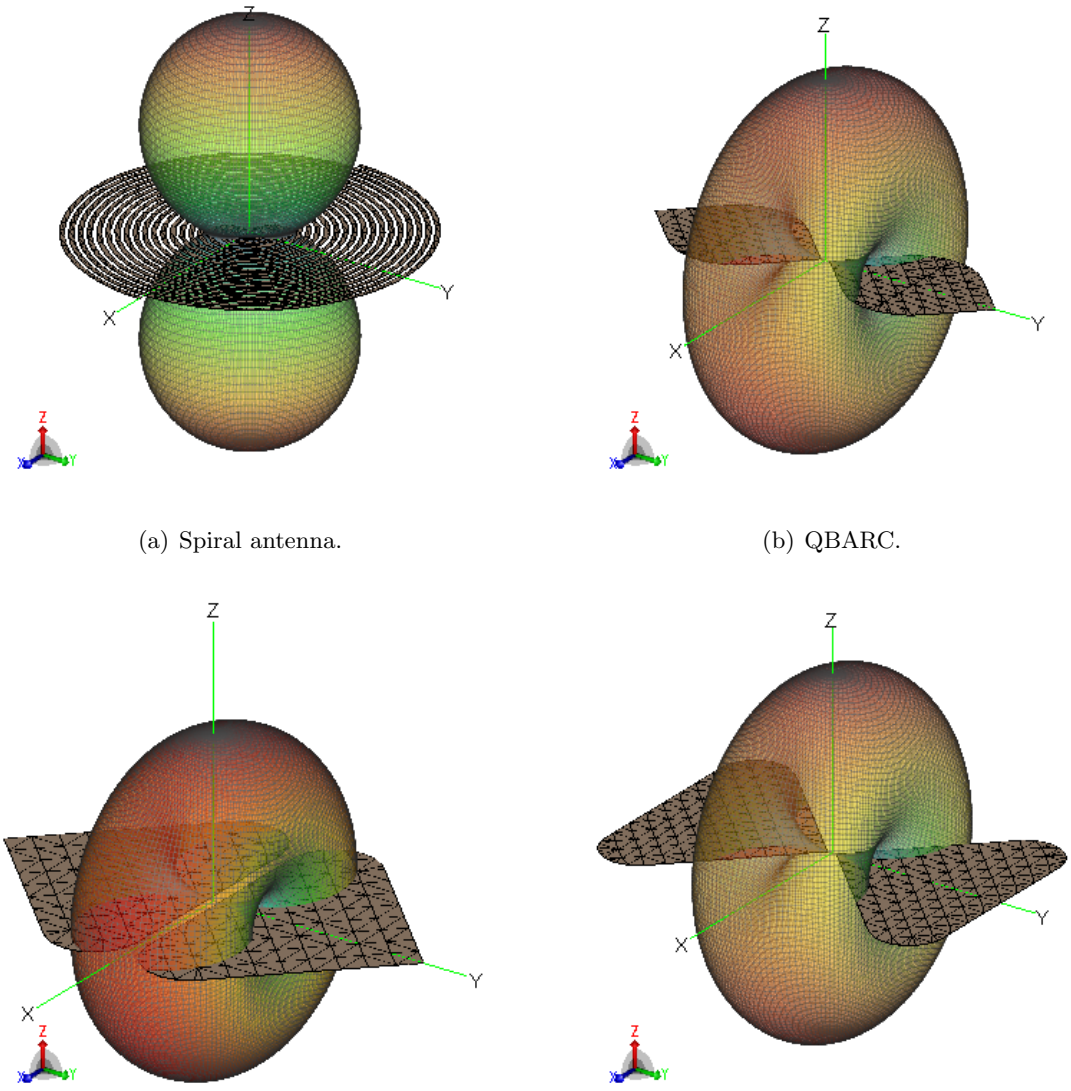

(a) Spiral antenna.

(b) QBARC.

(c) ITBARC.

(d) TBARC.

Figure 2.5: *Shape of the total radiation pattern computed by FEKO, at 600 MHz.*

The "8" shape of the spiral radiation pattern has very low radiation in the plane of the antenna that forbids to synthesize a beam array in this direction. However, it has the advantage to have a **z** axis of rotational symmetry, perpendicular to the plane of the antenna. So, the doubly curvature

of the array will not influence too much the radiation magnitude if small angles are considered.

Using "donut shape" radiation patterns is manageable for a doubly curved array, but introduces a non symmetry that must be taken into account if both vertical and horizontal elements are used. The "8-shape" radiation pattern of the spiral is less sensitive to the doubly curved surface issue, but has poor radiation component in the array plane.

Cross polarization level

A bowtie-like antenna radiates a linearly polarized electric field. Vertical and horizontal polarized gain are plotted for the direction along the **z** axis, as depicted in Fig. 2.6. It can be seen that the cross polarization level is very low at any frequency. In the second case, depicted in Fig. 2.7, the chosen direction is $\varphi = 45°$ and $\theta = 45°$. In that direction, the cross polarization is very high. Less than 5 dB exist between the two polarization components. Thus, the level of the polarized field strongly depends on the orientation for those designs.

The spiral antenna radiates a circularly polarized electric field. Thus, LHCP and RHCP polarized gain are plotted in Fig. 2.6(a) at $\varphi = 0°$ and $\theta = 0°$ and in Fig. 2.7(a) at $\varphi = 45°$ and $\theta = 45°$. It can be observed that the cross-polarization level is similar for both cases and does not depends on the direction. However, the level of cross polarization depends on the frequency and is higher at the lower frequency. From 450 MHz to 600 MHz, 10 to 20 dB can be obtained between the two polarizations.

So, it has been shown for bowtie antennas that the cross-polarization level characteristics strongly depends on the direction. In the case of the doubly curved conformal array, a diversity of element array orientation is introduced. So, the spiral radiation characteristic, which has an axis of symmetry, is of a great interest for this application. However, for a dual-polarized array design achieving both RHCP and LHCP, two types of spiral antennas have to be used, since they radiate only one polarization above and below their plane.

2.1.3 Wideband performances of an array

It has been shown previously that the most suitable elements for our application are the spiral antenna and the QBARC design. Thus, the possibility of using them in a wideband array is discussed. The upper bound of the array bandwidth is limited by the distance between elements. Indeed, grating lobes occur when scanning, if the inter-element distance is longer than a half wavelength ($\lambda/2$). The closer the elements are, the higher the maximum frequency bound is. However, the size of the element limits the inter-element spacing and the element has to be large enough to radiate properly. Hence, its size fixes the minimum frequency bound of the bandwidth. Thus, to improve the bandwidth of an equally spaced array using identical elements, it is necessary to choose an element as compact as possible. It means that for an equivalent size of 0.25 m, the spiral antenna

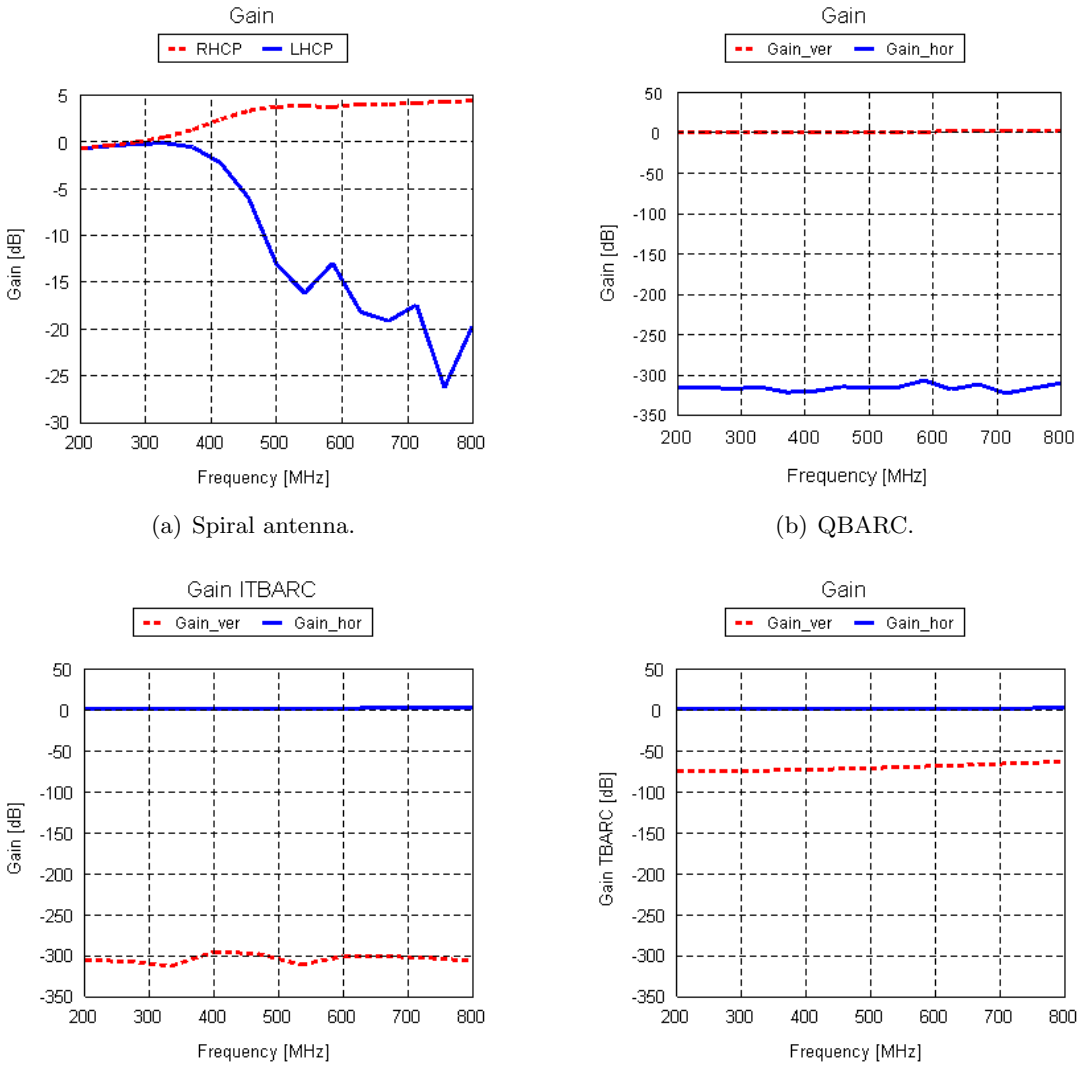

(a) Spiral antenna.

(b) QBARC.

(c) ITBARC.

(d) TBARC.

Figure 2.6: *Polarized components of the gain in the direction ($\theta = 0°, \varphi = 0°$)*

can still radiate at 410 MHz according to Fig. 2.3(a) and the QBARC has a minimum frequency of 460 MHz according to Fig. 2.3(b).

Actually, the theoretical minimum frequency of an Archimedean spiral antenna with a diameter D is $F_{min} = c/\pi D$ (with c the celerity of the light). Thus, the spiral antenna is more compact than wideband dipoles. However, only one polarization can be achieved considering half space separated

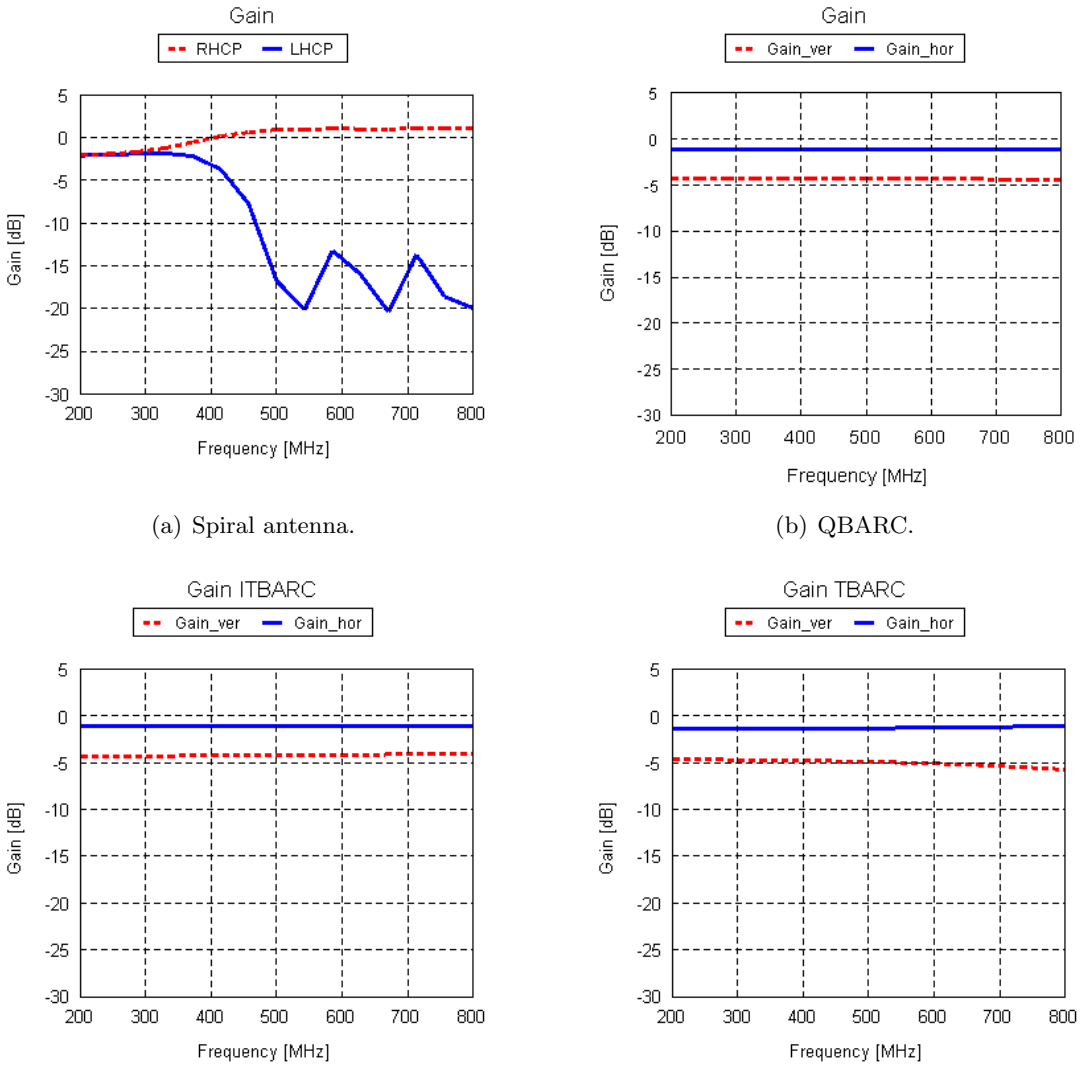

(a) Spiral antenna.

(b) QBARC.

(c) ITBARC.

(d) TBARC.

Figure 2.7: *Circularly polarized component of the gain in the direction ($\theta = 45°, \varphi = 45°$)*

by the antenna plane. Thus, at least two spirals must be used to design a dual polarization array. So, both RHCP and LHCP sub-arrays must be used at the cost of doubling the array surface (see examples of configuration in Fig. 2.8). It seems to be more challenging to recombine the signals, since RHCP arrays and LHCP sub-arrays are not located at the same place.

QBARC antenna element is linearly polarized and two elements have to be combined to form

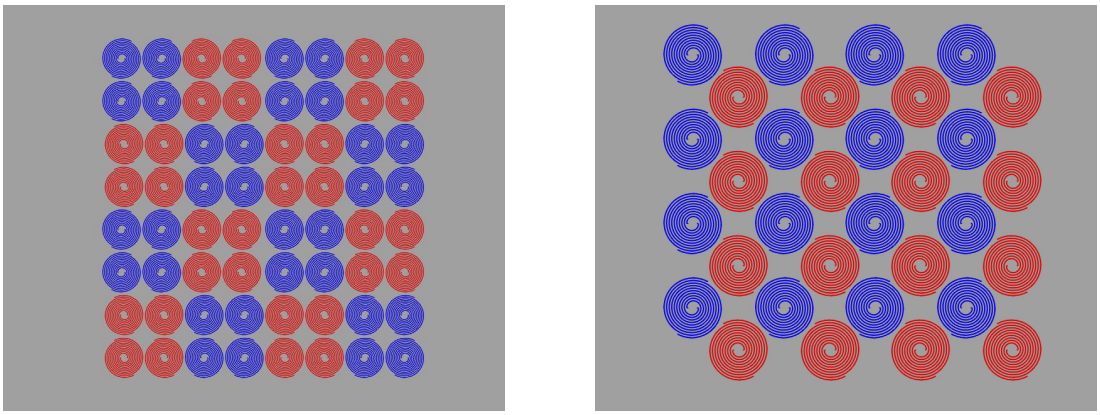

(a) Configuration 1. (b) Configuration 2.

Figure 2.8: *Proposition of array arrangement using spiral element in order to obtain both polarization. Blue spiral (RHCP), red spiral (LHCP)*

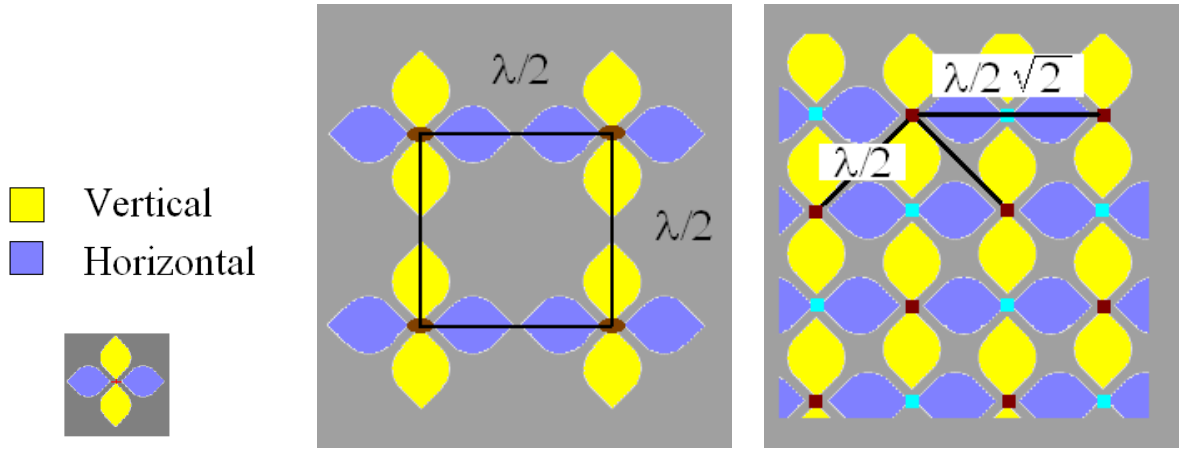

(a) QBARC single element for a dual polarized array. (b) QBARC array configuration 1. (c) QBARC array configuration with a minimum distance reduced by a factor $\sqrt{2}$.

Figure 2.9: *Proposition of array arrangement using QBARC element in order to obtain both polarization.*

a dual polarization antenna like cross-dipoles (see Fig. 2.9(a)). So the array lattice could have a configuration as proposed in Fig. 2.9(b). However, it is also possible to have a more compact lattice as it can be seen in Fig. 2.9(c) thanks to the shape of the QBARC antenna. In this configuration, the vertically polarized element is not located in the same place as the horizontally polarized element.

The distance between element can be reduced by a factor of $\sqrt{2}$ to improve the array bandwidth, but the element bandwidth would limit its performances. So, it seems more simple to use QBARC design elements instead of spiral to form a compact doubly polarized array.

To conclude, the comparative study has shown that the spiral element bandwidth is greater than that of the planar wideband dipoles and that the element is more compact than any other. However, if we consider the array arrangement, the wideband dipole QBARC is more suitable to form compact lattice with bandwidth comparable to that of a spiral array, with the advantage of a smaller total surface. Since our application must also consider the polarization information, this is a parameter to take into account in the choice of the element. The level of the cross polarization of a QBARC antenna is clearly not as good as the cross polarization level of a spiral if all the possible scanning directions are considered. Furthermore the spiral radiates the same polarization in any directions of an half space. So, for conformal array applications, the half omnidirectionality of polarization must be an advantage. Thus, the spiral antenna is chosen as the element of the conformal array performing wideband and dual polarization performances with a low level of cross-polarization.

2.2 Prototype of the spiral

In order to validate the modeling results of the chosen spiral antenna, a prototype of spiral antenna is built. The measurements of the antenna characteristics are expected to confirm the wideband performances of the antenna in terms of impedance over the considered bandwidth. Moreover, the radiation characteristic of the antenna (shape and gain) have also to be validated. Finally, the experimental approach must demonstrate the feasibility of measurements including the feeding cable that has been omitted in the modeling. Indeed, the lack of metallic ground plane will not isolate the cable from the antenna elements and thus some perturbations will occur.

2.2.1 Building of prototypes

A prototype antenna must be built to radiate in the frequency range of interest, 400-600 MHz, leading to an antenna diameter of 0.25 m. With this dimension, a spiral array prototype would reach the size of several meters. Since the anechoical chamber has a limited size, it is preferred to reduce to half the size the prototype, increasing accordingly the frequency range with a factor of 2. So, the practical range of frequencies considered for measurements is [800-1200] MHz with an antenna prototype diameter of 12.5 cm.

The spiral antenna shape is designed design using the CAD (Computer Aided Design) tool *Rhinoceros*. The corresponding mask (see Appendix) has been used in a photolithographic process to obtain the printed antenna on a substrate of 0.8 mm thickness and a permittivity $\epsilon = 3.38$. Then, the spiral antenna on the substrate has to be connected to the coaxial cable and thus, a

SMA connector must be integrated in the design (see Fig. 2.10). However, the spiral antenna exhibits a theoretical 188 Ω input impedance and its two spiral arms have to be excited with a balanced current. Typical electronics circuits as well as the vector network analyser (VNA) provide unbalanced coaxial feeding at 50 Ω. Thus, a matching component with a balance to unbalance conversion capability is required (see Fig. 2.10(a)).

Thus, a surface mount technology transformer has been purchased (details in appendix). It is able to match the 50 Ω of the coaxial cable output with the 188 Ω input impedance of the spiral antenna and it provides a balanced interface at the secondary winding. Then, its small size should minimize its interaction with the antenna, since measurements must fit the model used in FEKO, where no cables influence is taken into account. The resulting design can be seen in Fig. 2.10(d). The spirals have been printed by an external manufacturer, components have been assembled at Supelec by technicians as well as the transformer and SMA connector soldered on the printed circuit.

Complementary modeling with FEKO helped to characterize the cable influence on the antenna radiation characteristics. It has been shown that the cable should be orientated perpendicular to the antenna plane. Indeed, in case of a cable parallel to the antenna plane, coupling between the radiated field and the cable is observed. So, the feeding cable will be kept as much perpendicular to the antenna plane as possible.

2.2.2 Measurements

Nine spiral antenna elements have been manufactured and their individual characteristics are measured by using a vector network analyzer. These antennas will be mounted afterward in an 8-element array configuration. Besides, it allows to investigate the measurement results dispersion and then to conclude on the reproducibility of the design. The array measurements results must fit the modeling results of a uniformly excited array. Thus, a minimum dispersion is expected between the various antennas to obtain an array with similar components.

S_{11} measurement

First, the S_{11} reflection coefficient is measured in an anechoic chamber. The results for each antenna prototypes at various frequencies can be seen in Fig. 2.11. The measured S_{11} values are higher than expected between -4.5 and -7.5 dB, meaning that reflections occur. It is supposed that the use of a transformer introduces additional reflection due to its input return loss characteristics (between 10 and 20 dB according to the frequency) given in the data sheet (see appendix). Measurements of transformers components to get the full complex characteristics would be useful to confirm the values given by the commercial documentation, but have unfortunately not be done at the moment.

The dispersion of measurement results is depicted in Fig. 2.11(a) and Fig. 2.11(b). It can be seen that the magnitude dispersion between the measured elements is roughly under 1.5 dB and that the

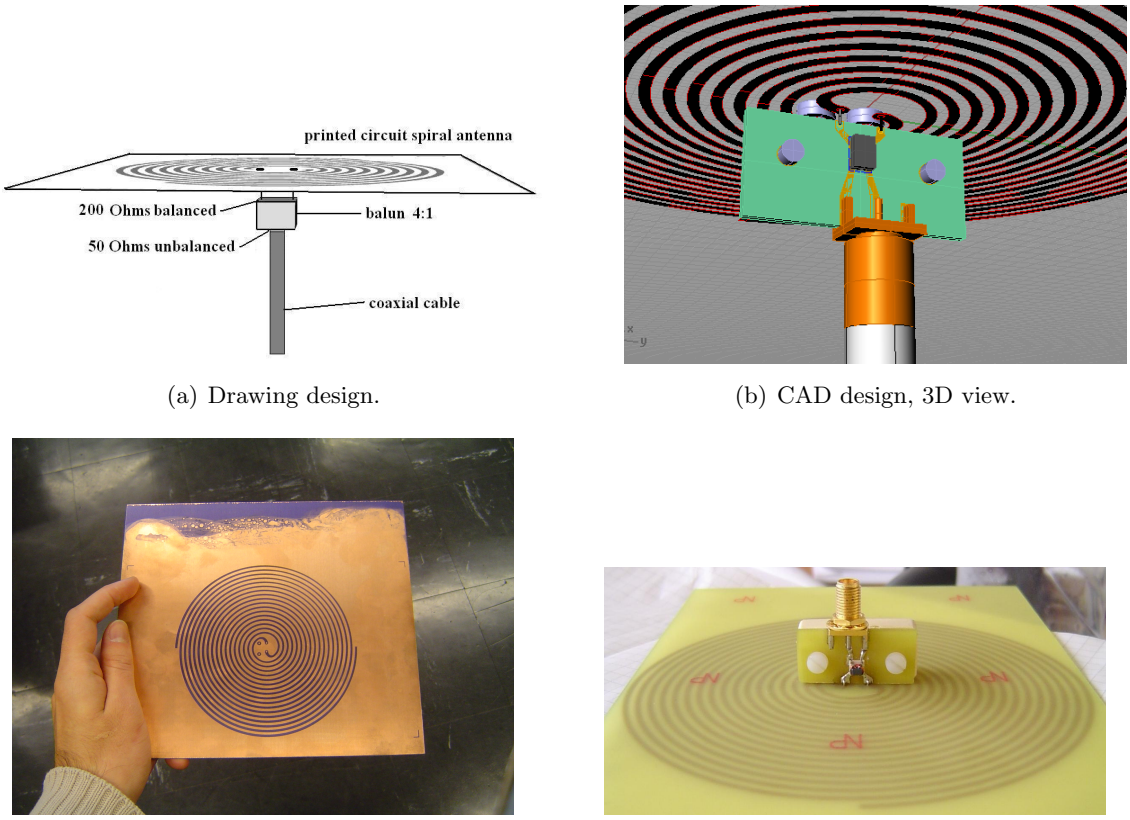

(a) Drawing design.

(b) CAD design, 3D view.

(c) Printed circuit board before copper etching.

(d) Final antenna prototype design.

Figure 2.10: *Design of the spiral antenna prototype.*

phase dispersion is roughly under 10 degrees. Consequently, when comparing array measurements with modeling, differences between the uniformly excited array and a practical measured array can be expected. Indeed, the various transformers may not have the same characteristics, especially the phase. It means that the antenna elements do not radiate with the same excitation coefficients. So, particular attention must be payed when the measured array radiation pattern would be analyzed. This point will be discussed further in Chapter 3 for array measurements.

Gain measurement setup

The gain of one of the antenna prototypes has been measured using the comparison method explained in [3]. The gain of the antenna under test (G_{AUT}) can be calculated from the known gain of the reference antenna (G_{ref}) as given in Eq. 2.3. So, the power P_{ref} of a biconical antenna (see

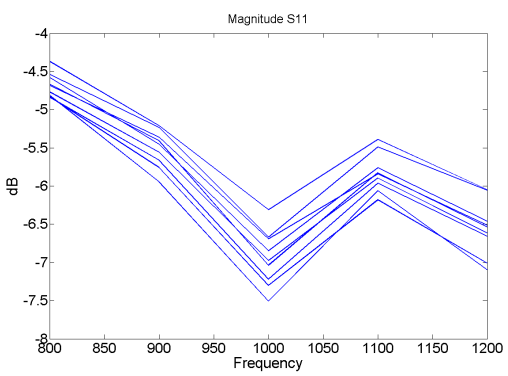

(a) Measured S_{11} magnitude of the 9 antenna prototypes.

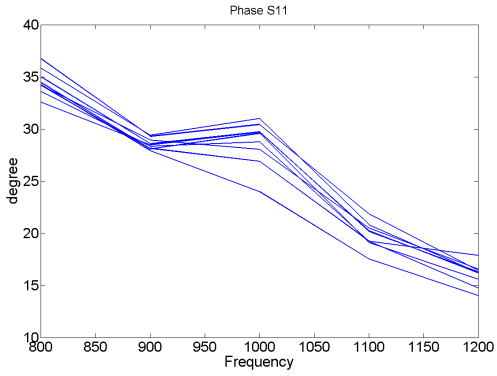

(b) Measured S_{11} phase of the 9 antenna prototypes.

Figure 2.11: *S_{11} coefficient of the spiral antenna measurements.*

appendix) has been measured with exactly the same measurement devices as used for measurements of the power P_{AUT} of the spiral antenna, in order to calculate the gain of the spiral antenna. Gain versus frequency is plotted in Fig. 2.12 at 850, 1000 and 1100 MHz, for the measured biconical antenna, the measured spiral antenna and the modeled spiral antenna. Few dBs differences can be observed between the modeled and the measured spiral antenna. It is supposed that it corresponds to the few dBs of the transformer insertion loss characteristics (see appendix).

$$G_{AUT} = \frac{P_{AUT}}{P_{ref}} G_{ref} \tag{2.3}$$

Radiation pattern measurements

The radiation patterns of the 9 antennas have been also measured in Supelec using the spherical test facility "Sesame" dedicated to near-field measurements. The measurement system is based on a circular arch with a 5 m diameter, along which a probe can move on a 170° course (see Fig. 2.13(b)). Measurements can be performed within a 0.1 to 30 GHz frequency band. The device under test is placed at the center of the arch using a mast laid itself on a turntable. This measurement setup allows a spherical scanning, necessary for omni-directional sources characterization. Taking into account its dimensions, Sesame can be also used directly in far-field conditions for many applications.

The measurements results are compared with those obtained by modeling. Radiation patterns plotted in the elevation plane as well as 3D view are presented at 800 MHz (Fig 2.14), 900 MHz (Fig 2.15) and 1200 MHz (Fig 2.16), for both RHCP and LHCP component of the radiated field. The 2D patterns have been normalized to 0 dB. It must be noticed that measurements can not

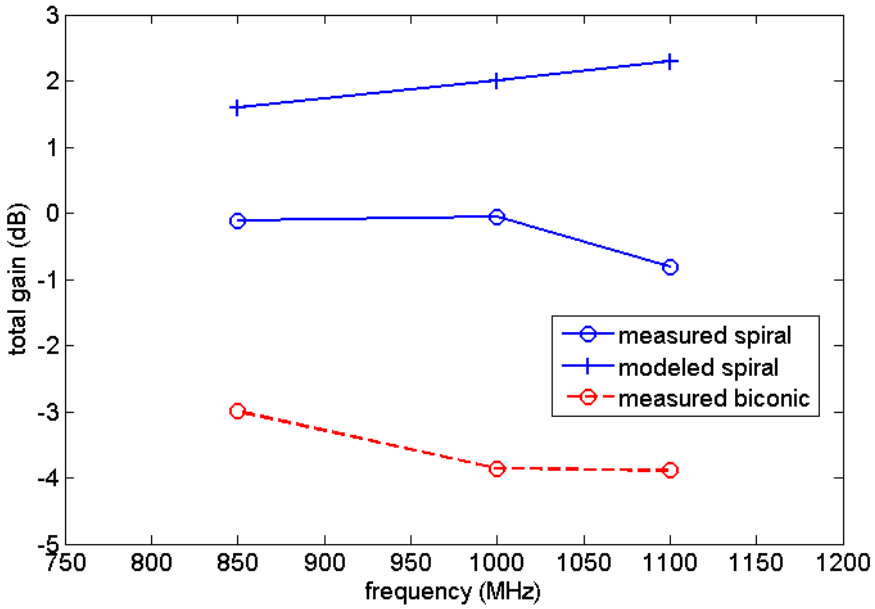

Figure 2.12: *Gain of a measured spiral antenna obtained from a measured biconical reference antenna. Measurements and modeling results are compared for various frequencies.*

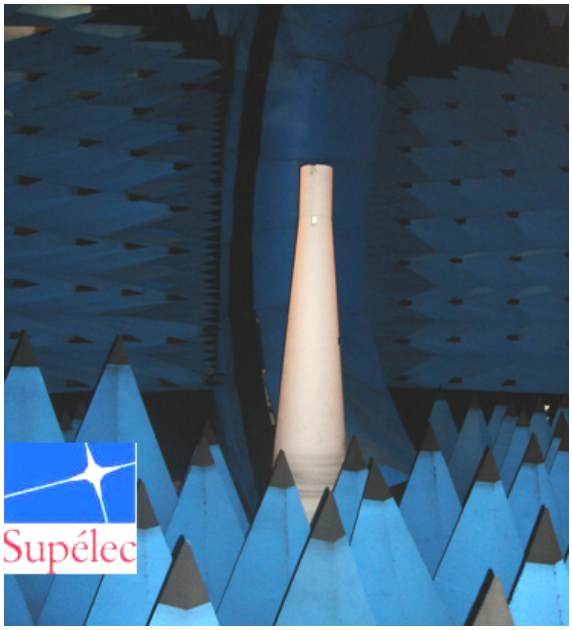

(a) Spherical test facility "Sesame" in Supelec

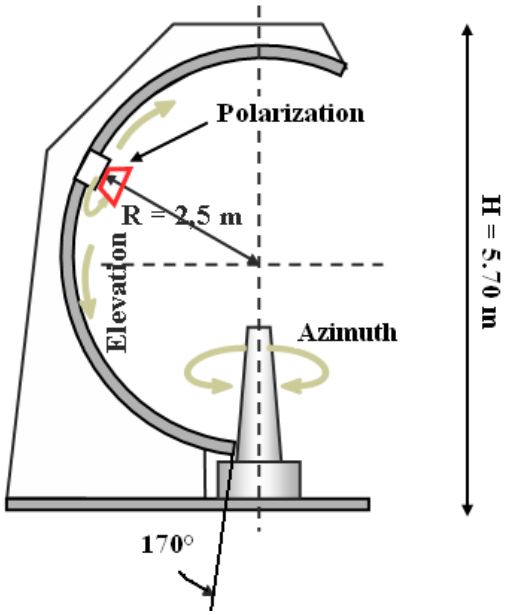

(b) Spherical test facility dimensions

Figure 2.13: *Spherical test facility configuration*

be achieved at elevation angles between 170° and 180° because of the limitation of the test facility configuration (see Fig. 2.13(b)). That explains the lack of measured value at these angles.

Radiation pattern comparison

First, comparing the 2D results at various frequencies (see Fig 2.14(a), Fig 2.15(a) and Fig 2.16(a)), some discrepancies can be observed in the measured radiation pattern. The main lobe is roughly reconstructed, but big divergences occur for the back lobe. This may be due to the lower values of the radiated field, but it must be also kept in mind that the patterns have been normalized to the maximum value, i.e. the main lobe.

Then, it can be noticed that the feeding cable is vertically aligned. It means that, at the elevation angles 90° and 270°, the vertically polarized measuring probe would also receive the contribution of radiations coming from the cable. That could explain the high differences at this two angles.

The 2D figures demonstrate that the measured main lobe shape and its relative level fit to the modeling results. The RHCP component seems to match more accurately, probably due to the presence of the cable on the RHCP radiation side. Furthermore, degradations of the pattern shape can be observed at high frequencies that may be due to the transformer and cable interferences.

The 3D views plotted in Fig 2.14(b), Fig 2.15(b) and Fig 2.16(b)) helps in the qualitative comparison between measurements and modeling results. It can be seen that the main lobe is reconstructed for both polarization. Then, the spatial separation of the polarized field is still effective and this effect increases at the highest frequency as predicted. The 3D plot also confirms the round shape of the main polarized lobe, even if, at high frequencies, strong perturbations can be seen.

Conclusion on the antenna design

The designing of spiral antenna prototypes for measurements purpose has shown that the feasibility of identical antennas was quite challenging since characteristics from one antenna to an other change in phase and magnitude. The choice of a transformer component in a surface mount technology which provides an easy implementation and a readily available solution, does not require a sophisticated design. However, it may not be the best solution for such applications since its characteristics are difficult to measure (non reciprocal component, with balance and unbalance access). Furthermore, the return loss of the transformer component degrades severely the antenna S_{11} coefficient. Hence, improvement in the design of a matching and an unbalance to balance transition might facilitate the manufacturing of identical antennas.

2.2.3 Conclusion on the practical approach

Measurements results have shown that the characteristics of the measured spiral antennas matched those of modeling. The gain as well as the radiation pattern are respected within the considered bandwidth. Thus, the proposed design offers a simple solution to be used in a conformal array configuration for measurements without ground plane, as long as the cable remain perpendicular to the antenna plane. Furthermore, modeling results and especially the polarization characteristics of the radiated field have been confirmed by measurements. Finally measurements have demonstrated that the actual design of the antenna element is clearly not suitable to be mounted on an airship, since the coaxial feeding needs to be perpendicular to the antenna plane. Thus, if a conformal array on airship measurements have to be manufactured, other solutions have to be found to solve this issue.

2.3 Feeding and data link issues

The feeding of the conformal array mounted on the airship is one of the main challenges to overcome. Indeed, a coaxial feeding at the spiral center is not possible since it must be perpendicular of the antenna plane. Hence, solutions have to be elaborated in order to demonstrate the feasibility of using a spiral antenna array mounted on airship with a suitable associated feeding circuit.

The first issue is the conception of the data link circuit used to collect the data from the array elements to the processor placed for convenience in the airship gondola (see Fig. 2.17(a)). The link cables must be light and also must not interact with the radiating antennas. So, an optical solution could be used to solve the interaction issue. Consequently, analog to digital converters as well as electric to optic converters will be required. It may be possible to design a system on chip (SoC) miniaturized to be placed in the center of the spiral. Indeed, because of the array scanning condition, the maximum frequency is limited. This means that the center part of the spiral is not fully used and a small inner part of the spiral might be removed, without disturbing the functioning of the spiral at lower frequencies. Nevertheless, this has not been demonstrated yet and further developments will be necessary.

Another solution is to find an antenna design fed in a coplanar configuration. Thus, existing designs have been investigated and a new design has been proposed during the Master thesis of Karim Louertani at SONDRA [6].

2.3.1 Coplanar feeding solutions

An interesting design of a coplanar 3-arm spiral antenna which could solve the issue of using a cable perpendicular to the antenna plane has been proposed by Muller and Sarabandi [5]. The 3-arm spiral has also the advantage to be fed by an unbalanced transmission line, such as a coaxial line or coplanar waveguide, and therefore an external balun is not needed at the feed point. The antenna can be directly matched to any practical transmission line characteristic impedance and therefore external matching networks are not required. This is accomplished by feeding the antenna at the outer radius by a coplanar waveguide (CPW) transmission line and tapering it toward the center. However, even if the wideband performances of this antenna have been demonstrated, the bandwidth does not correspond to that of a center-fed 2-arm Archimedean antenna. Indeed, the lowest frequency of this design has been empirically found to be three times higher in [5] than its equivalent center-fed 2-arm antenna. It means that this antenna should not be suitable for scanning array applications respecting the half wavelength of distance between elements. Thus, the design of the 3-arm spiral will be first modeled using FEKO in order to validate and analyze the results found in [5]. Then, a new design will be proposed to solve both the perpendicular feeding issue and to radiate within the desired frequency bandwidth.

Modeling of the 3-arm spiral antenna

A 3-arm spiral antenna fed at the outer radius has been designed (see Fig. 2.18), inspired by the 3-arm antenna design of Muller and Sarabandi [5]. Each arm has 10 turns and the line width is equal to the interspace between two arms. The diameter of the spiral is 0.25 m, which corresponds to a F_{min} of 400 MHz for a 2-arm center-fed spiral. Three 50 Ω loads are added at the center of

the spiral as recommended in [5]. The excitation is placed at the center line of the external feeding arm in order to model a current excitation of a coaxial with the ground connected to the external line of the cable.

The VSWR as well as the components of the complex impedance $\Im(Z)$ and $\Re(Z)$ are plotted in Fig 2.19. It can be noticed that the input impedance within the bandwidth [900-1500] MHz is constant and has a value near 200 Ω like a complementary spiral antenna. The F_{min} is equal to 900 MHz (see Fig. 2.19(a)), corresponding to 2.25 times the F_{min} of a 2-arm center-fed spiral with the same diameter. So, the frequency shift is observed even if the expected coefficient 3 given by Muller and Sarabandi is not validated. That might come from the small differences between the two designs (number of turns, line width, presence of a load, tapered line), since the original design is not accurately defined in the paper. Resonances in the VSWR values can be seen within the frequency band [400-900] MHz corresponding to the strong variations in phase and magnitude impedance seen in Fig. 2.19(b).

Symmetry considerations

Investigations have been led to understand the bandwidth shift. A parametric study, varying the number of turns, the line width to interspace ratio, the number and values of loads at the spiral center, the length of the outer feeding line, has concluded that any of these parameters allow to radiate in the same bandwidth as a 2-arm center-fed spiral. In addition, the modeling of a 2-arm outer-fed antenna and of a 3-arm center-fed antenna brings to the conclusion that the higher value of F_{min} appears when the antenna is outer-fed.

To understand this, the current distribution has been analyzed according to the frequency for the 2-arm center-fed antenna and the 3-arm outer-fed antenna. A center-fed spiral has a current distribution at low frequency over its whole surface, whereas at high frequency the current is concentrated in the center of the spiral. It means that when frequencies are low, the current is reflected at the edge of arms and thus the spiral does not radiate properly. The configuration of an outer radius fed antenna is different since the excitation is external to the spiral, at the end of the coplanar line (see Fig. 2.18), thus the distribution of current cannot be the same. At low frequencies, the current is distributed over the whole surface and reaches the center of the spiral loaded by the three 50 Ω loads. At high frequencies, the current is not distributed at the center, but on the perimeter of the spiral as it can be seen in Fig. 2.18 at 1.2 GHz.

Another effect can be taken into account. The spiral antenna radiation condition is that the current on symmetrical arms must be in phase. In the case of an outer fed antenna, the various arms do not have the same length since they start from exactly the same angle in the outer radius (represented by the point **A** in Fig. 2.18) and stop at different angles at the center of the spiral. Typically, for a 3-arm spiral antenna, the difference of length between the second arm (middle) and the first one will correspond to a distance $d_{12} = \pi D/3$ (point **A** to point **B** in Fig. 2.18), where

D is the diameter of the spiral. The difference of length between the third arm (external) and the first one will correspond to a distance $d_{13} = 2\pi D/3$ (point **A** to point **C** in Fig. 2.18). Thus, at low frequencies, the distribution of current does not respect the in-phase condition, due to the lack of symmetry. Phase compensation should be investigated at the feeding point to compensate the delay introduced by the path length.

Radiation performances of the proposed design have also been studied. Fig. 2.20 shows the radiation pattern in the elevation plane (at $\varphi = 0°$) for various frequencies and the 3D radiation pattern at 510 MHz. As it can be seen, the spiral antenna radiates over a wideband of frequency but the radiation pattern shape is strongly modified and looses its symmetry. The outer feeding line and the non symmetric geometry of the spiral produce radiation pattern with a non constant shape

So, modeling has confirmed the main properties results of the design presented in [5]. Furthermore, the modeling tool has allowed to observed the distribution of current for various spiral configuration. It has been highlighted that the center-fed behavior was completely different from the outer-fed design because of a new current distribution law according to the frequency. The bandwidth shifted at higher frequencies may be an inherent consequence of the outer-fed geometry due to the path length differences between the three arms. Then, the symmetry in the spiral distribution of current is of a great importance to explain and design an antenna able to radiate at lower frequencies.

2.3.2 4-arm spiral antenna

In order to keep the symmetry of the spiral, a 4-arm spiral antenna design is proposed and can be seen in Fig. 2.21(a). It is obtained from a 2-arm outer-fed spiral antenna interleaved with its rotationally symmetric. The symmetric design should lead to less degradations in the radiation pattern and a more in-phase distribution of current. It uses the coplanar advantage of the previously proposed 3-arm antenna, except unbalanced transmission line that necessitates three arms. The 4-arm spiral has been modeled with the following parameters: each arm has 5 turns, the line width is equal to the two arms interspace and the diameter is 25 cm. It must be pointed out that no load has been used at the end of each arms in this model. The four arms edges in the center of the spiral are left open.

The 4-arm spiral antenna has two ports excited with a 180° phase difference in order to produce an in-phase current distribution. The distribution of current given by FEKO according to the frequency has been particularly observed and an example at the spiral center is represented in Fig. 2.21(b). Thanks to the symmetry of arms 2-4 and 1-3 the density of current is also symmetric and can be in phase. This has been observed at each frequency and thus radiations should be enhanced.

Fig. 2.22(a) shows the VSWR computed with a 200 Ω and 300 Ω matching impedance. It can be seen for both cases that $F_{min} = 360$ MHz and that the VSWR value is under 2 over the whole bandwidth. So, it means that using two excitation ports phased with a 180° difference, the F_{min} of the center-fed 2-arm spiral is even lower than the 2-arm center fed design. It can be noticed that the input impedance plotted in Fig. 2.22(b) exhibits a higher real part than the center-fed 2-arm spiral. This is in good agreement with [58] mentioning an increase in impedance with the number of arms for a given mode.

Performances of the 4-arm spiral antenna in terms of radiation and polarization are also estimated. The RHC polarized gain radiation pattern is plotted in the elevation plane ($\varphi = 0°$) in Fig. 2.23(a) and in the azimuth plane ($\theta = 90°$) in Fig. 2.23(b). It can be seen that the symmetry of the radiation pattern is preserved at any frequency. In Fig. 2.23(a), the polarized radiation pattern illustrates the fact that at 600 MHz, the back lobe is bigger than at 500 MHz.

The value of both RHC and LHC polarized gain is plotted according to the frequency in Fig. 2.23(c) for a direction ($\theta = 0°$, $\varphi = 0°$), and in Fig. 2.23(d) for a direction ($\theta = 45°$, $\varphi = 45°$). The RHCP is the co-polarized gain in the direction ($\theta = 0°$, $\varphi = 0°$). Its value is quite good for the considered bandwidth, however, the level of the cross-polarization is not low enough. Within the frequency band [400-550] MHz, the LHC cross-polarization gain value is roughly 4 dB lower than the co-polarization value for the ($\theta = 0°$, $\varphi = 0°$) direction case. For a direction ($\theta = 45°$, $\varphi = 45°$), the cross-polarization roughly reaches -7 dB compared to the co-polarization, within the same frequency band. Hence, the 4-arm spiral antenna exhibits poorer performances on low cross polarization level. So, even if the radiation pattern has properties similar to the initial center-fed 2-arm spiral antenna and is rotationally symmetric, the cross-polarization level is not as low as expected.

The issue of two excitation ports instead of one must also be underlined. The 4-arm spiral antenna requires two excitations at different locations with a 180° phase difference. Thus, design of the array must take into account the double feeding for each antenna element and the compactness should be increased due to the number of cables required. Then, it is important to control the phase of the two access accurate enough to match the performances obtained by modeling. The difficulty of a practical realization should be consequently enhanced due to the phase reference at two different locations. However, the two excitation ports could also allow to use the 4-arm spiral antenna as a reconfigurable antenna using either one port, or the other. Further studies should be perform to fully exploit the possible performances of such an antenna.

2.4 Conclusion of Chapter 2

In this chapter, the design of the array element has been studied. A research of a technology compatible with the host platform has led to a selection of four wideband antenna candidates which have been compared using the modeling tool FEKO. While the allowed array bandwidth is almost similar for each candidate, it has been shown that the polarization criterion was the most determining. Indeed, it has been stressed that bowtie like antennas suffer from a high cross-polarization level if directions out of the electric and magnetic planes of the antenna are considered. On the other hand, the spiral has demonstrated a specific skill that maintains a quasi constant cross-polarization level over a half space. This characteristic suits perfectly to conformal configurations, where an element orientation differs according to its position in the array. For this reason, the spiral antenna has been chosen as the array element.

Then, the conception of a spiral antenna prototype has been conducted, in order to validate the modeling results. The issue of the feeding cable presence has been highlighted as the spiral is used without ground plane and has both front and back lobes. The measurements have shown that if the cable is kept perpendicular to the antenna plane, its influence is minimized.

A microwave transformer component has been purchased and integrated to the antenna design to match the 200 Ω of the antenna impedance and to provide a balanced to unbalanced transition. Individual measurements of the transformers would have been helpful to specify the insertion loss and return loss values. However, the non trivial measurement procedure has not been achieved because of lack of time.

It has been found that the measurements of the antenna S_{11} as well as its gain fitted quite well to the values of modeling. Some differences have been observed and could be explained by the insertion loss introduced by the transformer. Furthermore, the measurements of the radiation pattern has shown that the shape of the antenna pattern was respected with some discrepancies due to the presence of the cable. All the antenna samples exhibit similar performances that would ensure a uniformly excited array.

The feeding of the antenna elements on airship has been also discussed. Indeed, using cable perpendicular to the antenna plane, for center fed spirals mounted on an airship, is not feasible. Hence, from an existing design [5] found in the literature, a study has been led within the framework of the master internship of Karim Louertani [6]. The initial design which allows to feed the spiral in the same plane than the antenna has been studied and modified to suit our requirements.

The importance of the current distribution has been emphasized. It is thought that the outer-feeding arm introduces a phase shift perturbating the current distribution. Hence, a more symmetric design has been proposed with two outer-feeding arms. This innovative design has been modeled and results have shown that its wideband performances in an array are superior to the previous one. However, the cross-polarization level must still be improved.

So, the work done in this first part allows to determine the technology and the shape of the array elements on the airship. A 134-element array of spiral antenna has been proposed, located in the front part of the airship and has a half ellipse shape (see Fig. 2.24). The choice of spiral antennas would enable a frequency band between 450 and 600 MHz.

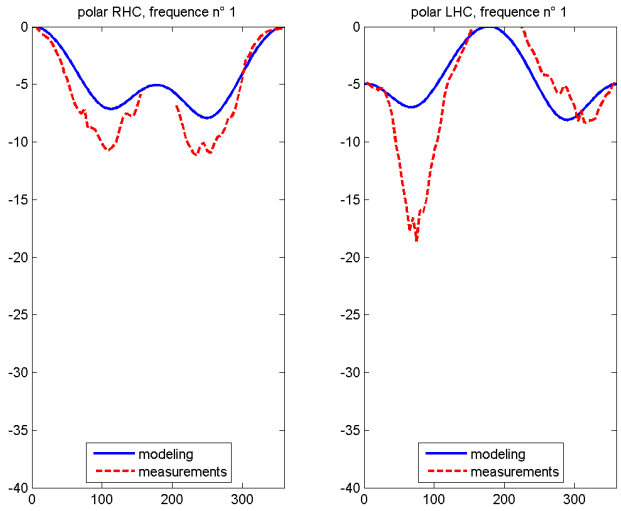

(a) Elevation pattern, 800 MHz, RHCP (left) and LHCP (right)

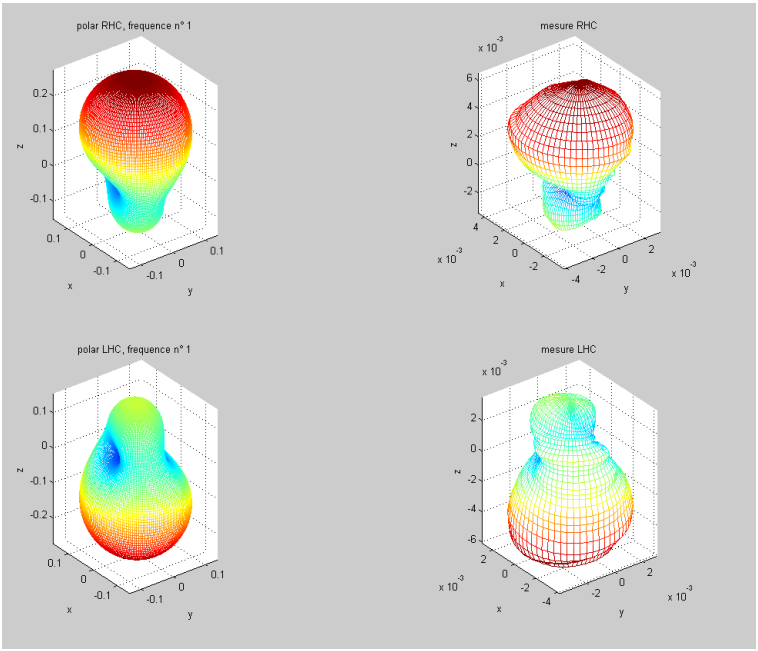

(b) 800 MHz, RHCP (top) and LHCP (bottom), modeling(left), measurements (right)

Figure 2.14: *Single antenna radiation pattern comparison between measurements results and modeling results at 800 MHz.*

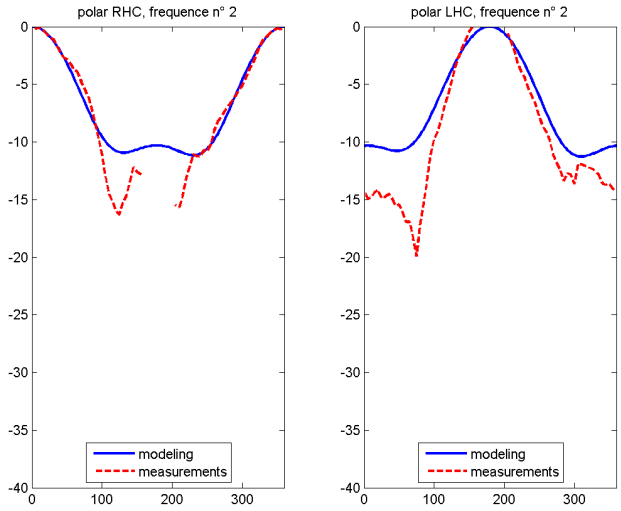

(a) Elevation pattern, 900 MHz, RHCP (left) and LHCP (right)

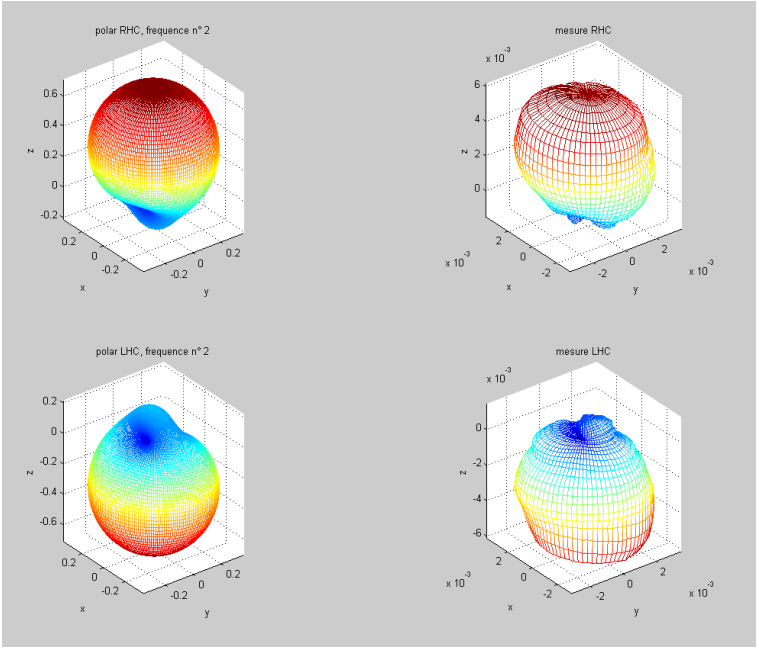

(b) 900 MHz, RHCP (top) and LHCP (bottom), modeling(left), measurements (right)

Figure 2.15: *Single antenna radiation pattern comparison between measurements results and modeling results at 900 MHz.*

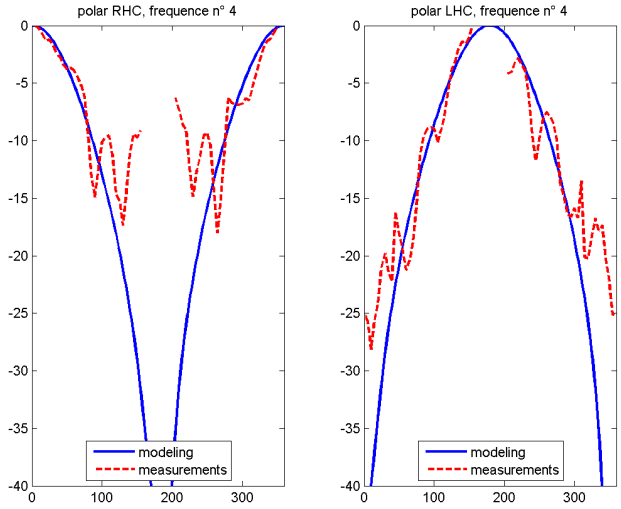

(a) Elevation pattern, 1200 MHz, RHCP (left) and LHCP (right)

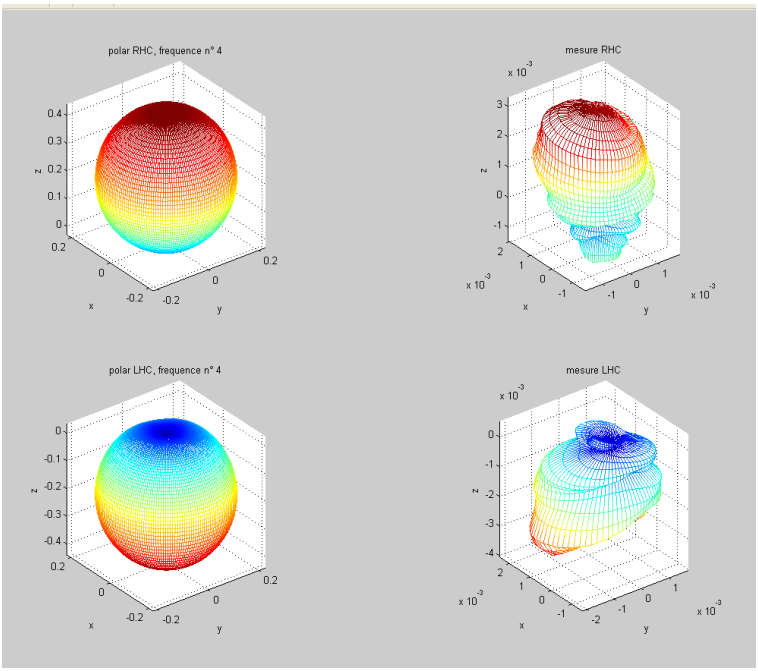

(b) 1200 MHz, RHCP (top) and LHCP (bottom), modeling(left), measurements (right)

Figure 2.16: *Single antenna radiation pattern comparison between measurements results and modeling results at 1200 MHz.*

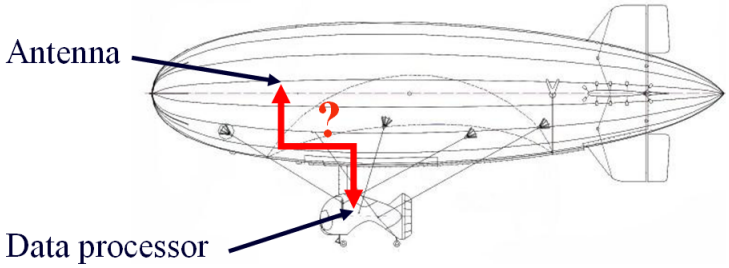

(a) data link issue.

Figure 2.17: *datalink.*

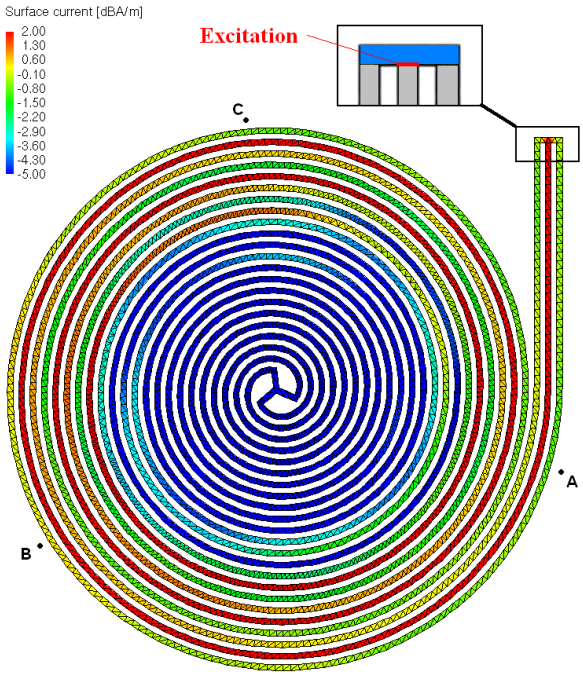

Figure 2.18: *3-arm outer-fed antenna design exited by a CPW line. Current distribution is represented at 1.2 GHz.*

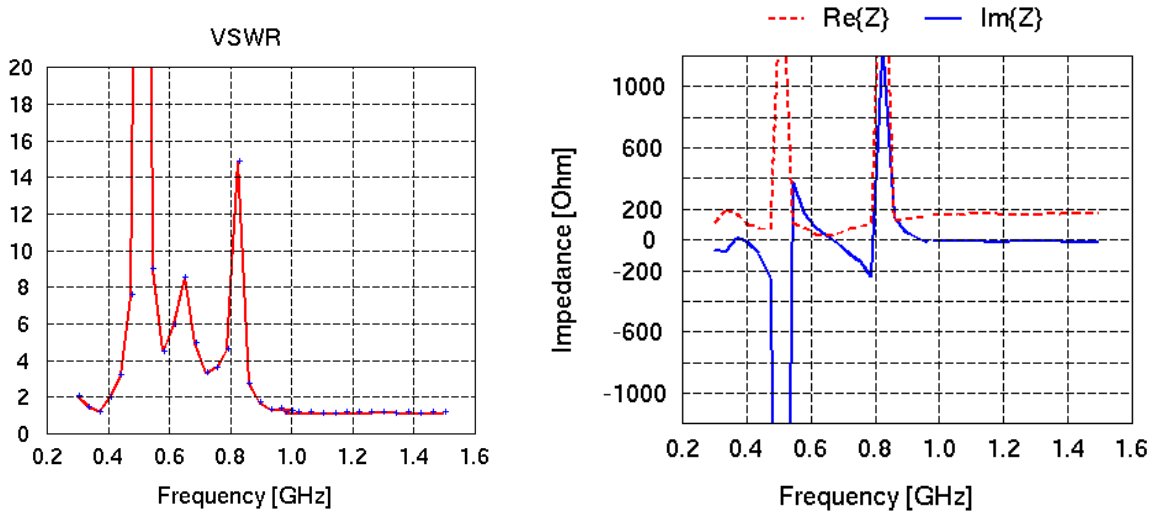

(a) VSWR of the 3-arm spiral antenna, referenced to 200 Ω.

(b) Real part and imaginary part of the input impedance.

Figure 2.19: *Bandwidth of a 3-arm antenna with a diameter D=0.25 m.*

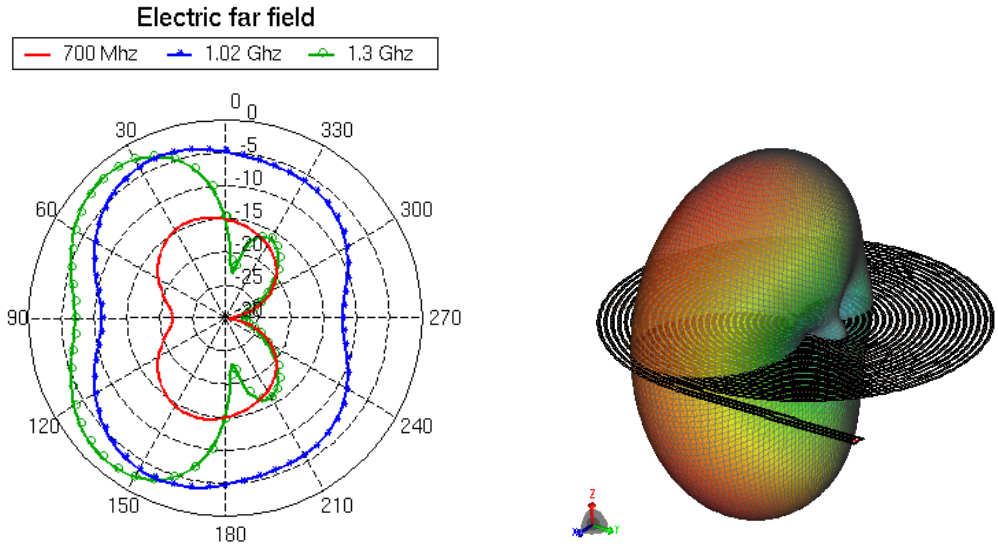

(a) 2D elevation pattern in the elevation plane (at $\varphi = 0°$) for various frequencies.

(b) 3D radiation pattern at 510 MHz.

Figure 2.20: *3-arm antenna radiation characteristics.*

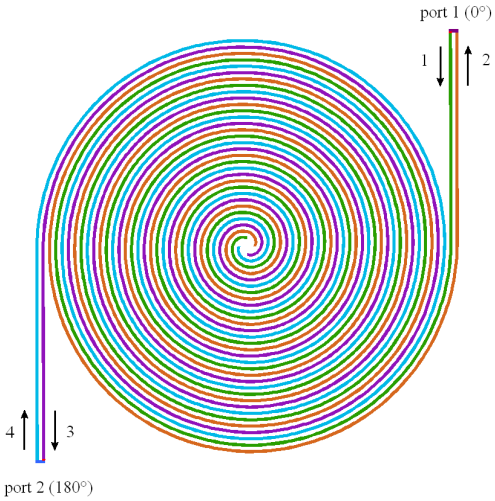

(a) 4-arm spiral antenna coplanar design (diameter D=0.25 m).

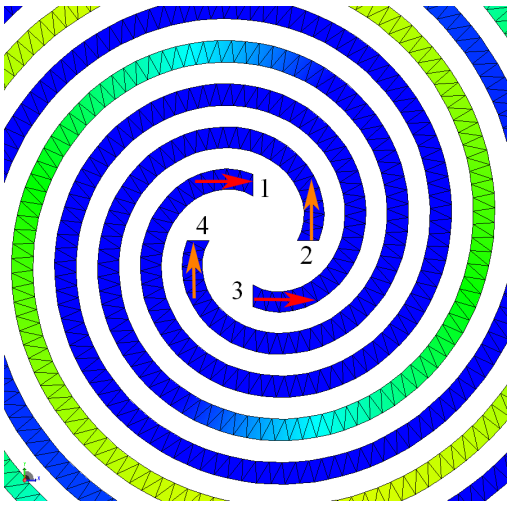

(b) Zoom in the center of the 4-arm spiral antenna. Currents on each symmetrically opposite arm (1-3 and 2-4) are in phase.

Figure 2.21: *4-arm antenna design and current distribution.*

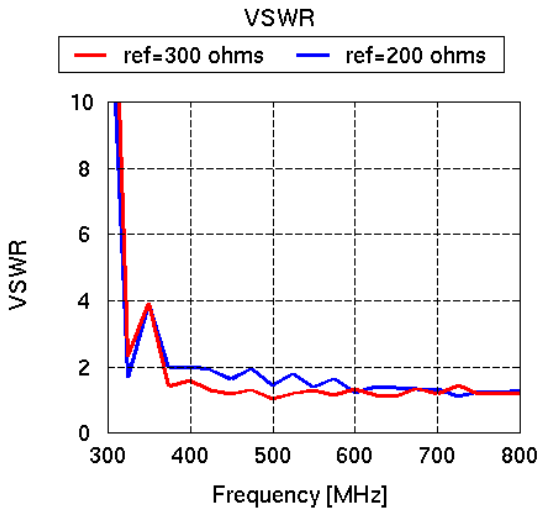

(a) VSWR of the 4-arm spiral antenna calculated with a 200 Ω and a 300 Ω reference.

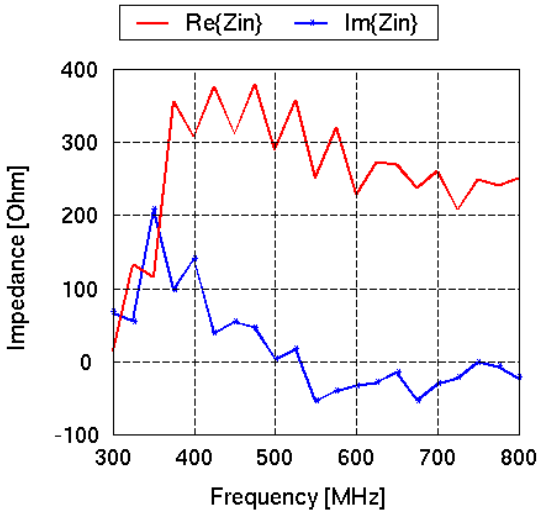

(b) Input impedance of the 4-arm spiral antenna.

Figure 2.22: *4-arm antenna.*

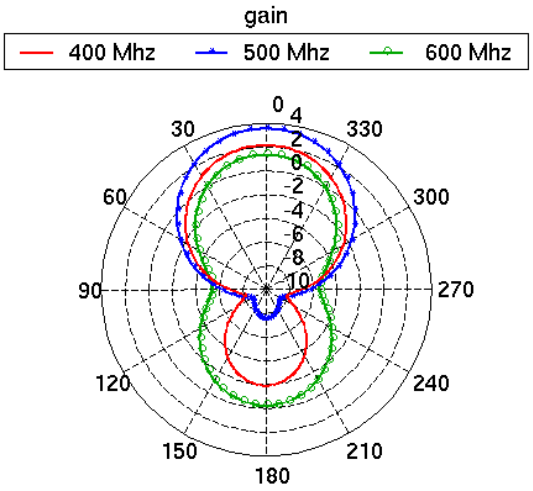

(a) RHC polarized gain in the elevation plane $\varphi = 0°$.

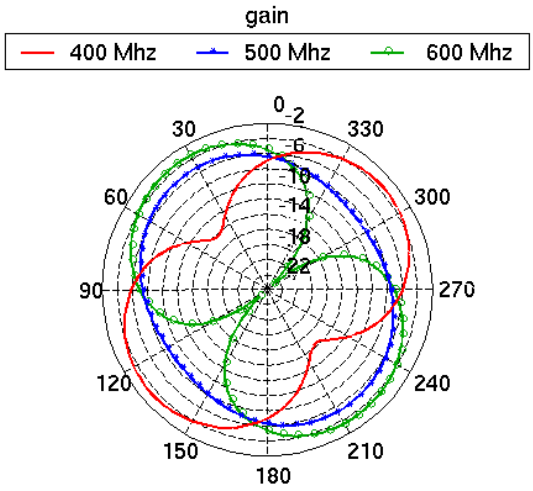

(b) RHC polarized gain in the azimuth plane $\theta = 90°$.

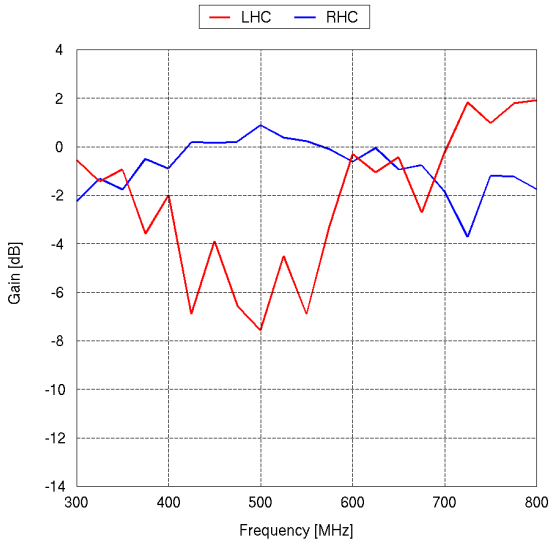

(c) RHC and LHC polarized gain in the direction ($\theta = 0°$) according to the frequency.

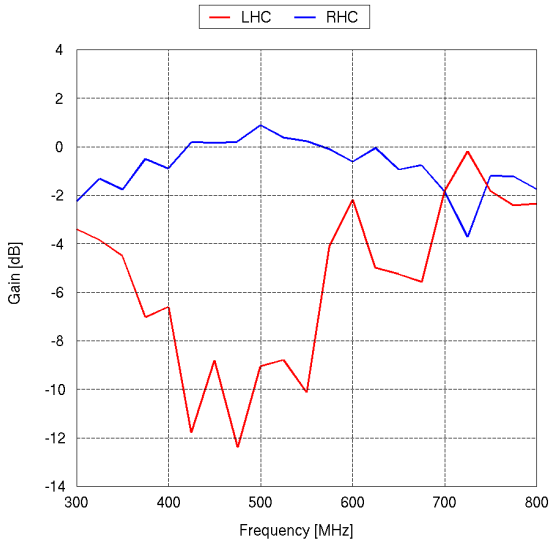

(d) RHC and LHC polarized gain in the direction ($\theta = 45°, \varphi = 45°$) according to the frequency.

Figure 2.23: *4-arm antenna radiation characteristic.*

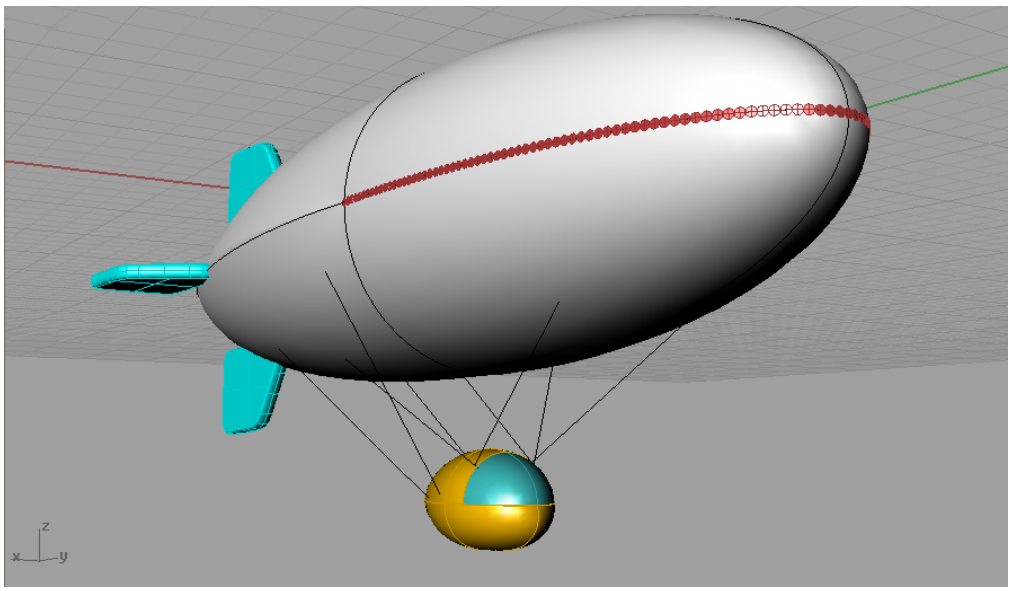

Figure 2.24: *Artistic view of the proposed conformal array location and shape.*

Chapter 3

Computation of the Conformal Array Radiation Pattern

The shape of an array radiation pattern depends on the relative physical positioning of the elements and their relative electrical excitations. These two parameters are generally used to exercise control over the radiation pattern [64]. It means that, from a desired radiation pattern, the corresponding set of electrical excitations has to be found. The direct approach consists in computing the radiation pattern from both the element positioning and the excitation coefficients applied. In addition, the orientation of elements and the possible interactions must be also taken into account in the conformal case. So, a modeling tool able to compute the conformal array radiation pattern is required.

The first solution would be to use the commercial tool FEKO, as previously done for the single antenna modeling. FEKO is based on the MoM and gives the electromagnetic response of any structure [65]. The MoM scales as N^2 in terms of memory to store the impedance matrix, with N the number of unknowns. Moreover, the CPU-time to solve the linear set of equations requires N^3. Since the chosen array size is N=134, the MoM will require too much memory and CPU-time. Some accelerating methods like the Multilevel Fast Multipole Method (MLFMM), allow the reduction in memory requirements to solve a large structure modeling issues. Nevertheless, even if faster computers or accelerating method are used, the modeling must be repeated for each set of excitation coefficients, i.e. each direction, and has to be also repeated for optimization techniques. Indeed, the set of excitation coefficients can be found using a pattern synthesis method that requires many computation of the radiation characteristics. Thus, the full use of a modeling commercial tool is not a suitable approach.

So, a simple and efficient complementary method must be developed to predict the array radiation pattern. The method to compute the array response has to be valid for frequencies within the 400-600 MHz bandwidth. Furthermore, according to the specific case of the half ellipse array shape,

the inward radiation of antennas as well as the polarization must be also taken into account. In this chapter, the array configuration analysis and the evaluation of the coupling values are described. Then, a modeling tool to compute the radiation pattern of the conformal array will be developed and the accuracy of the method will be evaluated.

3.1 Modeling of coupling

Mutual coupling is specific to any array and is often difficult to evaluate. It is known that coupling decreases when the distance between elements increases. Coupling also depends on the element characteristic and the respective orientation of two neighboring elements. In the considered case, where antennas are mounted on the airship hull, the half ellipse configuration of the array and the lack of ground plane introduce new sources of coupling. On the other hand, the lack of ground plane simplifies the calculations and would minimize coupling between close elements. The coupling values may also depend on the array curvature. The ellipse has various radius of curvatures and, thus, coupling differs from one part of the array to another part. In Fig. 3.1, it can be seen that zones **A** and **B** have low curvature, corresponding to the quasi planar case. But, zone **C** has a high curvature and should be analyzed more carefully. Furthermore, coupling may also occur between zones **A** and **B**, since no metallic ground plane reflects the radiation. Consequently, before developing any radiation pattern computation method, it is important to evaluate the coupling between the different elements and to understand how they are influenced by frequency, curvature and element position parameters. Thus, coupling effects are investigated, based on the computation of the $|S_{ij}|$ coefficients between two spiral antenna ports, with i and j the numbers of the considered elements. The distance center to center $d = 0.25\ m$ is kept along the array, and is the same whatever the curvature is.

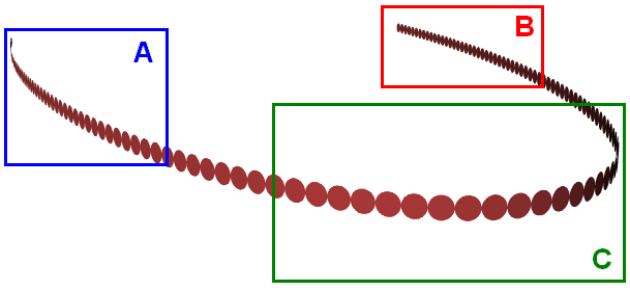

Figure 3.1: *1D half-ellipse conformal array of spiral antenna elements. Low curvature zones **A** and **B**, high curvature zone **C***

3.1.1 Wire approximation, modeling of coupling

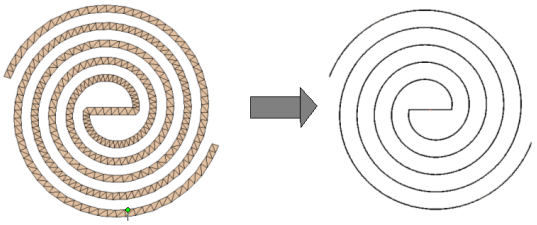

(a) Wire approximation: A microstrip spiral divided into triangles element is replaced by a equivalent spiral divided into wire segments.

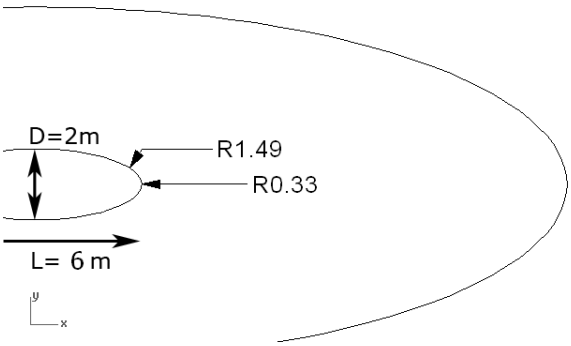

(b) Scale factor 1:5 applied to have the 19-elements array with the same shape than the 134-elements array. The minimum radius of curvature reaches 0.33 m at the highest zone of curvature.

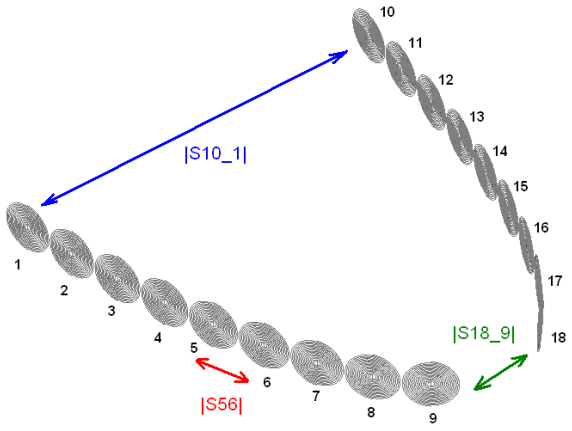

(c) Model of the 18-elements array. Wire spirals are used and scale factor 1:5 has been applied.

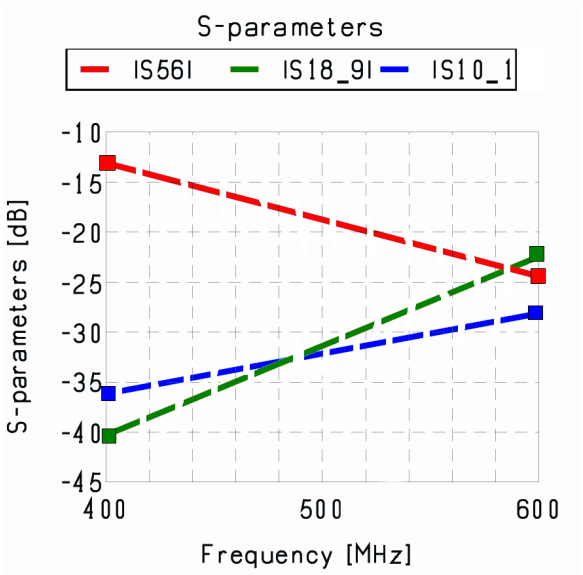

(d) $|S_{ij}|$ coefficients values at 400 MHz and 600 MHz corresponding to the coupling between elements 5 and 6, 18 and 9, 10 and 1.

Figure 3.2: *Modeling of the coupling, wire spirals approximation*

The modeling tool has limited capabilities to model an array with a high number of elements.

However, it is possible to model spirals using wire segments instead of triangles to minimize the computation time. Indeed, wire decomposition requires 1 current value per wire segment, rather than three current values for a triangle element [65]. Thus wire spiral antenna with the same geometry, as shown in Fig. 3.2(a), will be used instead of microstrip spirals, allowing to compute a 18-elements array. The desired design is a 134-element array on an ellipse of 10 m diameter and 30 m length. The array size considered for modeling has only 8 elements. Thus, it is necessary to reduce the ellipse dimensions to keep a similar radius to curvature ratio and a scale factor 1:5 is applied as depicted in Fig. 3.2(b). The new configuration is an ellipse of 6 m length and 2 m diameter. A smaller size means a smaller distance between opposite elements, a higher curvature, thus, the coupling effects should be increased.

The coupling values are evaluated at two frequencies, 400 and 600 MHz, corresponding to the lower and upper bound of the considered bandwidth. Fig. 3.2(c) shows three characteristic types of coupling. The S_{10-1} value is the magnitude of the coupling value between element 1 and element 10 and represents the coupling between elements on opposite sides. The S_{18-9} value is the coupling value between element 18 and element 9 and represents the coupling between element on opposite sides in the strongly curved region. The S_{5-6} value is the coupling value between element 6 and element 5 and represents the coupling between adjacent elements. The 18-element wire spiral array is modeled with FEKO.

The results are depicted in Fig. 3.2(d). First, it can be seen that coupling between adjacent elements (S_{5-6}) are stronger than other types of coupling. Then, the values of any cases of coupling are under -10 dB. Because of the lack of frequency points, it is not possible to conclude accurately on the evolution of coupling according to the frequency. However, it can be observed that at 600 MHz, the difference between the different types of coupling seems to decrease.

3.1.2 Modeling of the strongly curved array region

The previous results have been obtained using an approximated wire model of the spiral. However, the practical spiral is based on microstrip technology and should be modeled with surface triangle elements instead of wires. Furthermore, the high curvature zone **C** shown in Fig. 3.1 has not been completely modeled in the previous example. So, a circular 1D array with identical antennas, radiating RHCP outward (co-polarization configuration) is now considered. Only an 8-elements array has been modeled with MoM for time consuming reason. Coupling effects are investigated based on the computation of the S-parameters between spiral antenna ports as in the previous example.

The angle of curvature α is defined in Fig. 3.3 as the angle between two adjacent antenna elements of the array. In order to model the coupling effect on the airship, 8-antenna arrays are modeled for various curvature and each represents a part of the complete array on the real size

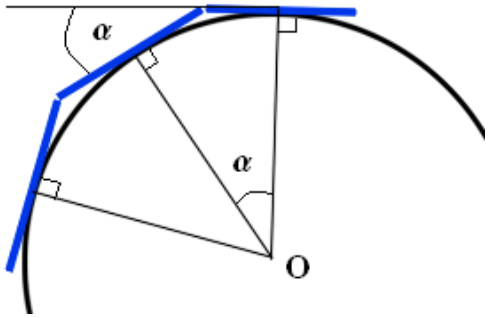

Figure 3.3: *Angle of curvature α, defined as the angle between the two spiral planes. α is also equal to the angle between the perpendicular to the two spiral elements.*

ellipse. Fig. 3.4(a) shows the arrays dimensions and geometry at different curvatures, compared to the real size of the elliptic section of the airship in the highest curvature zone **C**. A 5° angle of curvature array, corresponding to a small curvature conformal array, and a 20° angle of curvature array corresponding to a high curvature conformal array are modeled and compared.

The results are depicted in Fig. 3.4. The S-parameters configuration are defined in Fig. 3.4(b). Fig. 3.4(c) gives the results at low curvature and Fig. 3.4(d) at high curvature. First, it can be noticed that for both cases, the coupling values fall under -10 dB to -20 dB. Differences occur between close elements coupling S_{2-1} and further element coupling S_{8-1} at low frequency rather than high frequencies. The S_{2-1} values decrease at high frequency because the current is localized in the center of the spiral. Comparison between the 20° angle of curvature and the 5° angle of curvature arrays highlights the effect of curvature on coupling. The changes appear for the S_{6-1} and S_{8-1} values that correspond to the elements located at opposite sides of the array. Higher curvature means also a shorter distance between elements and the coupling increases. However, it is also interesting to notice that the S_{2-1} value remains the same for both curvature.

For a high curvature array, modeling results confirmed the results shown in the Section 3.1.1. Values of coupling have been found under -10 dB and the highest values concern elements close to each other.

3.1.3 Influence of the curvature

It has been shown previously that the most influent type of coupling was the coupling between neighboring elements. In the case of an array with an ellipse shape, the curvature is a particularly important parameter since it varies along the ellipse. In order to study the curvature influence, two neighboring spiral antennas are considered and various configurations at different angles of curvature curvature are modeled. Spirals have two faces, one radiates RHCP field, the second radiates LHCP field. Thus, the first case where two identical antennas radiate the same RHC polarized far field at

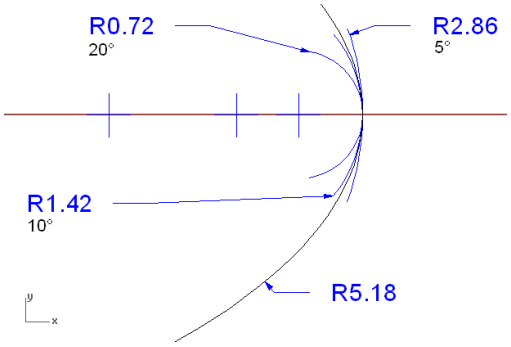

(a) Comparison of the various curvature 8-element array geometries with the real size ellipse of the airship (high radius of curvature R=5.18). Radius of curvature are also indicated for the various array shapes.

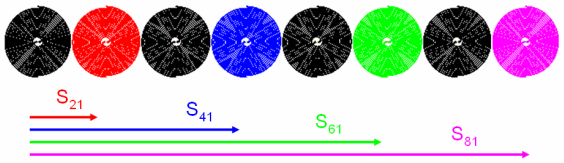

(b) coupling between spiral array.

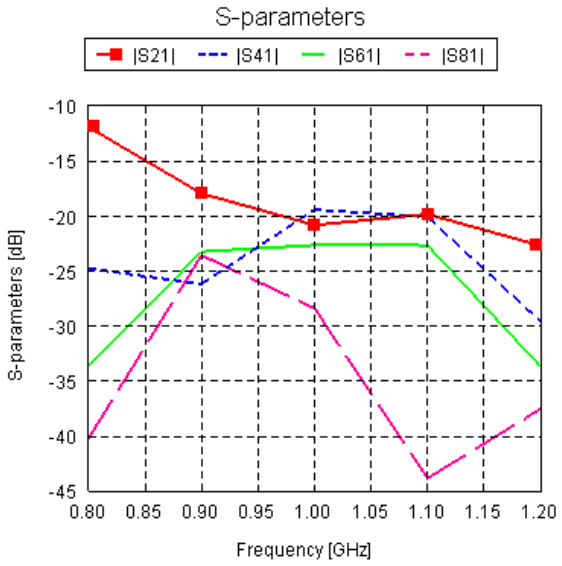

(c) 5° angle of curvature

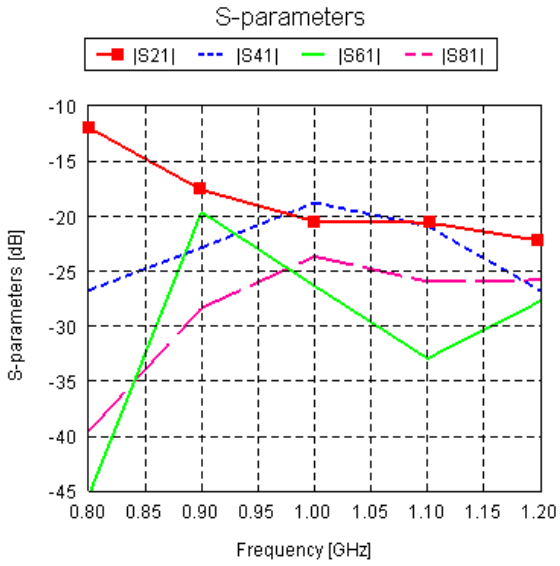

(d) 20° angle of curvature

Figure 3.4: *8-antenna array at* 5° *and* 20° *angle of curvature.* $|S_{ij}|$ *coefficients according to the frequency obtained by FEKO.*

broadside direction (co-polarization antennas) is shown in Fig. 3.5(a). Fig. 3.5(b) shows the other case, where the second antenna radiates a LHC polarization (cross-polarization antennas). The comparison of the values between the two configurations shows that the coupling is clearly stronger

for co-polarization than for the cross-polarization one. Then, it can be noticed that the coupling increases slightly with curvature due to the fact that antennas are closer. But, the curvature has a a very low effect on coupling and the S_{12} coefficient is lower than -15 dB at any case.

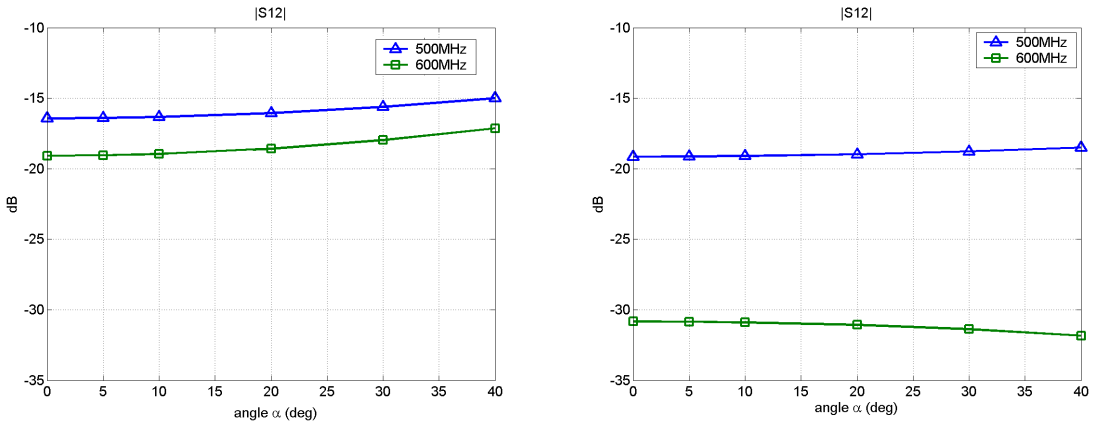

(a) S_{12} coefficient between two antennas with the same orientation RHC-RHC (co-polarization).

(b) S_{12} coefficient between two antennas with opposite orientation RHC-LHC (cross-polarization).

Figure 3.5: *Influence of the curvature on coupling values.*

Consequently, the results of various modeling configuration have stressed that considering spiral antennas, coupling values are not so high. Indeed, except at low frequencies, the currents are located in the center part of the spiral and the coupling between close elements is reduced. Furthermore, the main radiation of the spiral antenna is perpendicular to its plane minimizing coupling between neighboring elements. Finally, the curvature parameter has been studied in various cases and it has been highlighted that curvature has a really poor influence on coupling.

3.2 Measurements of coupling

Coupling results and conclusions coming from the modeling tool have to be validated by measurements. Measurements of single antennas have already been reported in the first chapter. It has been shown that the measured radiation characteristics of the spiral antenna prototype nearly matched the gain and pattern obtained by modeling. However, disturbances have been noticed in the radiation pattern shape of the measured single antennas. Moreover, it has been supposed that the insertion of a transformer component introduces reflections and lower the antenna radiation efficiency. Practical considerations have been also observed from the single antenna measurements. The interferences between the feeding cable and the antenna can be reduced if the cable is perpendicular to the antenna plane. The array platform prototype will be designed following the

knowledge developed during the single antenna measurements. Then, the conformal antenna array measurements results will be compared with those of modeling.

3.2.1 Design of the array prototype

A platform is required to hold the single antennas and to form the curvature of the conformal array. The present purpose is to fit to the configuration of the arrays modeled in free space with FEKO. In the case of a curved array, the array has various local plane, and keeping the cable perpendicular to the array plane is no longer valid. The use of absorbers reducing the interactions between cables and antennas can neither be considered. Indeed, absorber presence at the array back would change the coupling and also forbid the back radiation of the array. Consequently, because it is not possible to avoid the interaction of cables, it has been chosen to let them lie locally perpendicular to the array curvature.

A CAD tool is used to design the platform. Two arrays of different curvatures will be measured and the two corresponding platform designs achieved can be seen in Fig. 3.6. The position and orientation of the array elements must be respected with good accuracy since it strongly influences the pattern shape. Thus, holes are drilled in the platform with defined angles as it can be seen in Fig. 3.7(c). Drilling angles and dimensions are drawn in Fig. 3.6(b) and Fig. 3.6(b). Theses holes are used to guide the cables that are feeding the spirals at their centers. Hence, the perpendicular orientation of cables is respected as well as the position accuracy. Furthermore, the edges of the platforms have been shaped to provide an accurate array curvature. The example of the 20° angle of curvature platform, shaped in a high density Styrofoam material, can be seen in Fig. 3.7. This material provides good mechanical robustness to allow repetitive measurements.

Another issue is that the feeding of the array must achieve equal excitations from one source coming from the VNA. So, power splitters and cables are gathered to constitute the feeding circuit shown in Fig. 3.7(d). The technical characteristics of the chosen components are shown in appendix. The power splitters and cables have been chosen to fit to the modeled uniformly excited array. The phase unbalance and the magnitude unbalance must be kept as low as possible. The magnitude unbalance is the worst-case variation in insertion loss between the 8 ports of the feeding circuit. The phase unbalance is the offset from the desired carrier phase relative to the actual phase shift in any of the possible phase states. Furthermore, to limit the coupling between the 8 ports of the feeding circuits, power splitter with a good isolation must be chosen. Unfortunately, the power splitters and cables introduce small phase unbalance and small magnitude unbalance. Nevertheless, these coefficients can be easily estimated by measuring the S_{i1} coefficients of the 1-8 ports feeding circuit. A VNA is connected to the input port-1 and to the port-i (with i the number of the feeding output port). All the other output port are matched to a 50Ω load and the S_{21} is measured for each port. Table 3.8 shows the measured magnitude variations and phase variations calculated as the

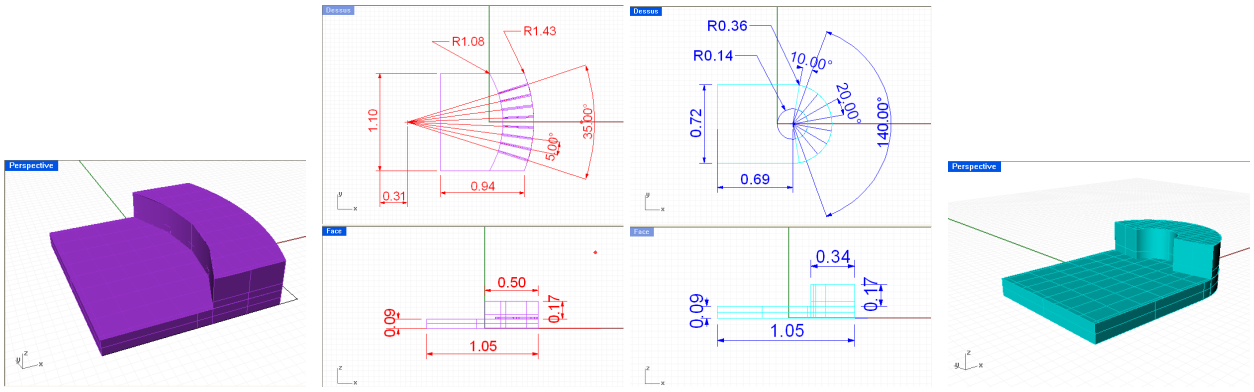

(a) 3D view of the 5° angle of curvature platform

(b) Dimensions (m) of the 5° angle of curvature platform

(c) Dimensions (m) of the 20° angle of curvature platform

(d) 3D view of the 20° angle of curvature platform

Figure 3.6: *Design of Styrofoam platform for conformal array measurements.*

difference between the maximum value and the minimum value at a given frequency. The measured characteristics of the feeding circuit can be used for any curvature since they only depend on the circuit components. The feeding circuit components are located as far as possible from the array to reduce the possible interferences. However, it must be noticed that the phase and magnitude unbalance introduced by the transformer component cannot be estimated. Indeed this component is connected to the spiral printed circuit.

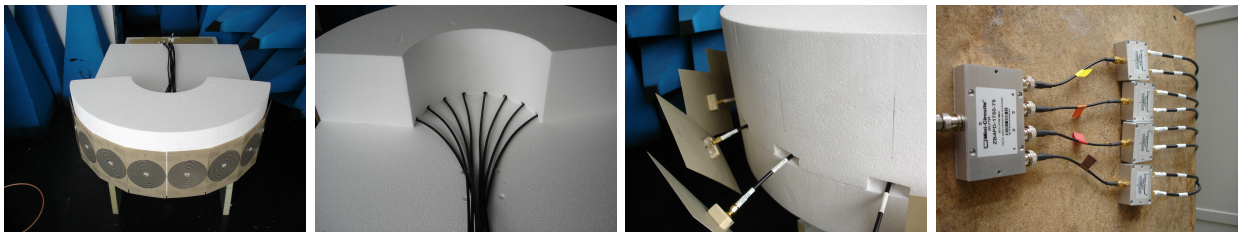

(a) Face view.

(b) Back view.

(c) Details.

(d) Array feeding network composed by power splitters.

Figure 3.7: *Pictures of the* 20° *angle of curvature Styrofoam platform*

	800 MHz	900 MHz	1000 MHz	1100 MHz	1200 MHz
Magnitude variation (dB)	0.06	0.07	0.08	0.16	0.15
Phase variation (degree)	7.2	8.1	9.6	9.8	10.0

Figure 3.8: *Phase and magnitude variations (Max - Min) of the 8-port feeding circuit.*

3.2.2 Coupling Measurements results

Coupling is now estimated by measurements. The 5° of curvature array is considered and S_{ij} are measured to obtain the 8x8 matrix of coupling. A 2-ports VNA is used and thus only two cables are simultaneously connected to the array. The 6 other antennas are matched to 50 Ω loads. The measurement is done successively to get all the components of the coupling matrix. Thus, the 64 S_{ij} values can be obtained after 32 different configurations. To reduce the measurement time, we consider the symmetry of the array to have $S_{ij} = S_{((N+1)-i)((N+1)-j)}$ i.e. $S_{12} = S_{87}$. Furthermore, we consider also the reciprocity of the antenna coupling $S_{ij} = S_{ji}$. Thus, only 16 configurations are required for the coupling matrix measurement. The results are presented in Fig. 3.9. Two axis of symmetry along the two diagonals of the matrix can be observed, due to the two previous assumptions that concern the reciprocity and the array symmetry. From Fig. 3.9 it can be seen that the coupling decreases with the distance. However, the S_{18} coefficient is higher than S_{17}, probably due to the curvature of the array. The evolution with frequency is less clear. Higher values can be clearly noticed at 900 MHz. Nevertheless, when looking at the S_{12} versus the continuous frequency measured by the VNA (see Fig. 3.10), it can be observed that resonances occur. For example, at 1000 MHz, coupling between element 1 and element 4 decreases suddenly. Thus no specific behavior of coupling values versus frequency can be clearly deduced. Further investigations on coupling at specific frequencies would have to be performed to clarify this effect.

The results of the measured coupling values can also be compared with the coupling values obtained by modeling. Fig. 3.11 shows the comparison between modeling and measurement results of the S-parameters (dB) versus the frequency. An 8-elements conformal array with 5° of curvature is still considered. It can be observed that the range of values from -25 dB to -40 dB are similar for the S_{14}, S_{16} and the S_{18} values. However, the measured S_{12} values differ from the modeling results. The measurements exhibit a S_{12} lower than the modeled one, especially at low frequency. It can be assumed that back radiations of the spiral induce currents on the cable and that this effect reduces the coupling between close elements. It can also be noticed that the S_{18} is a bit higher than the S_{16} due to the curvature of the array. This effect, related to the array curvature, is confirmed by both measurements and modeling.

The case of 20° angle of curvature should also be measured and analyzed, but because of the lack

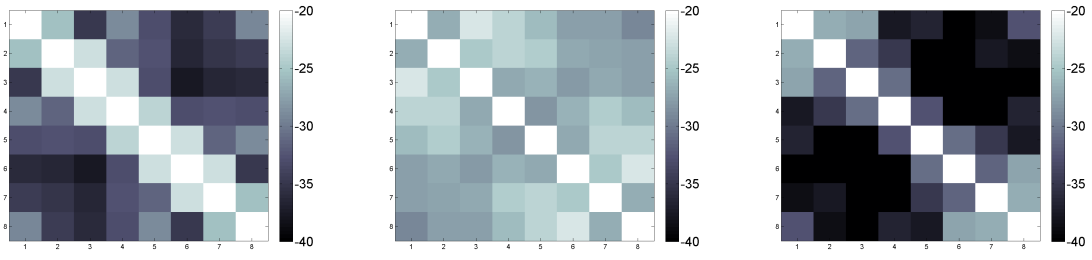

(a) 800 MHz (b) 900 MHz (c) 1000 MHz

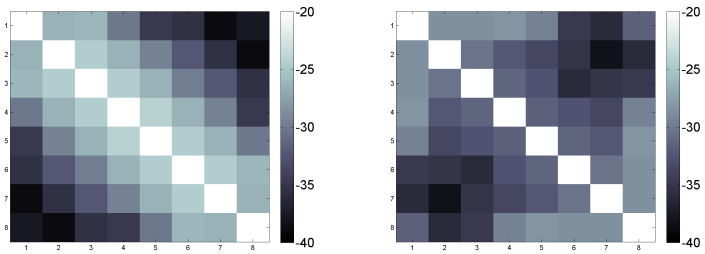

(d) 1100 MHz (e) 1200 MHz

Figure 3.9: *Measured coupling matrix of the 8-elements array with* 5° *of curvature.*

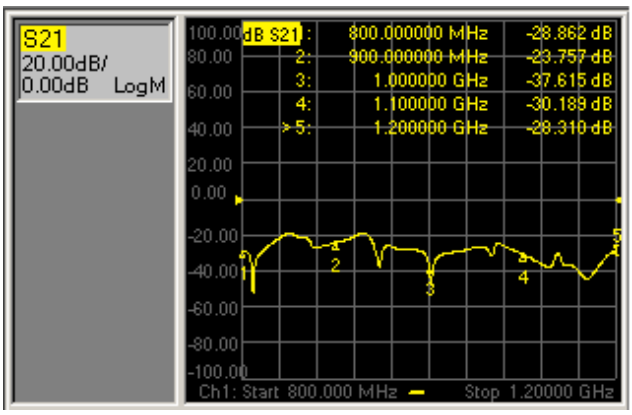

Figure 3.10: *S_{14} coupling values (dB) according to the frequency, measured by the vector network analyzer (VNA)*

of time, only the 5° of curvature array as been tested. However, the results of the measured coupling have demonstrated that cables interact with the array as predicted. The exact cable influence has not been investigated since no contradictions have been found and that we don't want to develop a

model which includes that kind of feeding because of time consuming. The measurements confirmed the low values of coupling evaluated by simulation. Resonances have been noticed possibly due to both the array resonances and spiral own resonances linked to the current distribution on its arms.

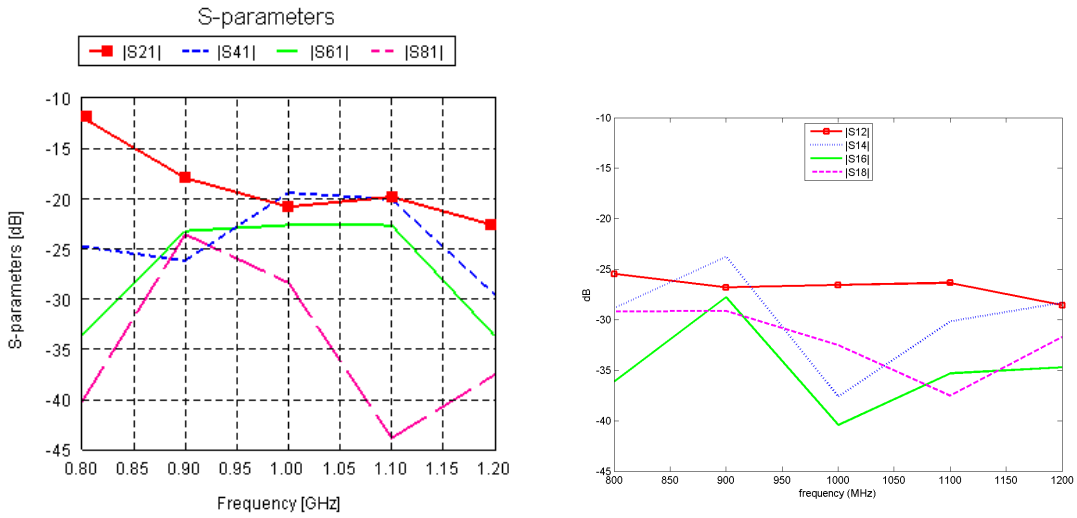

(a) Modeling. Frequency in GHz

(b) Measurements. Frequency in MHz

Figure 3.11: *S-parameters (dB) according to frequency. Comparison between measurements and modeling results. An 8-element conformal array with 5° of curvature is considered in both cases.*

3.3 Computation method for conformal array

Since the computation of the full conformal array radiation characteristic is not possible using an exact method because of the too long computation time, an approximated method must be developed. It has been found in section 3.1, that the highest coupling values are under -10 dB to -35 dB. If the coupling between the elements of the array is low, we can assume that the radiated far field of the conformal array is the sum of the radiated far field of each antenna element. This assumption is usually done to compute the array factor of a classical planar array [66]. So, this approach is expected to significantly reduce the computation time, since it will be necessary to model only one antenna element with an exact method to obtain its radiation pattern.

3.3.1 Conformal array radiation pattern

Problem description

A general conformal array of N elements positioned on an arbitrary shaped surface is considered. We assume that the host platform do not interact with the array. The array is described in the main coordinate system $(\mathbf{x}, \mathbf{y}, \mathbf{z})$. Each element m of the array is located on the surface of the host platform at spherical coordinates $(\rho_m, \theta_m^{pos}, \varphi_m^{pos})$. The coordinates $(\rho_m, \theta_m^{pos}, \varphi_m^{pos})$, standing for the element position, must not be confused with the spherical coordinates (θ, φ) which denote the radiation directions of the array radiation pattern. Fig. 3.12 illustrates an example of a 2-element array conformed to an arbitrary shaped surface. The array is represented in the azimuthal plane $(\mathbf{x}, \mathbf{y})$ at $\theta = 90°$. So, each element is located at position $(\rho_m, \theta_m^{pos}, \varphi_m^{pos})$ given in the array main coordinate system $(\mathbf{x}, \mathbf{y}, \mathbf{z})$. But its element radiation pattern is given in its local coordinate system $(\mathbf{x'}_m, \mathbf{y'}_m, \mathbf{z'}_m)$.

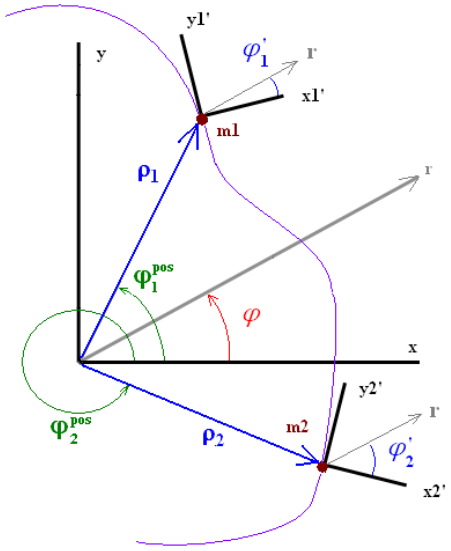

Figure 3.12: *General case of a conformal array configuration. Illustration with a two elements (m_1 and m_2) array , conformed to an arbitrary shaped surface. 2D view of the azimuthal plane $(\mathbf{x}, \mathbf{y})$ at $\theta = 90°$. $\boldsymbol{r}$ is the direction of the radiated field. Main coordinate system $(\mathbf{x}, \mathbf{y}, \mathbf{z})$. local coordinate sytem $(\mathbf{x'}_m, \mathbf{y'}_m, \mathbf{z'}_m)$*

The array total radiated field $\mathbf{E}^{tot}(\theta, \varphi)$, given in Eq. 3.1, is expressed in the main coordinate system $(\mathbf{x}, \mathbf{y}, \mathbf{z})$. $\mathbf{E}^{tot}(\theta, \varphi)$ is the vectorial sum of the elements $\mathbf{E}_m(\theta, \varphi)$, rotated to take into account the orientation of each element. As in any classical array, the relative phase of each element depends on the element position, referenced to the origin of the main coordinate system. The relative phase shift, introduced for a direction $\mathbf{r}$, for the element m, is equal to $\Phi_m = k\mathbf{r}.\rho_m$, with k the wave

number, $\mathbf{r}$ the steering vector at direction (θ, φ) and ρ_m the position vector of element m with the phase reference at the origin of the main coordinate system.

$$\mathbf{E}^{tot}(\theta, \varphi) = \sum_{m=1}^{N} e^{j\Phi_m} \mathbf{E}_m(\theta, \varphi) \tag{3.1}$$

In the case of a planar array, all the elements have the same orientation and the same local coordinate systems. Nevertheless, in the case of a conformal array, the elements have not the same orientation and thus, local coordinate systems $(\mathbf{x'}_m, \mathbf{y'}_m, \mathbf{z'}_m)$ are considered. The element radiation patterns can be summed if all are given in the same main coordinate system $(\mathbf{x}, \mathbf{y}, \mathbf{z})$.

Method description

$\mathbf{E}_m(\theta, \varphi)$ is the desired expression of the rotated pattern expressed in the main coordinate system, required in Eq 3.1.

The rotation depends on the element orientation $\mathbf{n}$, that can be determined from the array shape. A general rotation $\mathbf{R}$ can be written in terms of successive rotation matrices $\mathbf{R}_z, \mathbf{R}_\xi, \mathbf{R}_{z'}$ (Eq. 3.2), with the three Euler rotation angles γ, β, ψ (Fig. 3.13). The rotation angles γ, β, ψ can be derived from the element orientation described in the modeling tool and from the element orientation in the array. Since each element has its own orientation $\mathbf{n}_m$, the rotation matrix must be written as $\mathbf{R}_m$.

$$\mathbf{R}_m = \mathbf{R}_{z'}(\psi_m)\mathbf{R}_\xi(\beta_m)\mathbf{R}_z(\gamma_m) \tag{3.2}$$

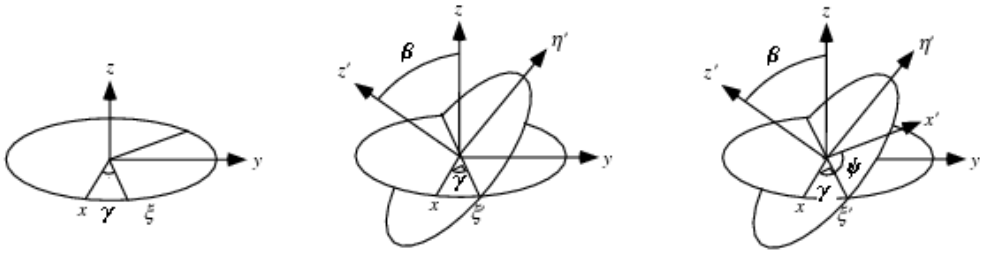

Figure 3.13: *Rotation Euler angles γ, β, ψ used in the general rotation matrix.*

Fig. 3.14 gives the flow diagram to obtain $\mathbf{E}_m(\theta, \varphi)$ from the element radiation characteristic $\mathbf{E}'(\theta', \varphi')$ computed by FEKO. It must be noticed that the discrete values (θ, φ) can be chosen arbitrarily. The directions angles (θ'', φ'') are defined as the angles, given in the local coordinate system, which follow the same discrete distribution as the desired angles (θ, φ), but before rotation.

Three successive steps are required:

1. Get the intermediates angles (θ'', φ'') corresponding to the desired (θ, φ);
2. Obtain the corresponding values of $\mathbf{E}''_m$ in the local coordinate system;
3. Rotate the pattern to obtain the desired $\mathbf{E}_m$.

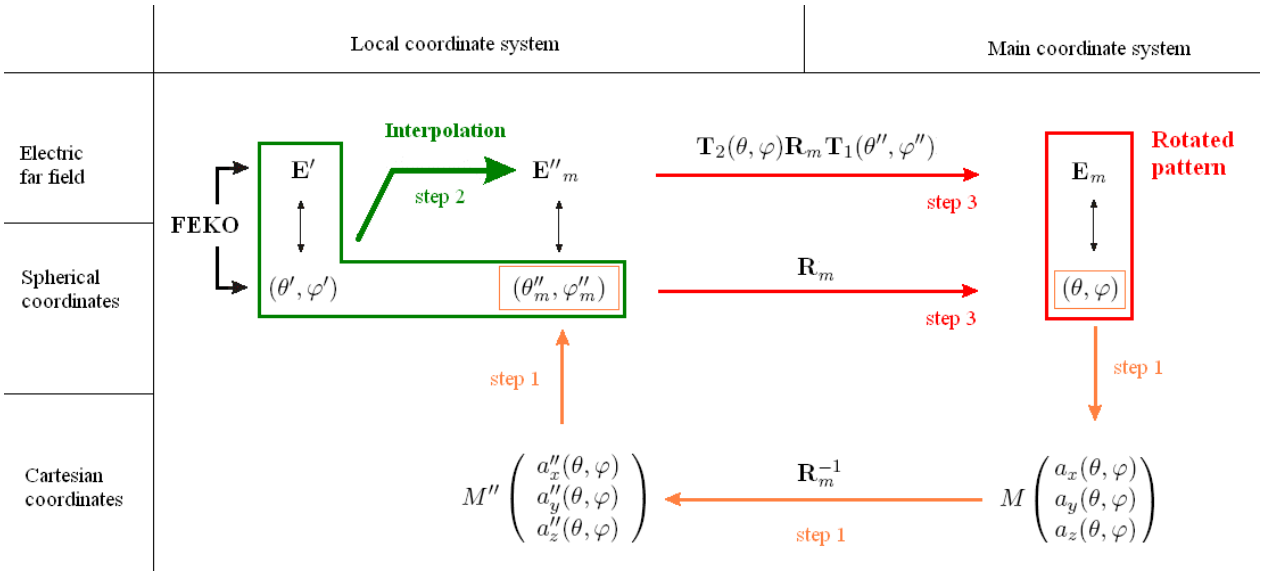

Figure 3.14: *Flow diagram to obtain* $\mathbf{E}_m$ *in the array main coordinate system from the* $\mathbf{E}'$ *given by FEKO.*

The first step, described in Fig. 3.14, has to be done before the rotation of the pattern. Indeed, the desired angle distribution (θ, φ) cannot be obtained directly from the initial angle distribution (θ', φ') of FEKO. The discrete angles do not take the same values before and after the rotation (see Fig. 3.15). The solution is to calculate intermediate direction angles $(\theta''_m, \varphi''_m)$ in the local coordinate system which will give the direction angles (θ_m, φ_m) in the main coordinate system after rotation. Hence, a rotation $\mathbf{R}_m^{-1}$, coming from the rotation $\mathbf{R}_m$ is used to rotate the element radiation pattern of the main coordinate system to the local one. To use properly the rotation $\mathbf{R}_m^{-1}$ in a cartesian coordinate system, the point M_m is introduced. It has spherical coordinates $(1, \theta, \varphi)$. The corresponding cartesian coordinates (a_x, a_y, a_z) can be obtained by Eq. 3.3 and are required to calculate the spherical direction angles after rotation.

$$M \begin{pmatrix} a_x(\theta,\varphi) = & \sin\theta\cos\varphi \\ a_y(\theta,\varphi) = & \sin\theta\sin\varphi \\ a_z(\theta,\varphi) = & \cos\theta \end{pmatrix} \tag{3.3}$$

Then, cartesian coordinates (a''_x, a''_y, a''_z) of point M in the local coordinate system, after rotation $\mathbf{R}_m^{-1}$ are given by Eq. 3.4. Finally, new spherical coordinates $(\theta''_m, \varphi''_m)$ representing the direction angles in the local coordinate system can be obtained from Eq. 3.5 and Eq. 3.6.

$$M''\left(\begin{pmatrix} a''_x(\theta,\varphi) \\ a''_y(\theta,\varphi) \\ a''_z(\theta,\varphi) \end{pmatrix}\right) = \mathbf{R}_m^{-1}\left(\begin{pmatrix} a_x(\theta,\varphi) \\ a_y(\theta,\varphi) \\ a_z(\theta,\varphi) \end{pmatrix}\right) \tag{3.4}$$

$$\theta'' = Arccos\left(\frac{\mathbf{a''}_z(\theta,\varphi)}{\sqrt{\mathbf{a''}^2_x(\theta,\varphi) + \mathbf{a''}^2_y(\theta,\varphi) + \mathbf{a''}^2_z(\theta,\varphi)}}\right) \tag{3.5}$$

$$\varphi'' = Arccos\left(\frac{\mathbf{a''}_x(\theta,\varphi)}{\sqrt{\mathbf{a''}^2_x(\theta,\varphi) + \mathbf{a''}^2_y(\theta,\varphi)}}\right) \tag{3.6}$$

The issue is that no electric field have been calculated for the angles (θ', φ'). So, an interpolation technique is required.

The second step, described in Fig.3.14, is required to find the $\mathbf{E''}_m$ associated to the previously calculated $(\theta''_m, \varphi''_m)$. An interpolation of the $\mathbf{E'}$ values according to the corresponding (θ', φ') and the desired $(\theta''_m, \varphi''_m)$ is used. The interpolation is done in the local coordinate system before the rotation of the local radiation pattern. Once the $\mathbf{E''}_m$ radiated field values have been obtained, the discrete values problem is solved and the rotation of the radiation pattern $\mathbf{E''}_m$ is now possible.

The third and final step, shown in Fig.3.14, is the rotation of the local coordinate radiation pattern with a rotation matrix $\mathbf{R}_m$. Hence the desired radiated field $\mathbf{E}(\theta,\varphi)$ in the main coordinate system can be obtained. A rotation $\mathbf{R}_m$ with the same rotation angles $\gamma_m, \beta_m, \psi_m$ is applied to $\mathbf{E''}_m$. The angles (θ'', φ'') calculated in step 2 using $\mathbf{R}_{m^{-1}}$ will obviously correspond to the desired angles (θ, φ).

The rotation of $\mathbf{E''}_m$ takes into account the polarization characteristic of the electric field. furthermore, the orientation of the electric field vector $\mathbf{E''}_m$ is defined in the polarization basis $(\mathbf{e}''_r, \mathbf{e}''_\theta, \mathbf{e}''_\varphi)$ of the local coordinate system (see Fig. 3.16(a))

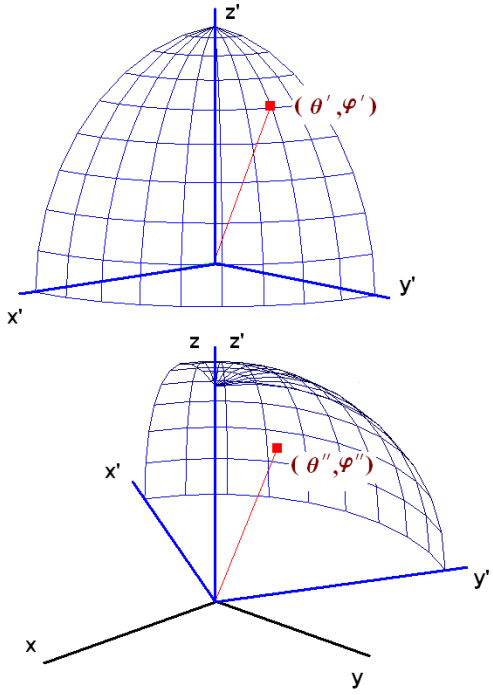

Figure 3.15: *View of the distribution of the discrete direction angles (θ', φ') given by FEKO and the distribution of the discrete direction angles $(\theta''_m, \varphi''_m)$ obtained after a rotation $\mathbf{R}_m^{-1}$. These two coordinate distributions do not match necessarily and an interpolation is required.*

To rotate properly the $\mathbf{E}''_m$ values in the main coordinate system, the rotation matrix has to be used in the local cartesian coordinate system $(\mathbf{x}', \mathbf{y}', \mathbf{z}')$. Thus, Eq. 3.7 is applied and gives the $\mathbf{E}_m$ values in the desired polarization basis $(\mathbf{e}_r, \mathbf{e}_\theta, \mathbf{e}_\varphi)$ of the main coordinate system.

It can be noticed that a similar approach had been done in [67]. However, it is not including the radiation pattern of the single element and planar arrays are considered located on a conformal surface. Furthermore, the discrete angles issue that appears in practice has not be solved nor discussed.

$$\mathbf{E}_m(\theta, \varphi) = \mathbf{T}_2(\theta, \varphi)\mathbf{R}_m\mathbf{T}_1(\theta'', \varphi'')\mathbf{E}''(\theta'', \varphi'') \tag{3.7}$$

The transformation matrix $\mathbf{T}_1$ (given in Eq. 3.8) is first applied to $\mathbf{E}''_m$ and gives the cartesian coordinates $(\mathbf{E}''_x, \mathbf{E}''_y, \mathbf{E}''_z)$ in the local coordinate system $(\mathbf{x}_m, \mathbf{y}_m, \mathbf{z}_m)$.

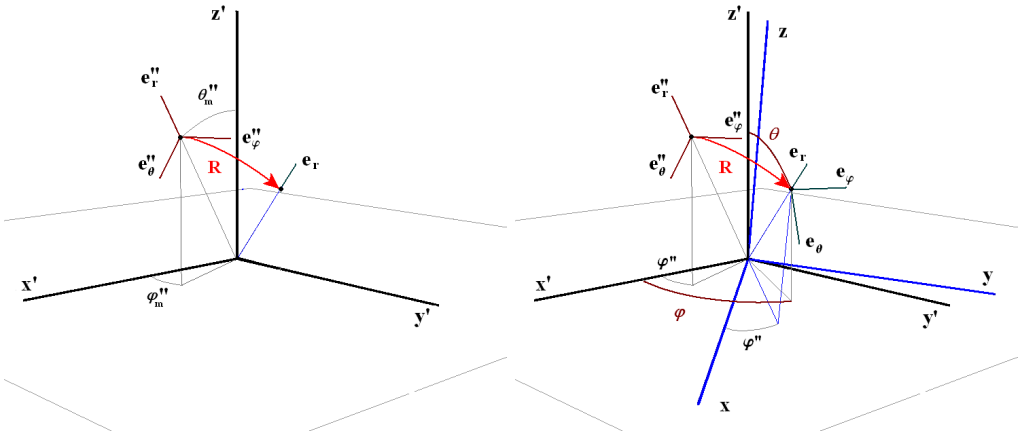

(a) Antenna local coordinate system $(\mathbf{x'}_m, \mathbf{y'}_m, \mathbf{z'}_m)$ and its polarization basis $(\mathbf{e}''_r, \mathbf{e}''_\theta, \mathbf{e}''_\varphi)$

(b) Array main coordinate system $(\mathbf{x}_m, \mathbf{y}_m, \mathbf{z}_m)$ and its polarization basis $(\mathbf{e}_r, \mathbf{e}_\theta, \mathbf{e}_\varphi)$

Figure 3.16: *Coordinate systems and polarization basis systems*

$$\mathbf{T}_1 = \begin{pmatrix} \sin\theta''\cos\varphi'' & \cos\theta''\cos\varphi'' & -\sin\varphi'' \\ \sin\theta''\sin\varphi'' & \cos\theta''\sin\varphi'' & \cos\varphi'' \\ \cos\theta'' & -\sin\theta'' & 0 \end{pmatrix} \tag{3.8}$$

Then a rotation matrix $\mathbf{R}_m$ is used to rotate each element m pattern. After the rotation, the radiated field $\mathbf{E}_m$ has to be given in the polarization basis $(\mathbf{e}_r, \mathbf{e}_\theta, \mathbf{e}_\varphi)$ of the main coordinate system (see Fig. 3.16(b)). Thus, matrix $\mathbf{T}_2$ given in Eq. 3.9 is used. $\mathbf{T}_2$ is a transformation matrix from cartesian to spherical, it requires the direction angle of the main coordinate system (θ, φ). It must be noticed that $\mathbf{T}_2$ is not equal to $\mathbf{T}_1^{-1}$ since the angles (θ, φ) of the main coordinate system and (θ'', φ'') of the local coordinate system are not the same.

$$\mathbf{T}_2 = \begin{pmatrix} \sin\theta\cos\varphi & \sin\theta\sin\varphi & \cos\theta \\ \cos\theta\cos\varphi & \cos\theta\sin\varphi & -\sin\theta \\ -\sin\varphi & \cos\varphi & 0 \end{pmatrix} \tag{3.9}$$

Thus, from a radiation pattern computed in its own coordinate system, it is possible to rotate the pattern and express it in a new coordinate system. The issue of discrete angles can be solved using interpolation in an intermediate step. The rotation keeps the polarization and the complex nature of the radiated field. It can be used to obtain the radiated field of variously orientated elements

of a conformal array. Nevertheless, this rotation method can be also very useful in polarization measurements of devices, when the base of polarization does not match with the orientation of the chosen antenna, for practical reasons.

Polarization

Since the considered application must distinguish the polarization, the total far field $\mathbf{E}_{tot}$ must be decomposed into two components $(\mathbf{E}_{rhcp}, \mathbf{E}_{lhcp})$ in a circular polarization basis. The choice of a circular polarization basis is done to fit to the antenna geometry and polarization characteristics. The modeling tool FEKO, used to obtain the element radiated field $\mathbf{E}'(\theta', \varphi')$ in the local coordinate system $(\mathbf{x'}_m, \mathbf{y'}_m, \mathbf{z'}_m)$, gives $\mathbf{E}'$ in a $(\mathbf{E'}_\theta, \mathbf{E'}_\varphi)$ linear basis, i.e $(\mathbf{E'}_{vertical}, \mathbf{E'}_{horizontal})$. But, it is possible to switch from one polarization basis to the other using the expressions given by Eq. 3.10 and Eq. 3.11. Thus, each component of the polarized far field $\mathbf{E}'(\theta', \varphi')$ could be expressed in both circular $(\mathbf{E}_{rhcp}, \mathbf{E}_{lhcp})$, or linear $(\mathbf{E'}_{vertical}, \mathbf{E'}_{horizontal})$ polarization basis. The above method has to be applied for each of the polarization component of the far field.

$$\mathbf{E}_{rhcp} = \frac{1}{\sqrt{2}}(\mathbf{E}_\theta + j\mathbf{E}_\varphi) \tag{3.10}$$

$$\mathbf{E}_{lhcp} = \frac{1}{\sqrt{2}}(\mathbf{E}_\theta - j\mathbf{E}_\varphi) \tag{3.11}$$

3.3.2 Approximated method validation

In order to validate the approximated method, radiation patterns obtained by the approximated method, by simulation and by measurements are now compared for various frequencies and various angles of curvature. An 8-spiral element array, with spirals radiating RHC polarization outward is still considered. The measurements are performed between 800 MHz and 1200 MHz, with a half-reduced size antenna of 12.5 cm diameter. So, the results are equivalent to those of an antenna of 25 cm diameter measured between 400 MHz and 800 MHz. Measurements have been done in the spherical configuration (Fig. 3.17(a)). The array platform is mounted vertically with the maximum of radiation pointing at $\theta = 0°$ (see Fig. 3.17(b)). Radiation patterns are shown in Fig. 3.18 for the 5°curvature and Fig. 3.19 for the 20°curvature. Only the plane containing the conformal array is depicted.

To obtain the far field radiation pattern, a near field to far field transformation developed at Supelec for the Sesame test facility is used. Indeed, the dimensions of the array platform compared to the measurement setup dimensions are too close. It must be highlighted that the near field measurement is truncated, because the probe can only achieve measures from $\theta = 0°$ to $\theta = 170°$ (see Fig. 3.17(a)). It means that measurements cannot be performed within a solid angle of 10°

radius. Using the near field to far field transformation, the non measured values are forced to zero according to the Supelec code. As a consequence the far field results are degraded especially in this region that corresponds to the LHCP radiation.

To exploit properly the measurement results and to compare with simulation and approximated method results, the radiation pattern of the measured array is rotated using the pattern rotation method developed in the section 3.3.1. Thus, we obtain the rotated radiation pattern corresponding to an array located in the azimuthal plane looking forward the **x** axis. This technique provides the advantage to keep the cables aligned in the perpendicular plane of the antenna array plane, and to express the results in a more convenient coordinate system. So, the non measured region corresponds now to angles φ between 170° and 190°. The outward radiation corresponding to the convex part of the array is at $\varphi = 0°$. The inward radiation corresponding to the concave part of the array is at $\varphi = 180°$. Both RHC and LHC polarized radiation patterns at 800, 1000 and 1200 MHz are shown in Fig. 3.18 and Fig. 3.19. The plots have been normalized to 0 dB.

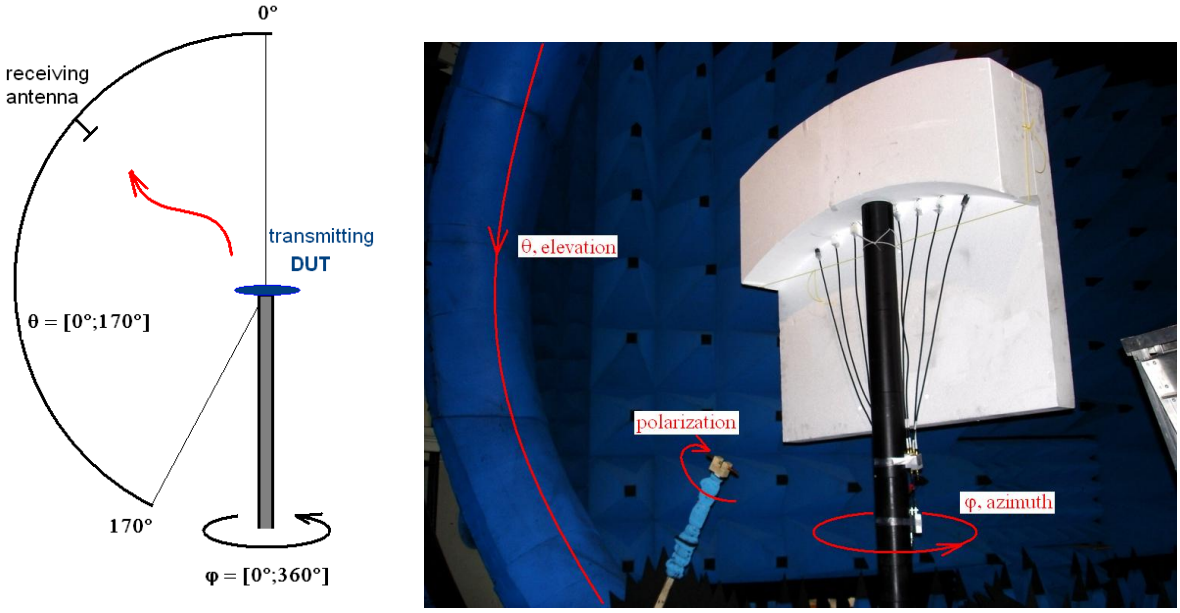

(a) The receiving antenna probe is limited to $\theta \leq 170°$

(b) Configuration of the 5° of curvature platform in the anechoic chamber.

Figure 3.17: *Configuration of the array radiation pattern measurement.*

The measured radiation pattern has not an exact uniform excitation because of the phase and magnitude unbalance at the output of each cable of the feeding circuit. Nevertheless, the S_{12} value at each feeding circuit port has been previously measured. It characterizes the phase and

magnitude unbalance and provides a set of eight complex coefficients. These coefficients are included in the approximated method (*approximated + correction*) and can hence be compared with the measurement results. From the Fig 3.18 and Fig 3.19, it can be seen that these corrections slightly change the shape of the radiation pattern, especially the symmetry. However these changes are really small compared to the differences that can be seen between the three different methods.

The results of the approximated method can be compared with the results of the modeling obtained by the MoM, both array having a uniform excitation. It can be seen that for every cases of curvature and frequency, the approximated method fits quite well to the modeling results. For both polarization, the reconstruction of the main lobe corresponding to the co-polarization (at $\varphi = 0°$ for RHCP and $\varphi = 180°$ for LHCP), is fulfilled for frequencies within the band. Cross-polarization lobe exhibits more important differences between the two methods, especially when the radiation of the isolated element in this direction is particularly low. The main differences occur at φ directions corresponding to directions in the antenna plane and with low values of radiation. The results of the *"approximated method + corrections"* can be compared with the results of the measurements, both array having the same coefficient of excitation.

Furthermore, the spiral antennas are turned to radiate the RHCP to the ceiling and the LHCP to the floor. Cables are located in the concave face of the array i.e. the LHCP radiation face. As a consequence differences can be noticed between the measurement results and the approximated method in the LHCP radiation lobe. This effect is much more visible when the curvature is low and when the lobe is more focused in the non measured region.

At higher frequencies, disturbances can be observed in the measured radiation pattern. This confirms the results previously obtained by individual antenna measurements, where the size of the feeding devices (cable and transformers) becomes more influent on the antenna radiation pattern. The effect of the array conformation is clearly seen when comparing the results of the 5° angle of curvature and the 20° angle of curvature. All antennas have their own orientation and concentrate the field in different directions. So the more the curvature increases, the more the element orientations differ, leading to lower the main beam level. Then, due to the antenna characteristic, the cross-polarization level is better at higher frequencies.

The approximated method, neglecting the coupling, allows to predict the conformal array radiation pattern, for any array shape, any antenna. Furthermore, it includes the vectorial nature of the electric field and allows polarimetric applications. So, for the considered array of eight spiral antennas in the conformal case as in the planar case, it is possible to obtain the shape and the level of the main lobe simply by summing the contributions of each antenna element, taking into account the orientation of each one.

3.4 Conclusion of Chapter 3

In this chapter, the issue of the conformal array radiation pattern computation has been studied. Indeed, a full modeling using FEKO is too time consuming, and a pattern synthesis optimization requires a model to compute the excitation coefficient set.

Therefore, a model has been developed based on the vectorial sum of every array element contribution. In a first step, coupling have been evaluated using reduced array size and simplified spiral antenna model. The S_{12} values computed by FEKO for various curvatures and frequencies have shown that coupling should be lower than -10 dB. Thus, it has been decided to neglect these coupling in the array radiation pattern computation.

An approximated method neglecting coupling has then been developed. It is based on the rotation of the radiation characteristic of the elements. It has been demonstrated how the discrete values of the radiation characteristic computed by FEKO required a re-sampling. Furthermore, the different steps of the rotation method have been carefully described.

A conformal array prototype has been designed and built to validate the results given by the modeling and the approximated method. It has been emphasized that the cable could not be perpendicular to every elements since each antenna has its own plane. Thus, a practical realization of such array is really challenging and emphasizes the necessity of using full coplanar technology or opto-electronic solutions. However, the measured coupling behavior in the array fits to the modeling results and value have been found also less than -10 dB. Nevertheless, some doubts regarding the radiation efficiency of the antenna elements remain because it has not been possible to perform the absolute gain measurement of the array because of the lack of time.

The approximated method has been validated through comparisons with measurements and modelings. It has been verified that the shape of the radiation characteristic was respected at various curvatures and frequencies, for a uniform excitation. It has been found that the variations between the characteristics of the array elements do not affect so much the shape of the radiation pattern. Strong differences have been found in the measurements results for the back lobe of the polarized field, as it was already the case for the single antenna measurement due to the cable presence and the limitation of the measurement facility devices.

So, even if the cables obviously disturb the measurements, it has been found that the measured array characteristics are close to those given by the other method. That means that the results of the approximated method are in good agreement with the practical array array performances. It must be also noticed that the approximated method enables the rotation of a vectorial characteristic and can also be useful to choose the coordinate system for measurements when the feeding cable implies a specific orientation of the antenna under test.

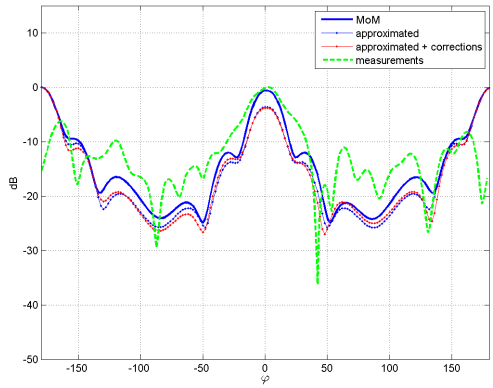

(a) 5° angle of curvature, 800 MHz, LHCP

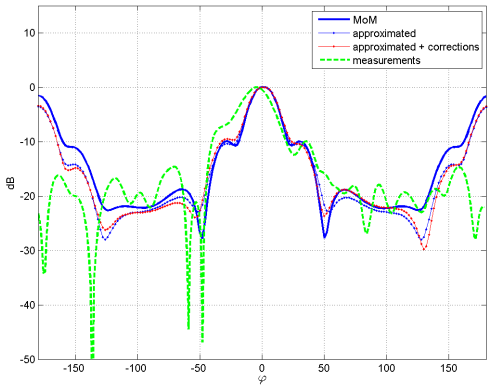

(b) 5° angle of curvature, 800 MHz, RHCP

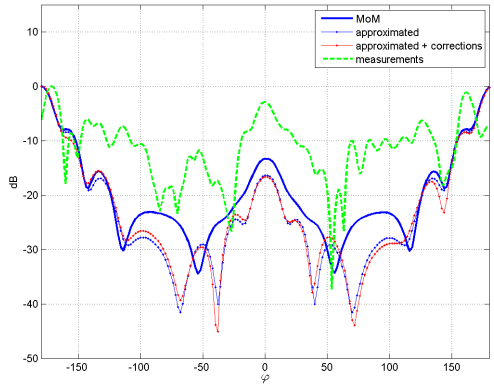

(c) 5° angle of curvature, 1000 MHz, LHCP

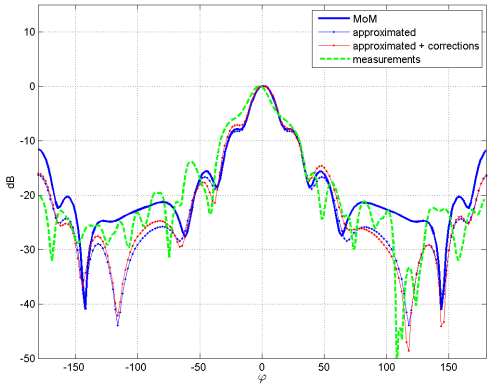

(d) 5° angle of curvature, 1000 MHz, RHCP

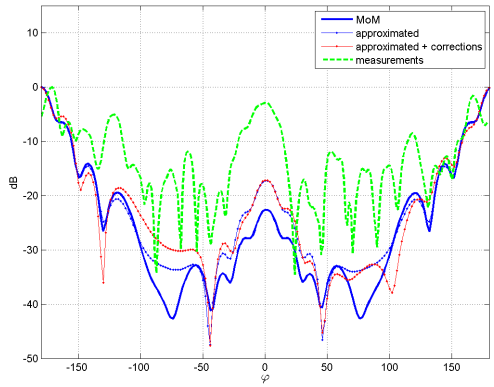

(e) 5° angle of curvature, 1200 MHz, LHCP

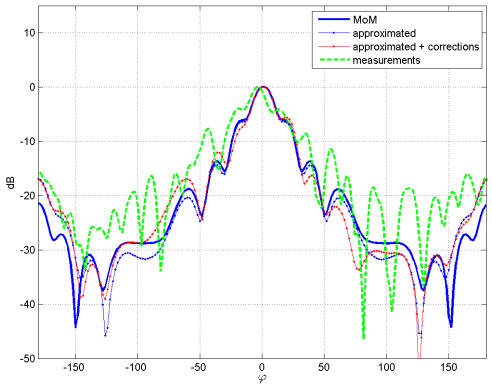

(f) 5° angle of curvature, 1200 MHz, RHCP

Figure 3.18: *Result comparisons at* 5° *angle of curvature. The curve "approximated" gives the radiation pattern of an uniformly excited array computed with the approximated method. The curve "approximated + corrections" gives the radiation pattern of an array excited using the measured coefficients of the feeding circuit, integrated in the approximated method.*

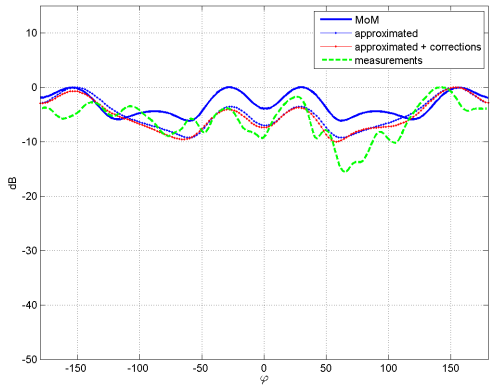

(a) 20° angle of curvature, 800 MHz, LHCP

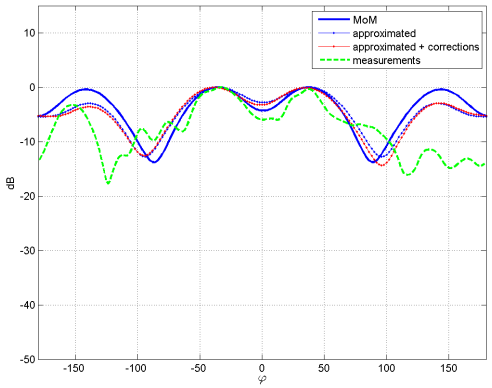

(b) 20° angle of curvature, 800 MHz, RHCP

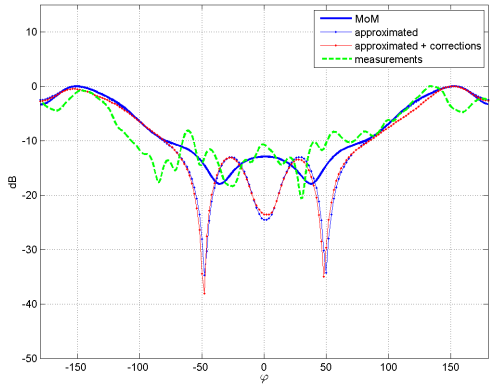

(c) 20° angle of curvature, 1000 MHz, LHCP

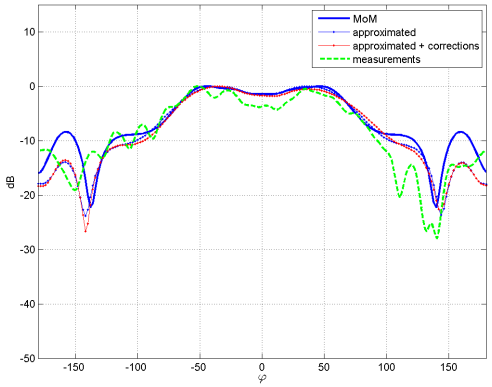

(d) 20° angle of curvature, 1000 MHz, RHCP

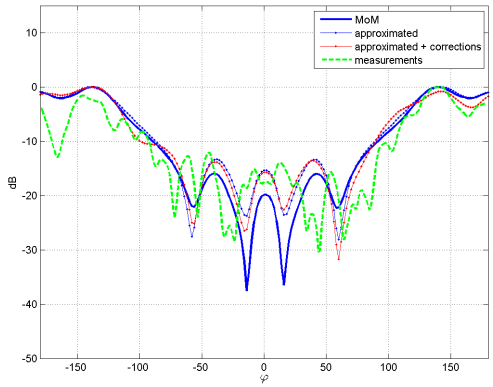

(e) 20° angle of curvature, 1200 MHz, LHCP

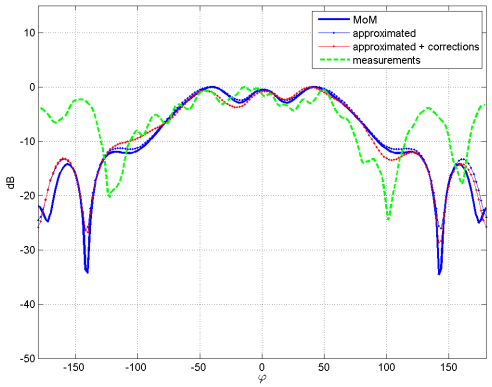

(f) 20° angle of curvature, 1200 MHz, RHCP

Figure 3.19: *Result comparisons at* 20° *angle of curvature. The curve "approximated" gives the radiation pattern of an uniformly excited array computed with the approximated method. The curve "approximated + corrections" gives the radiation pattern of an array excited using the measured coefficients of the feeding circuit, integrated in the approximated method.*

Chapter 4

Dual Polarized Performances of the Phased Conformal Array

The conformal array is mounted on an airship for radar applications and it will be used as a receiving array for digital beamforming. However, to facilitate the study, a transmitting array will be considered in this chapter. Thanks to the reciprocal behavior of the antenna array, the beamforming capability can thus be demonstrated.

Large array allows good radar angular resolution, corresponding to a radiation pattern with a narrow main beam. The feasibility of synthesizing radiation patterns with narrow main beam must be demonstrated at various scan angles. Furthermore, for polarimetric radar applications, the level of cross-polarization has to be kept low enough whatever the scan angle is.

The shape, the location and the technology of the array is given in Chapter 2. A 134-element array is conformed to the front part of the airship and has consequently a half ellipse shape. The electromagnetic behavior and the radiation pattern computation method of a such array has been developed and described in Chapter 3.

This chapter discusses the achievable performances of the array according to the desired patterns. Indeed, in the case of an airship used as a host platform, the ground plane which traditionally redirects the field outward cannot be used. As a consequence, the directivity is lower and a part of the radiated field goes inward in wrong directions leading to a waste of energy. The main purpose is to find the complex coefficients that fulfill the narrow beam and the low cross polarization pattern requirements.

The conformal non planar shape of the array is taken into account to optimize the range of possible scanning angles. A scanning over 360° will be considered in the optimization procedure. The cross-polarization behavior will be particularly investigated to allow radar polarimetric applications.

4.1 Array configuration analysis

As the array is conformed to an airship, used as a host platform, some unconventional aspects of the host platform have to be pointed out. Unlike the numerous other platforms, airship body has poor interaction with the antenna array because it is filled with helium ($\epsilon_r \approx 1$) and its skin is really thin. As a consequence, the possibility of radiating in any direction of space can be considered. For instance, this is not the case for antenna arrays on a metallic ground plane where only a half space of radiation is considered.

First, the polarization features have to be carefully described for both the conformal array and the spiral antenna. The conformation of the array introduces differences between the polarization characteristics of each element which complicates the array design. Then, the polarization characteristic of the spiral exhibits special properties that should be analyzed.

In a second part, the configuration of the radiating sources will be analyzed to explain the scanning behavior of the conformal array. Since the platform is not modeled, the three directions of space can be considered to define a volumic array. Unlike classical pattern synthesis, which only activates the element orientated toward the desired scanning direction, inward and outward radiation possibilities yield to a new way of scanning. So, the functioning of the considered volumic array will be described to understand what kind of performances can be achieved.

4.1.1 Polarization aspects

Polarization issue of conformal array

For our application, dual polarization is required, thus, the interest will be focused on the polarization of the element and how it defines the array polarization.

The polarization is one of the main challenges for conformal array pattern synthesis. The polarized pattern defines the polarization of the radiated field according to the direction of radiation. The relation between direction and polarization is obvious but is not a source of problem for planar array where all the elements have the same orientation. An antenna placed on an arbitrarily shaped surface has an orientation depending on its location. Thus, even if the elements are identical, the polarization characteristic, given in the main coordinate system, is not the same. So, conformal arrays can be made of elements with different polarization characteristics, as it is the case for the radiation characteristic. However, while the radiation characteristic can be modulated easily with the excitation, the polarization depends only on geometrical design of the antenna and cannot be modulated (except if the antenna has a reconfigurable polarization).

A simple case of a circular array is illustrated in Fig. 4.1. It points out the importance of the orientation of antenna elements in a conformal array configuration. The elements of the vertical dipoles circular array have all the same orientation. Thus, for each direction, every element radiates

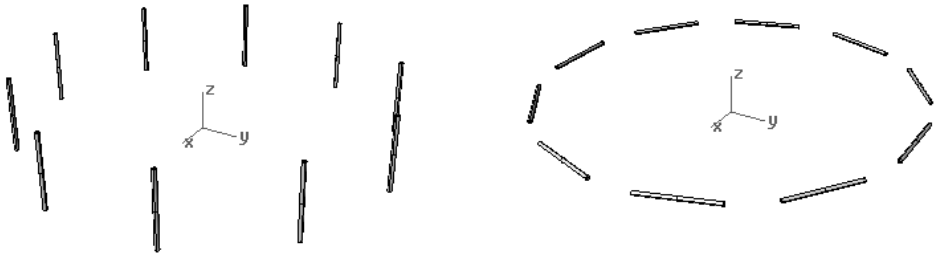

Figure 4.1: *Circular arrays of dipoles in vertical configuration (left) and horizontal configuration (right).*

the same polarization and, thus, the polarization issue does not appear here.

However, it can be also seen in Fig. 4.1 (on the right, for the horizontal dipoles circular array) that the elements do not have the same orientation because the dipoles follow the cylindrical geometry shape. Thus, at a given direction, the polarization of the transmitted field by each element will be different. For instance, considering the direction parallel to the **z** axis, **xy** is the plane of polarization and elements have various orientation and polarization. So, the polarization of the element according to its orientation must be accurately taken into account in the pattern analysis of a conformal array to predict its dual polarization scanning performances.

Polarization diversity of antennas

The choice of the spiral antenna as the array element comes essentially from its capability to radiate the same polarization over an entire half space. This feature is expected to simplify the polarization aspects which complicate the array design in a conformal case.

In Fig 4.2, the two polarized radiation patterns are plotted at 600 MHz. It can be described as a RHCP pattern on one side and a LHCP pattern on the other side. However, it must be kept in mind this behaviour is reduced at low frequencies. Chapter 2 gives more details concerning the level of cross-polarization and co-polarization at broadside. The polarization characteristic of the spiral antenna benefits of special features since the two orthogonal polarizations (RHC and LHC) can be radiated simultaneously in opposite directions with a symmetric behavior. The spiral is a chiral element, i.e. it is not superimposable on its mirror image. As a consequence, interesting properties of polarization can be observed, one face is left handed and the other face is right handed.

Thus, the spiral antenna as a unique polarization diversity in its radiation pattern that would be useful for our application since it radiates simultaneously RHCP and LHCP at different directions. However, it is really challenging since it is difficult to select only one polarization.

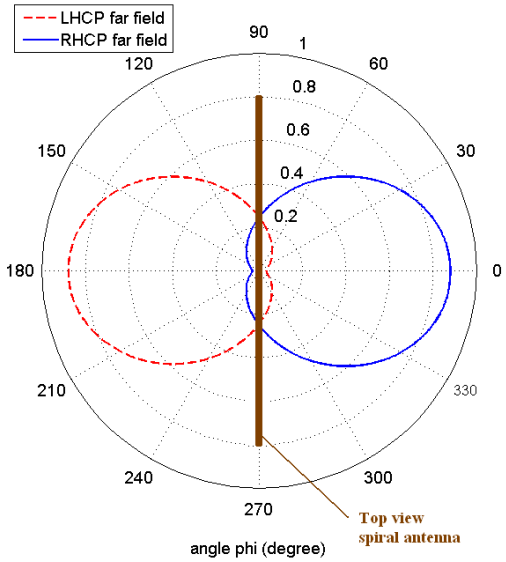

Figure 4.2: *Top view of the spiral antenna with its polarized radiation patterns. Azimuth plane representation ($\theta = 90°$)*

4.1.2 Volumic array scanning

Metallic ground plane issue

Metallic ground planes are used in array design for two reasons. The first is to shield the antenna from the feeding cables and electronic devices interactions. The second is to bring high directivity to the antennas which radiate outward the platform, improving the gain. An example of commercial existing spiral antenna technology is depicted in Fig. 4.3(a). The spiral antenna radiation can be improved if a backed cavity is added allowing radiating in only one direction with an enhanced gain. However, the cavity, as a metallic groundplane is also known to reduce the antenna bandwidth and degrades polarization purity.

Nevertheless, the interaction with a non canonical shape platform is so prohibiting, that most of the conformal arrays concern non planar array using well known metallic ground plane. It must be noticed that an inflatable structure, like an airship, might be the only one platform to strictly forbid the metallic ground plane. Indeed, both dielectric and metallic platform are rigid enough and made of a solid body which enables a ground plane.

As a consequence, the airship platform might be one of the few where inward and outward radiations occur (see Fig. 4.3(b)). The classic conformal array scanning behaviors cannot be considered and new description of the possible scanning has to be investigated.

(a) Spiral antenna with cavity backed.

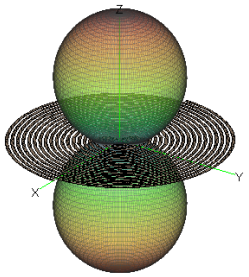

(b) Spiral antenna without cavity backed.

Figure 4.3: *Back radiation issue: a spiral antenna without cavity backed has both front and back radiation beams.*

Inward and outward radiation mechanisms

It is then assumed that the full space radiation pattern of the element is considered, unlike antennas on metallic ground plane where a half radiating space is available. Fig. 4.4 sums up the polarization behavior of antennas located in the opposite sides of the airship, for both transmission and reception cases. The idea is to use the simultaneously radiated RHC and LHC polarizations to achieve scanning in every directions and for both polarizations.

Considering Fig. 4.4, we expect to synthesize a beam radiating toward the right directions ($\varphi = 0°$) for both RHC and LHC polarizations. Using outward radiation of the elements placed on the right side, it can be easily seen than RHCP beam can be achieved. Moreover, it would be also possible to synthesize LHCP beam radiating toward the right directions ($\varphi = 0°$) using the inward radiation of the elements placed on the left side of the airship. Thus, if both inward and outward radiations of the array are used, it would be possible to synthesize both RHCP and LHCP beam on both sides of the airship, with only one array conformed line.

It can be noticed that the inward radiation may interacts with the opposite part of the array. However, in Chapter 3, it has been shown that the coupling between elements positioned on the opposite side of the airship is low, probably due to the distance between the two airship sides. Thus, using the symmetry of the configuration, we obtain the two types of polarization for both sides of the airship.

So, the considered array is depicted in Fig. 4.5. All the antenna are turned RCHP radiating outward and LHCP inward. It can be noticed that the parts of the array located on the low curvature sides of the array can be approximated by two flat parallel arrays, functioning as described above.

Hence, the array can be seen as a two layers array, where the upper layer radiates RHCP and the lower layer radiates LHCP toward the 180°.

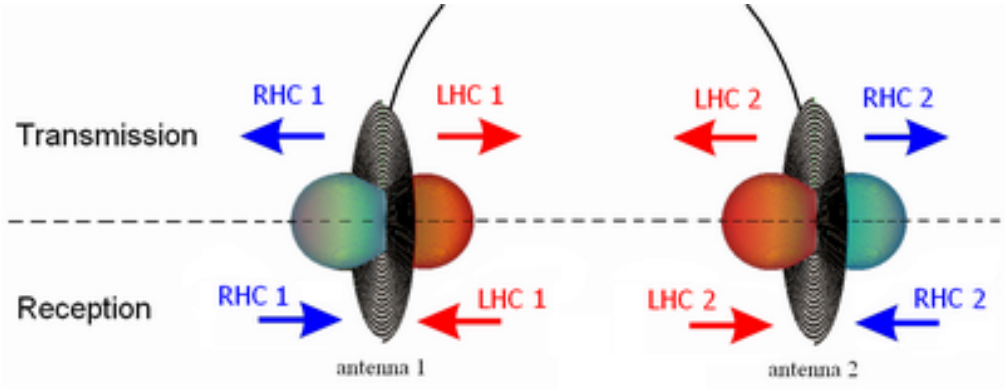

Figure 4.4: *Polarization behavior diagram, according to the spiral antenna location, in transmitting and receiving mode. The direction of radiation $\varphi = 0°$ and $\varphi = 180°$ are considered.*

4.2 Radiation pattern synthesis

The configuration of the array has been described and mechanisms of polarizations for the conformal case have been particularly stressed. The chosen array configuration is expected to synthesize beams for both polarizations at any scan angle. However, the feasibility and performances of the scanning array have to be demonstrated. Thus, a radiation pattern synthesis method suitable for conformal array has to be found. It should provide the set of complex excitations required to yield a desired or specified far-field radiation pattern.

After reviewing the existing pattern synthesis methods dedicated to conformal array, a numerical method will be chosen and described. Then, the performances of the obtainable radiation patterns will be discussed and it will be also determined whether low sidelobe patterns can be achieved.

4.2.1 Review of numerical methods

Some numerical methods to analyze conformal arrays have been already reviewed in Chapter 1. These methods have been developed to study the interactions between the platform and the antennas. In this section, attention is paid on pattern synthesis methods developed for conformal array. Indeed, the excitation magnitude and phase of the array elements can be adjusted in order to maintain low sidelobes as the array is scanning. The desired magnitude and phase weights for

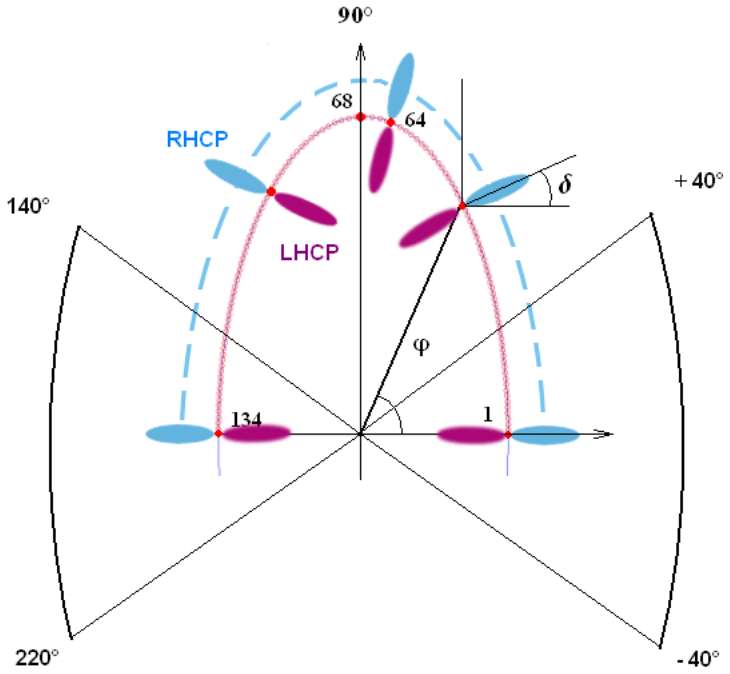

Figure 4.5: *Conformal array configuration. The 134 elements are turned RHCP radiating outward and LHCP radiating inward.*

maximum gain are deterministically set by the array geometry and scan angle. So the purpose consists in finding the appropriate coefficients producing the desired radiation pattern.

Global numerical techniques for optimization can be applied to the pattern synthesis of conformal array. The use of genetic algorithm (GA) procedures to optimize conformal array characteristics can be found in [68]. It is applied to a nine-patch element linear array mounted on a circularly cylindrical platform. In [69], a modified Bernstein polynomial is introduced, defined with just four parameters for ease and speed of optimization. A particle swarm optimizer (PSO) sets these four parameters to synthesize low array sidelobe amplitude distributions for a conformal array at various scan angles. In [70], a simulated annealing technique, which allows the inclusion of constraints in the variability of the excitations in the synthesis procedure, is proposed to synthesize radiation patterns of three-dimensional conformal arrays.

The pattern synthesis for conformal array problem has been also expressed in a least squares form. In [71], an iterative least-squares synthesis technique is explained, where synthesis examples are given for an array on a sphere with circular polarized elements. Then, a modified least-squares optimization is studied in [72], where a phase synthesis with predefined amplitudes can be done from

constraints written for the element excitation amplitudes. Another approach based on Huygens's equivalence principle has been developed in [73]. The reference field is composed of cylindrical or spherical sector wave modes which are superposed to produce the desired far field. Array element weights can then be derived by projection of the reference fields onto the element positions.

The Alternate Projection (AP) method has been proposed in [7], where the element excitations are selected for conformal arrays by choosing only the desired patterns from a subspace of all possible radiation patterns. This method is used in several papers which propose designs similar to the one proposed in this report. In [74], AP method is used for a line array wrapped around a wing including the effects of mutual coupling and the local radius of curvature. In [75], the mutual coupling is also included. In [76], a very similar method, called the vector space projection method (VSP), is discussed. It is demonstrated that VSP is useful for broad-band self-healing arrays (i.e., the reconfiguration of the array when some broad-band elements fail to operate). Furthermore, in [77], taper efficiency comparisons for conformal array beam synthesis are given. It has been concluded that the AP method synthesized patterns are closest to the desired patterns, closely followed by the GA method. The GA method was programmed to optimize taper efficiency, but it takes much longer to run than the other two methods.

So, the flexibility and efficiency of the AP method have been demonstrated for various applications in many papers. Consequently, AP has been chosen for our application, to find the complex excitation coefficients set able to synthesize a desired power pattern.

4.2.2 Alternate projection method

The AP method is an iterative numerical approach where the pattern synthesis is obtained after alternating projections. The algorithm works for one given pattern shape, i.e. at one given scan angle. Thus, it has to be repeated for each scan angle. Furthermore, the optimization procedure is performed for polarization LHC and RHC successively. In this method, the radiation pattern is calculated from the array geometry and from a set of excitation coefficients. Therefore, the approximated method developed in Chapter 2 is used to compute the radiation pattern and is included in the AP method procedure. Hence, the realizable pattern $\mathbf{F}_r(\theta, \varphi)$ is calculated as given by Eq. 4.1 and Eq. 4.2.

$$\mathbf{F}_r(\theta, \varphi) = \sum_{m=1}^{M} \mathbf{a}_m e^{j\Phi_m} \mathbf{E}_m(\theta, \varphi) \tag{4.1}$$

$$\mathbf{F}_r(\theta, \varphi) = \sum_{m=1}^{M} \mathbf{a}_m \mathbf{g}_m(\theta, \varphi) \tag{4.2}$$

with

$$\mathbf{g}_m(\theta,\varphi) = e^{j\Phi_m}\mathbf{E}_m(\theta,\varphi) \tag{4.3}$$

The vector $\mathbf{a}_m$ represent the complex excitation coefficients of the M elements. The phase shift Φ_m and the rotated radiation characteristic of the element $\mathbf{E}_m$ are the same as described in Chapter 3. The desired patterns $\mathbf{F}_d$ is shown in Fig. 4.6 and is defined by the upper bound $B_u(\theta,\varphi)$ and the lower bound $B_l(\theta,\varphi)$. $\mathbf{F}_r(\theta_i,\varphi_i)$, as well as $\mathbf{F}_d(\theta_i,\varphi_i)$, describes radiation patterns defined at discrete samples (θ_i,φ_i), with i the number of the sample.

Fig. 4.7 shows the successive steps to obtain the complex excitation coefficients vector $\mathbf{a}_m$. First, an initial realizable pattern $\mathbf{F}_r(\theta_i,\varphi_i)$ is calculated with Eq. 4.2 from a uniform unit vector $\mathbf{a}_m = 1$ of dimension $\mathbf{M}$. Then, $\mathbf{F}_d(\theta_i,\varphi_i)$ is built from the initial $\mathbf{F}_r(\theta_i,\varphi_i)$ with the following procedure for each sample i.

$$\text{if} \quad B_l(\theta_i,\varphi_i) \leq |\mathbf{F}_r(\theta_i,\varphi_i)|^2 \leq B_u(\theta_i,\varphi_i) \quad \text{then,} \quad \mathbf{F}_d(\theta_i,\varphi_i) = \mathbf{F}_r(\theta_i,\varphi_i) \tag{4.4}$$

$$\text{if} \quad |\mathbf{F}_r(\theta_i,\varphi_i)|^2 \leq B_l(\theta_i,\varphi_i) \quad \text{then,} \quad \mathbf{F}_d(\theta_i,\varphi_i) = \sqrt{B_l(\theta_i,\varphi_i)}\frac{\mathbf{F}_r(\theta_i,\varphi_i)}{|\mathbf{F}_r(\theta_i,\varphi_i)|} \tag{4.5}$$

$$\text{if} \quad |\mathbf{F}_r(\theta_i,\varphi_i)|^2 \geq B_u(\theta_i,\varphi_i) \quad \text{then,} \quad \mathbf{F}_d(\theta_i,\varphi_i) = \sqrt{B_u(\theta_i,\varphi_i)}\frac{\mathbf{F}_r(\theta_i,\varphi_i)}{|\mathbf{F}_r(\theta_i,\varphi_i)|} \tag{4.6}$$

It must be noticed that the bounds $B_u(\theta,\varphi)$ and $B_l(\theta,\varphi)$ define power values of the desired pattern. Then, the M complex excitation coefficients $\mathbf{a}_m$ are obtained with the inversion of the matrix $\mathbf{g}_m$ in the least mean square sense (see Eq. 4.7).

$$\mathbf{a}_m = \mathbf{g}_m^{-1}\ \mathbf{F}_d \tag{4.7}$$

Finally, a new $\mathbf{F}_r$ is obtained using the new set of $\mathbf{a}_m$ given by Eq. 4.7

$$\mathbf{F}_r = \sum_{m=1}^{M} \mathbf{a}_m\mathbf{g}_m \tag{4.8}$$

The new realizable pattern $\mathbf{F}_r$ can thus be projected again on the desired pattern in a new iteration, until the convergence of the algorithm. It must be noticed that the computation of the $\mathbf{F}_r$ takes into account the orientation of the element radiation patterns thanks to the approximated method and thus suits well to the conformal configuration.

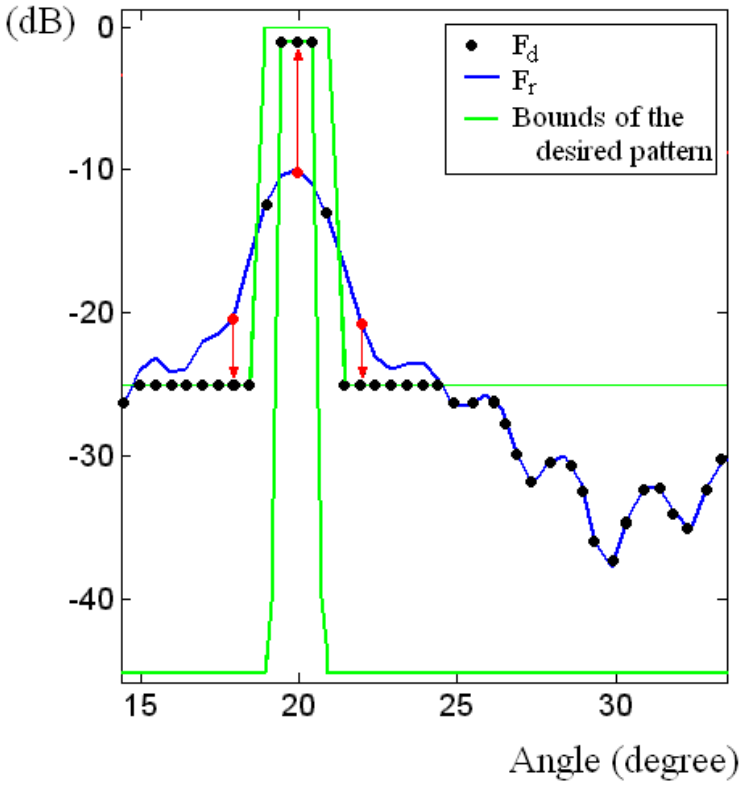

Figure 4.6: *Alternate Projection method - radiation pattern representation. The* $\mathbf{F}_d$ *samples are obtained from the realizable pattern* $\mathbf{F}_r$ *projected on the bounds* B_u *and* B_l *of the desired patterns.*

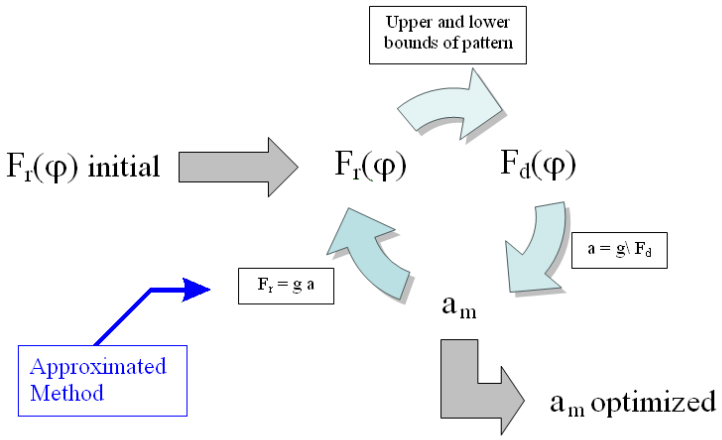

Figure 4.7: *Flow diagram of the Alternate Projection method.*

4.2.3 Performances results

AP method combined with the approximated method is used to calculate the conformal array radiation pattern in order to validate its performances. The half-ellipse shape conformal array is considered, with the 134 spiral antennas all turned RHCP outward as shown in Fig. 4.5. Fig 4.6 shows a zoom of the desired pattern for a scanning angle at $\varphi = 20°$. The bounds $B_u(\varphi)$ and $B_l(\varphi)$ of the desired pattern are set for a sidelobe level at -25 dB and a main beam width of 2°.

Scanning is performed in the azimuth plane, at every 10° over 360° to demonstrate the capability to synthesize a beam at various directions. Practically, the AP optimization has to be repeated for each scan angle i.e. 36 different optimizations. This is repeated for both RHC and LHC polarization and thus 72 optimizations are required to demonstrate the dual polarization beamforming feasibility. However, this is not really time consuming, since it has been observed that less than 10 iterations are necessary for the convergence of the algorithm. Thus, the excitations set have been found for both polarization cases at various scan angles in less than 30 minutes.

Fig 4.8 shows RHC polarized patterns optimized at various scan angles, obtained by neglecting the coupling between elements. Both co-polarization (RHCP in this figure) and cross polarization (LHCP in this figure) components of the far field are depicted. To each element of the array corresponds an excitation coefficient given by the AP method and this, at each scan angle. Some excitation coefficients have a lower magnitude than others and thus the corresponding element has a smaller contribution to the pattern synthesis. As a consequence, on the left part of Fig 4.8, only the antennas with a magnitude value higher than the third of the maximum magnitude of the coefficients are plotted.

From Fig 4.8(a), Fig 4.8(b), Fig 4.8(c), it can be observed that, as predicted in Section 4.1.2, the participating antennas are the antennas "looking" toward the scanning direction. Indeed, the outward radiations of spiral antennas are used to synthesize the RHC polarized beam. A symmetrical behavior of the participating array elements exists between an optimized RHCP pattern and a LHCP optimized pattern. Thus, for a LHCP beam, inward radiations of the array elements located opposite to the scanning direction would be used.

It can be seen that the cross-polarization level reaches -15 dB for the first three examples shown in Fig 4.8(a), Fig 4.8(b), Fig 4.8(c). Nevertheless, in Fig 4.8(d) the level of the cross polarization is higher. Indeed, optimization of RHCP pattern requires an outward radiation from the part of the array pointing to the chosen direction. In this last case, where a beam at $\varphi = 290°$, must be synthesized, no outward array element exists and the inward radiation of the antennas cannot provide RHCP radiation with low cross-polarization. This is because only a half ellipse array is considered. A circular or a full ellipse array would achieve this, but for practical reasons, the back part of the airship is not available.

The cross-polarization level at every scan angle for both RHCP and LHCP pattern is plotted in Fig 4.9. It can be observed that a co-polarized RHCP beam (blue) can be synthesized with a cross polarization (LHCP) level under -10 dB at any angle except directions from $\varphi = 220°$ to $\varphi = 320°$. The symmetric behavior between RHCP and LHCP beam synthesis can be clearly seen. Indeed, a co-polarized LHCP beam (red) can be synthesized with a cross polarization (rHCP) level under -10 dB at any angle except directions from $\varphi = 40°$ to $\varphi = 140°$ because no element radiates inward in these directions. In conclusion, if both RHCP and LHCP beam have to be achieved with low cross polarization level, scanning angles corresponding to the side looking of the airship have to be respected. That corresponds to a $\pm 40°$ scanning possibilities on both sides (see Fig. 4.5).

The AP pattern synthesis method has shown its efficiency for this non-conventional array. High quality patterns with low sidelobes have been achieved for most scan angles. The scanning using the high curvature part of the array does not allow synthesizing the beam for both polarizations and for any direction. Only RHCP field can be radiated outward and only LHCP field can be radiated inward, because only one layer of array is considered for these directions.

Furthermore, no convergence problems due to local minima occurred. However, it has been noticed that the method is more efficient if the main beam of the desired pattern is thin. This effect may be due to the fact that if the constraint is high in terms of directivity, only one direction is optimized and the back lobe radiated opposite to the desired direction is canceled. Tests have been led with different desired pattern shapes, trying to lower the sidelobe level. Unfortunately, it has not been possible to lower the side lobe level, even if the condition on the beam width is weaker.

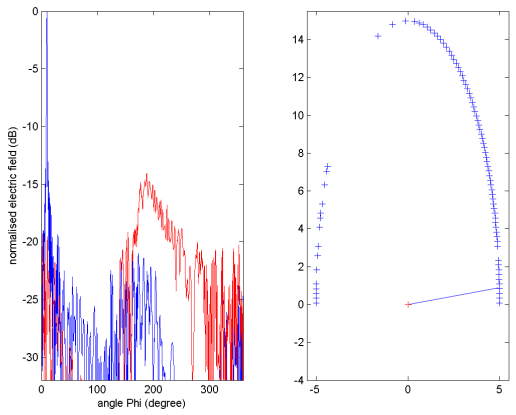

(a) RHCP beam scanning at 10°.

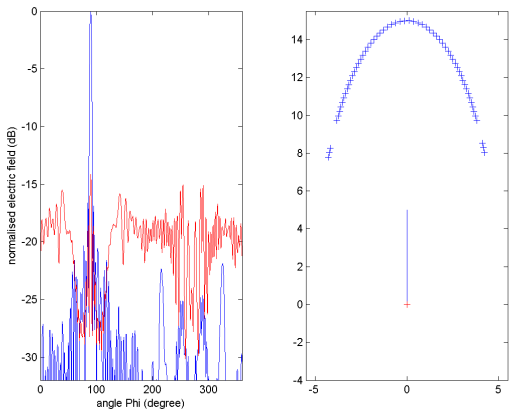

(b) RHCP beam scanning at 90°.

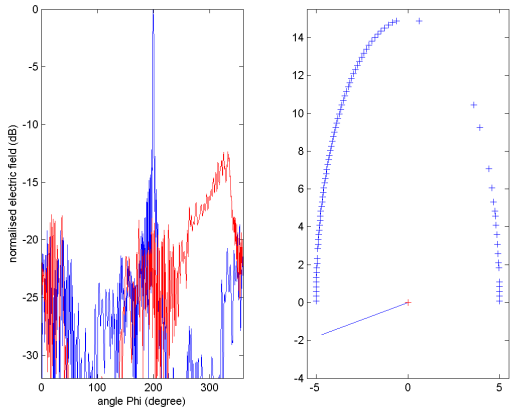

(c) RHCP beam scanning at 200°.

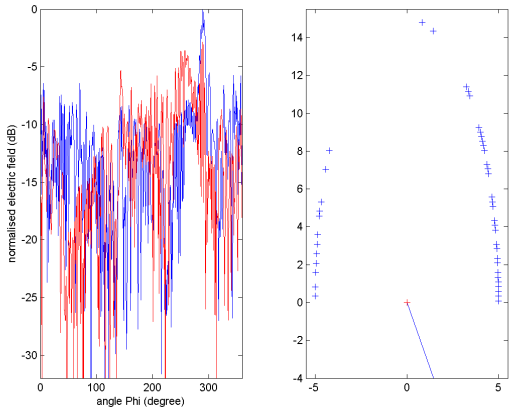

(d) RHCP beam scanning at 290°.

Figure 4.8: *Radiation patterns of the co-polarization (RHCP in blue) and the cross-polarization (LHCP in red) obtained using AP method (10 iterations). RHCP beam has been optimized at various angles. The right parts of the figures show the position of the contributing elements. All the antennas radiate RHCP outward.*

4.3 Heterogeneous array

It has been pointed out that the limitations of the array in synthesizing polarized beam in some directions comes from the array arrangement and the spiral antenna polarization characteristic. In the previous array design, all the elements of the array where turned RHCP outward. It has been shown that for some scan angles, one of the two polarizations cannot be achieved because of the

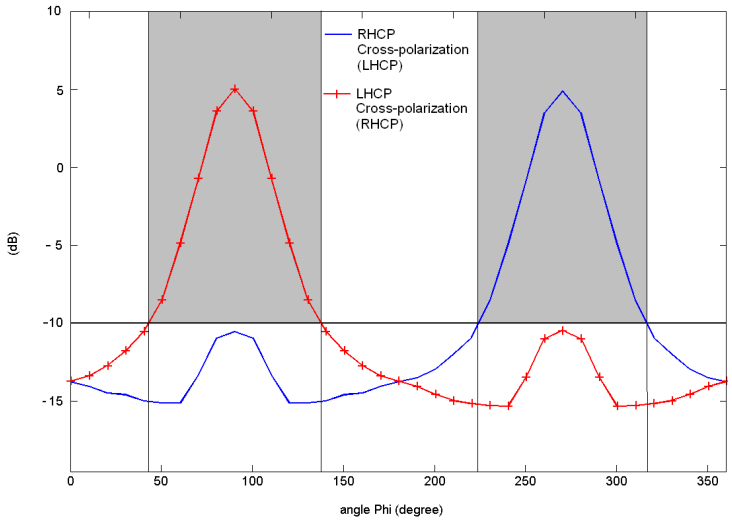

Figure 4.9: *Cross-polarization level versus desired angle of radiation, for a RHCP and LHCP optimized main beam. Homogeneous array case, all antenna are turned RHCP outward*

lack of elements turned in the correct directions. Thus, the limitations concern the array and not the AP algorithm. So, changes must be done in the array arrangement.

A spiral antenna has two faces: one is radiating RHCP, one is radiating LHCP. Thus, two possibilities exist to conform a spiral to the airship surface: the RHCP face outward or the LHCP face outward. It is necessary to have at any location of the array, both RHCP and LHCP radiating elements. Previous work led in the SONDRA laboratory [78] have shown in the non-conformal case, that it would be possible to obtain both polarizations with only one spiral array if an interleaved array is used.

So, the interleaving feasibility in conformal case will be investigated. First, the AP method must be adapted to the new array configuration and performances of the array will be described. Specific advantages of the conformal interleaving will also be highlighted.

4.3.1 Heterogeneous array configuration

The array is considered as heterogeneous since the interleaved array is composed by spirals turned RHCP outward and spirals turned LHCP outward. Thus, it is composed by two different elements and can also be seen as two unequally-spaced arrays, sharing a same surface and aperture.

Unequally spaced array

A theoretical approach of unequally spaced arrays has been described in [60]. It stressed some interesting capabilities of using large array with unequally spaced elements. It has shown that sidelobe reduction for an array of uniform amplitude could be achieved and that it is also possible to suppress the secondary beam and to perform an azimuthal frequency scanning. This is well appropriated for our case where the secondary beam has to be reduced if the scanning covers 360° coverage.

The interleaving of two arrays in the same aperture area has been proposed in [79] in order to improve the efficiency of an array aperture. Thinned array turns elements off in a uniform array in order to obtain a spatial taper that results in low sidelobes, but uses inefficiently the space. Hence, the interleaving of two arrays solves this waste of space and allows to use two array with various purposes. As a consequence it demonstrates the feasibility of achieving two interleaved arrays, one radiating the co-polarization, the other radiating the cross-polarization, in the same aperture.

Radiation pattern computation

The computation of the radiation pattern will take into account the antenna element diversity. The spiral antennas can be considered as two different types of antennas: RHCP outward (antenna type **A**) or LHCP outward (antenna type **B**). In this configuration, the difficulty comes from the fact that each element radiates simultaneously the co-polarization and the cross-polarization. Hence the polarized components $\mathbf{E}^{tot,rhcp}$ and $\mathbf{E}^{tot,rhcp}$ of the total radiated far field must each be calculated using both type of antennas:

$$\mathbf{E}^{tot,rhcp}(\theta,\varphi) = \sum_{m=1}^{M} \mathbf{E}_m^{antA,rhcp}(\theta,\varphi) + \sum_{m=1}^{M} \mathbf{E}_m^{antB,rhcp}(\theta,\varphi) \tag{4.9}$$

$$\mathbf{E}^{tot,lhcp}(\theta,\varphi) = \sum_{m=1}^{M} \mathbf{E}_m^{antA,lhcp}(\theta,\varphi) + \sum_{m=1}^{M} \mathbf{E}_m^{antB,lhcp}(\theta,\varphi) \tag{4.10}$$

with $\mathbf{E}_m^{antA}$ the field radiated by the antenna type **A** (RHCP outward) and $\mathbf{E}_m^{antA}$ the field radiated by the antenna type **B** (LHCP outward).

The ellipse is symmetric with respect to the axis **y** (at $\varphi = 90°$). In order to keep a symmetrical behavior of the array radiations, the complementary symmetry of the array is kept. The sequence of antenna **A** and antenna **B** is randomly determined for half of the array (element 1 to element 67). Then, elements 68 to 134 are obtained as the complementary of the first part of the sequence (**A** becomes **B**, **B** becomes **A**). Hence, a symmetrical array can be composed as seen in Fig 4.10.

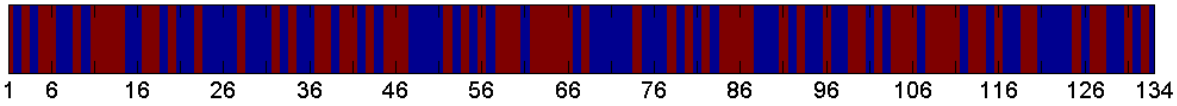

Figure 4.10: *Interleaved 134-element array sequence composed by two types of spiral antennas. Antennas type **A** radiate RHCP outward (in blue) and antenna type **B** radiate LHCP outward (in red). The sequence is randomly determined and is complementary symmetric.*

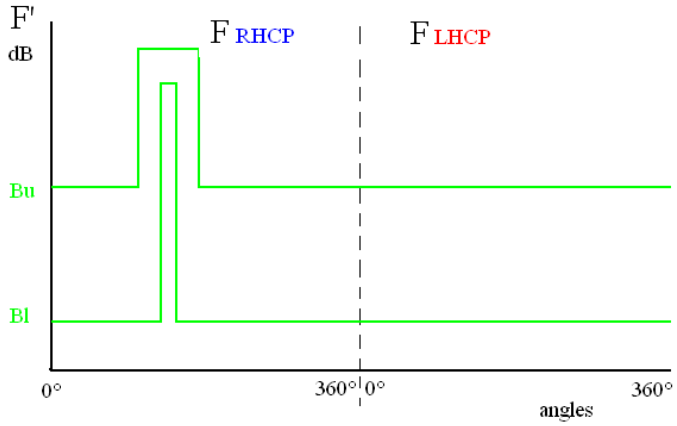

Figure 4.11: *Modified desired patterns, obtained by concatenation of the RHCP pattern and the LHCP pattern, in order to use the AP method simultaneously for the two polarizations.*

AP for heterogeneous array

Since two types of antennas are now considered, the AP algorithm has to be modified. The optimization can be done for both the co-polarization and the cross-polarization. The realizable pattern $\mathbf{F}_r(\theta,\varphi)$ as well as the desired pattern $\mathbf{F}_d(\theta,\varphi)$ are defined at discrete samples (θ_i,φ_i) for each polarization. Both polarizations can be simultaneously optimized, building a function $\mathbf{F}'_r(\theta,\varphi)$ which is the concatenation of $\mathbf{F}_r^{rhcp}(\theta,\varphi)$ and $\mathbf{F}_r^{lhcp}(\theta,\varphi)$ as it can be seen in Fig 4.11. Hence, the size of $\mathbf{F}'_r(\theta,\varphi)$ is twice that of $\mathbf{F}_r^{rhcp}(\theta,\varphi)$. Eq. 4.7 can still be used to obtain M excitation coefficients $\mathbf{a}_m$. The upper bound $(B_u(\theta,\varphi))$ and lower bound $(B_l(\theta,\varphi))$ of the pattern are defined also for both RHCP and LHCP components (see Fig 4.11).

4.3.2 Performance results

The excitation coefficients and the corresponding synthesized radiation patterns are computed using the modified AP method for the interleaved array case. Radiation patterns for both RHC and LHC polarization cases, at various scan angles, are synthesized. The desired patterns are defined from

the lower and upper bounds B_l and B_u with a main beam width of 2°, a sidelobe level of -25 dB and a cross-polarization level at -25 dB. The main beam varies from 0° to 360° by 10° steps.

Some realizable radiation pattern examples are shown in Fig 4.12, with a main lobe at 10°, 80°, 240°, 280°. In those examples, the main beam has a LHC co-polarization and the RHC cross-polarization is also plotted.

It can be seen that when the main lobe is synthesized at the side directions of the ellipse for the 10° and 240° directions, the level of the cross-polarization is below -10 dB, like the homogeneous pattern. Moreover, an improvement is noticed for the 80° and 280° directions, where the level of cross-polarization, unlike the homogeneous case, almost reaches -10 dB. Thus, if a heterogeneous array is considered, patterns with a main beam radiating at any scan angles can be synthesized, for both polarization, with a low cross-polarization level, and reduced number of elements.

It can be seen from the presented examples of the radiation patterns that the level of the cross-polarization is at least under -10 dB for any scan angle. On the right part of the Fig 4.12 are plotted the location of the elements which participate the more to the pattern synthesis. The element is plotted if its excitation coefficient magnitude is greater than the third of the maximum magnitude among the other coefficients. The color of the elements indicates if it is a type **A** antenna with the RHCP outward (blue) or a type **B** antenna with the LHCP outward (red).

Fig 4.12(a) shows the case of a LHCP main beam radiating at 10°. It can be observed that the participating antennas of type **A** and of type **B** respect the simple rule previously described: both front and back radiation are used for the synthesis. A LHCP main beam, synthesized to radiate on the right part of the ellipse, requires both radiations coming from antennas radiating RHCP inward, located in the left part of the ellipse, and antennas radiating LHCP outward, located in the right part. Fig 4.12(c) shows the inverse case where a LHCP beam is synthesized to radiate toward the left direction. Comparing Fig 4.12(a) and Fig 4.12(c), it can be observed that the antennas activated of type **A** are located in opposite sides, like antennas of type **B**.

The complementary symmetry of the array yields to a balanced distribution of the antenna type **A** and type **B** on the various locations of the array. Hence, since the array is complementary symmetric, if a beam of one polarization can be achieved toward right direction, a cross polarized one can also be obtained, in the opposite direction. The distribution of the excitation coefficients is symmetric.

Fig 4.12(b) and Fig 4.12(d) illustrate the cases where a main beam must be synthesized at scan angles when front and back radiations are not possible, only one part of the array has elements faced to the desired scan angles. In the homogeneous array case, only one polarization could be achieved. However, for the heterogeneous configuration, the lack of symmetric array is compensated by the interleaving method. Indeed, the presence of both co-polarized and cross-polarized antennas at any part of the array allows to synthesize either LHCP or RHCP beam at both ($\varphi = 90°$) and ($\varphi = 270°$) scan angles. LHCP main beam at a 80° (Fig 4.12(b)) direction uses mainly antennas turned LHCP

outward and LHCP main beam at a 280° (Fig 4.12(d)) scan angles uses mainly antennas turned RHCP outward. So, radiation patterns with low level of cross polarization can be achieved using the existing antennas of the array turned in the desired direction.

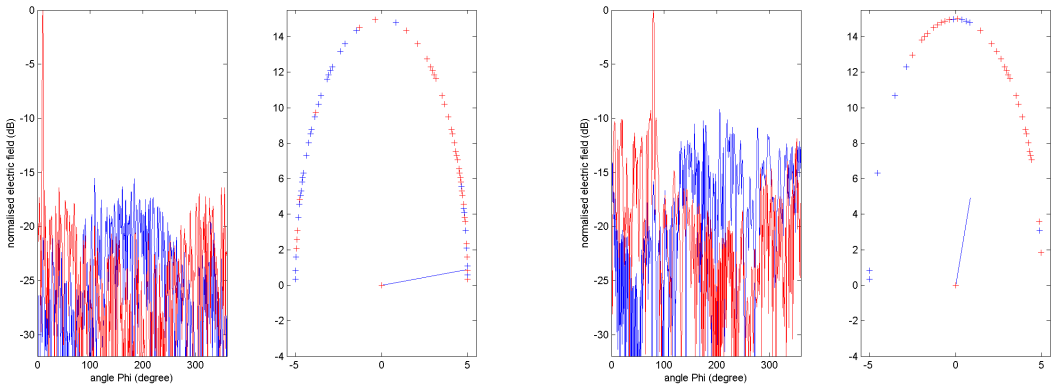

(a) LHCP beam scanning at 10°.

(b) LHCP beam scanning at 80°.

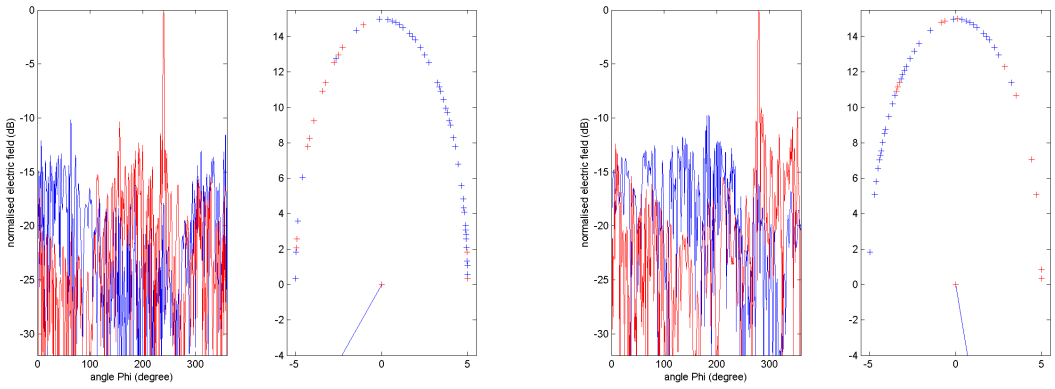

(c) LHCP beam scanning at 240°.

(d) LHCP beam scanning at 280°.

Figure 4.12: *Radiation patterns of the co-polarization (LHCP in red) and the cross-polarization (RHCP in blue) obtained using AP method (10 iterations). LHCP beam has been optimized at various angles. The right parts of the figures show the position of the contributing elements. Antennas radiating LHCP outward in red, antennas radiating RHCP outward in blue.*

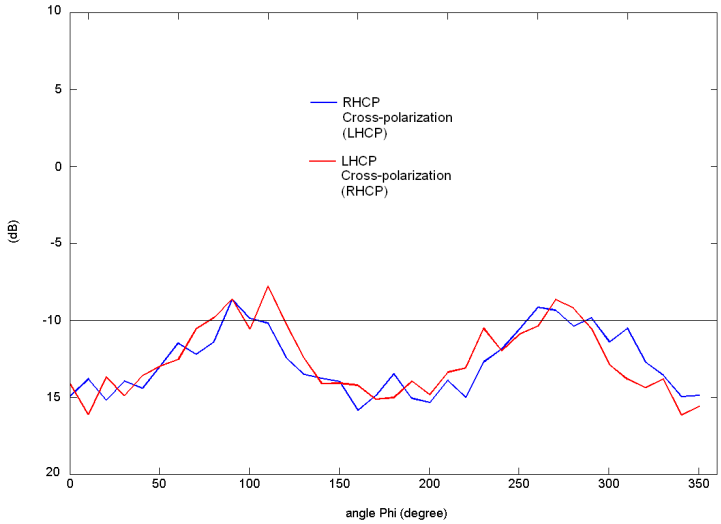

Figure 4.13: *Cross-polarization level versus desired angle of radiation, for a RHCP and LHCP optimized main beam. Interleaved array case, both RHCP and LHCP turned outward antennas are used.*

4.3.3 Reduction of the excitation number

A study of the coefficients applied to the array elements obtained by the AP method has revealed that some coefficients are low enough to be forced to zero. This could simplify the pattern synthesis, using less than 134 elements. It has been found that the coefficient $\frac{1}{3}$ represent a good compromise between a small number of array elements and a low cross-polarization level. Thus, a new set of excitations $\mathbf{a}_m$ is defined as following:

$$\text{if} \quad |\mathbf{a}_m| \leq \frac{1}{3} Max\,|\mathbf{a}_m| \quad \text{then} \quad \mathbf{a}_m = 0 \tag{4.11}$$

$$\text{if} \quad |\mathbf{a}_m| \geq \frac{1}{3} Max\,|\mathbf{a}_m| \quad \text{then} \quad \mathbf{a}_m = \mathbf{a}_m \tag{4.12}$$

Performances

Thanks to the non equally space arrangement, the radiation patterns after reduction of the number of excited antennas are really similar to those with 134 excited elements. It has been shown that it is possible to achieve low-cross polarization using all elements of the array in the direction 280° in Fig 4.12(d). Nevertheless, it is necessary to evaluate the possibility of switching some elements off, respecting the same low cross-polarization level condition. So, the cross-polarization level versus the scan angle is plotted in Fig.4.13, for both RHCP and LHCP optimized patterns.

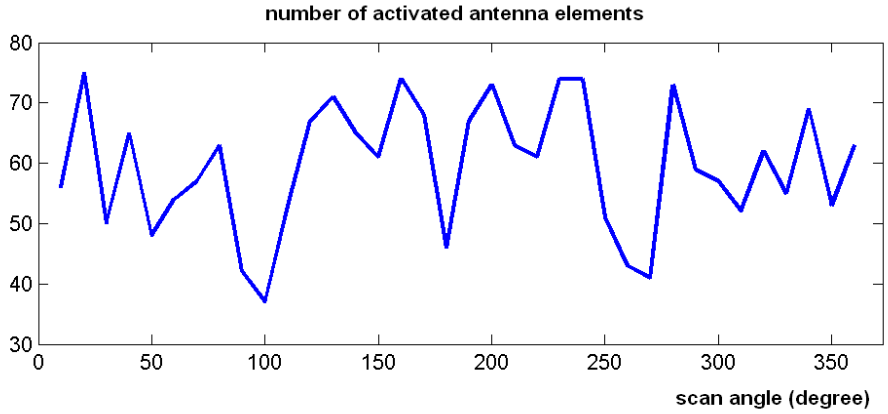

Figure 4.14: *Evolution of the number of element used according to the angle of the main beam optimized (Top). Comparison between the sum of the excitation coefficient magnitude when all elements are used and when the number of used elements is reduced.*

Reduced excitation evaluation

The advantage of reducing the number of excited elements is to reduce the number of data, neglecting the contribution of some sensors since some coefficients have been forced to zero. In order to evaluate the reduction, the number of elements used according to the scan angles is investigated and plotted in Fig 4.14. It can be observed that only 37 to 76 elements are necessary to obtain the desired radiation pattern with a cross-polarization level, presented in Fig. 4.13, instead of the 134 available. So, it means that even if the whole array is considered in the pattern synthesis method, only about half of the elements are really contributing. Furthermore, it demonstrates also the robustness of an interleaved configuration, where some chosen elements can be turned off without perturbing the array functioning.

The minimum number of elements required is reached when the main beam is pointed at scan angles ($\varphi = 90°$) and ($\varphi = 270°$), corresponding to the high curvature zone of the array (see Fig 4.5). For those scan angles, only one zone of the array is activated. At scan angles around ($\varphi = 0°$) and ($\varphi = 180°$), both front and back radiations of the array are used, two parts of the array lying on the airship sides are activated. Thus, the maximum number of elements is used allowing a low level of cross-polarization.

The magnitude of the excitation coefficients according to the element position and the angle of the main beam synthesized is plotted in Fig.4.15. On the left part (Fig.4.15(a)) is plotted the magnitude of the excitation set given by the AP method. On the right part (Fig.4.15(b)) is plotted the magnitude of the excitation set when the weaker coefficients are forced to zero. The evolution of

the excitation coefficients is clearer in the Fig.4.15(b), where the contrast is better. Two behaviors can be clearly seen. The first is when the main beam focuses at angles between 80° and 100° or between 260° and 280°, where the beam is steered in the airship forward and backward directions. The elements excited are located in the center of the array, i.e. in the nose of the airship. The second is when the main beam focuses at angles between 10° and 70° or between 110° and 250°, or between 290° and 360°, where the beam is steered toward the right and left sides directions of the airship. The elements excited are more homogeneously distributed and this characterizes the front and back radiation mode.

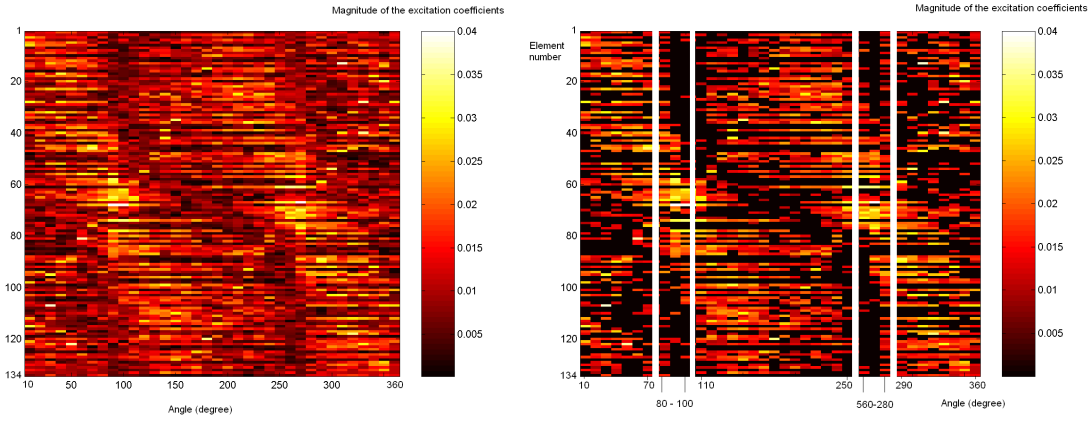

(a) All the elements are excited.

(b) Reduced number of elements are excited.

Figure 4.15: *Magnitude of the excitation coefficients according to the element position and the angle of the main beam synthesized.*

4.4 Conclusion of Chapter 4

In this chapter, the capabilities of a dual polarization scanning of the conformal array are investigated. First, an analysis of the conformal array has been done in order to understand its behavior when scanning. The non classical host platform features have been stressed. It has been shown that unlike traditional designs, the spiral antenna can be used over a full 3D space. It has been demonstrated that the non-interacting platform and the conformal array configuration bring new possibilities of scanning.

Furthermore, the polarization aspects play an important role in the scanning possibility and makes the study more complex. It has been explained that the spiral has chiral properties providing the unique ability of radiating cross-polarized waves in opposite directions. This allows to have the same polarization over a half space that simplifies the polarization issue of conformal array. Furthermore, it has been demonstrated that the use of the back and front lobe of the spirals allows to synthesize both polarizations in several directions using only one conformal linear array.

Then, the alternate projection pattern synthesis method has been chosen to find the appropriate excitation coefficients at various directions for both polarizations. The approximated method previously developped has been integrated in the optimization procedure to compute the resulting radiation patterns. It has been found that radiation pattern with a low cross-polarization level could be achieved when the beam is radiated by the antennas located in the airship sides with a $\pm 40^{\circ}$ steering. Nevertheless, a beam pointing at the front and back directions of the airship could not be achieved because only a half ellipse shape is used.

Finally, an interleaving technique has been proposed. It has been explained that spiral antennas turned RHCP outward are the complementary of spirals antennas turned LHCP outward. Thus, using this complementarity, both type of elements can be considered depending on the face radiating outward. From the radiation patterns obtained using the heterogeneous configuration, it has been demonstrated that is should be possible to synthesize both polarized radiation patterns at any scan angles, with a cross-polarization level lower than -10 dB. In addition, the interleaving technique allows to switch off some elements to simplify the beam synthesis.

Furthermore, it has been noticed that the sequence of the elements can be chosen randomly without affecting the pattern synthesis method success. It is believed that this parameter offers an additional degree of freedom that could be used to optimize the radiation pattern.

Chapter 5

Conclusion

The feasibility of mounting an antenna array on airship for radar applications has been investigated. The conformal array has to respect the lightweight and planar technology requirements achieving both wideband and dual polarization performances. Four axis can be distinguished:

1. The design of a conformal wideband array with a low cross-polarization level.
2. The computation of a conformal array radiation pattern.
3. The building and the wideband measurements of a conformal array without ground plane.
4. The investigation on the scanning possibilities of an array using the full space of radiation.

First, the design of a conformal array with wideband and low cross-polarization performances has been achieved and explained. The spiral antenna, which fulfills both the wideband and low cross-polarization requirements, has been chosen as the array element. Hence a 134-element array has been designed and should be effective from 400 to 600 MHz. This choice has been done especially because the spiral radiates almost the same polarization over a full half space and, thus, fits well the conformal configuration requirements. This property has been also emphasized afterward in Chapter 4.

It has been also demonstrated that the bandwidth of a uniform linear scanning arrays is limited by design reasons. The bandwidth is directly linked to the small size of its element, allowing a small inter-element distance to avoid the grating lobes when scanning. It must be highlighted that this limitation can be overcome in two cases. The first is when the array is conformal and thus, not uniformly linear. However, since the half ellipse array shape has quasi-planar parts, the condition of a compact size element must still be respected. The second case is when the array is non equally-spaced. So, it should be interesting to define the achievable bandwidth of the interleaved array, since its scanning study has only been validated at 600 MHz in this report.

Furthermore, it is worth noticing that low frequency arrays with planar technology cannot be mounted on traditional metallic platforms because a quarter wavelength distance is required between the ground plane and the radiating elements. Even, if high permittivity materials could be used to reduce this distance, they are unfortunately really heavy. Thus, it can be said that as a non interacting platform, the airship is at least completely well suited for applications at low frequency, at the cost of avoiding the ground plane.

The computation of a conformal array radiation pattern has been done to solve the computation time issue and to provide a model which could be used in the radiation pattern synthesis method. The idea of making the sum of each contributing elements is quite obvious. Hence, the study of coupling have shown that its value were not so high and could be neglected. This may be due to the fact that the spiral concentrates the current on its center at high frequencies.

The rotation of the radiation characteristic is a simple idea, but the vectorial nature in addition with the discrete values of the radiated field make it more complicated. Interpolations have been used to solve this issue and the different steps have been described in details. Furthermore, the rotation method has also revealed its usefulness in antenna measurements, when the polarization coordinate system, considered for practical reasons during measurements, does not correspond to the polarization coordinate system used for the interpretation of the results. An example is given in Chapter 3, for the conformal array measurements.

The validation of the method has been done through comparisons with measurements and modeling results. Some differences occur, but the main lobe and the polarization characteristic are well reconstructed. So, this method provides a simple way to give the main shape of the radiated pattern of a conformal array. It has the advantage of taking into account the vectorial nature of the field for polarimetric applications and is suitable for any element with low coupling in an array configuration.

Practical approach has also been used for the design and measurements of prototypes in order to validate the modeling results. The first difficulty has been to find a design which integrates the feeding with a minimum of perturbations. It has been observed that the radiation pattern matched the results of modeling over the full space. The measurement of the antenna gain as well as the matrix of coupling of the array have been found similar to the simulation results. However, the measurements probably suffers from the presence of the feeding that has not been taken into account in the simulation. Thus, feedings must be integrated in the design to allow significant measurements.

A work has been led on a coplanar solution for feeding, during the master thesis of Karim Louertani [6]. A pre-existing design that proposed a coplanar feeding has been investigated. It has been stressed that this design could not be used in a scanning array because of a too high lower frequency bound. Thus, a double-excitation spiral coplanar-fed has been designed allowing

both co-planar feeding and its use in an array. This design, based on a symmetrical distribution of current, seems to be very promising and effective to be mounted on the airship.

Finally, the possibilities of scanning have been investigated. It has been emphasized that the platform is very unique since every element, radiating in any direction of space is considered. This provides an original application for the generalization of the classic half space radiating array constrained by the ground plane or the platform. It is thought that the airship is one of the few application for such 3D array, opening new possibilities of scanning. It has been also demonstrated how the polarization mechanisms played an important role in the pattern synthesis. However, the interaction of an inward transmited wave with the array on the oppisite side has to be further investigated.

A pattern synthesis method has been used and gives some examples of achievable radiation patterns. It also shows how the elements participate to the radiation pattern. At last, the design has been enhanced, mixing the two complementary spiral antennas in an interleaved design. The improvement in scanning has been demonstrated for directions all over the airship and for both polarizations. However, the possibilities of this configuration have not been completely studied, the sequence of the antennas has not been optimized. Furthermore, more complex patterns with the possibility to radiate at different angles, different polarizations, in the same time, has not been demonstrated yet.

To conclude this work, some prospects can be mentionned:

- The proposed computation method neglects the coupling and has been validated through comparisons with measurements and modeling results. So this method is valid for the proposed configuration, but its limitations have not been defined. The enhanced complexity of a bi-dimensional array, using interleaved techniques and also integrating the feeding presence, should require a more accurate approach including eventually the mutual coupling.

- The proposed design concerns a conformal linear array able to scan in any direction in the azimuth plane and the results have also been shown in this plane. However, if we consider a flying airship, detecting target located on the ground, the elevation angle has also to be considered. Ground target detection should be achieved adding more rows to the linear conformal array. In that case, we think that the approach, conclusions and methods of the work presented in this report are still valid to this bidimensional array and should be extended.

- It has been clearly shown through practical realizations that the feeding cable strongly impacts the antenna performances. Besides, the proposed coplanar design is innovative and promising. It solves both the measurement issue and provide a manageable array design that

can be mounted on an airship hull surface. An array of coplanar elements should validate the feasibility of a possible light and wideband array suitable for polarimetric radar applications. However, efforts have still to be done in the array topology integrating the feeding, especially if a bidimensional one is considered with a doubly curved surface.

Publications

Journals

- F. Chauvet, R.Guinvarc'h and M. Hélier, "Approximated method neglecting Coupling for Conformal Array," *Applied Computational Electromagnetics Society Journal, Special Issue on ACES 2006 Conference*, Vol. 22 No. 1, pp. 105-111, March 2007, ISSN 1054-4887.

Conferences

- F. Chauvet, R.Guinvarc'h and M. Hélier, "Polarized scanning possibilities of a conformal wideband array," in *in Proc. Internationa Symposium on Antennas and Propagation*, Niigata, Japan, Aug. 2007.
- F. Chauvet, R.Guinvarc'h and M. Hélier, "Réseau large bande conformé sur dirigeable," in *Proc. Journée Nationales Microondes*, Toulouse, France, May. 2007.
- F. Chauvet, R.Guinvarc'h and M. Hélier, "Non uniformly curved conformal wideband array," in *Proc. European Conference on Antennas and Propagation*, Nice, France, Nov. 2006.
- F. Chauvet, R.Guinvarc'h and M. Hélier, "Coupling between spiral antenna elements of a conformal wideband array," in *Proc. Applied Computational Electromagnetics Society*, Miami, USA, March. 2006.
- F. Chauvet, R.Guinvarc'h and M. Hélier, "Conformal phased array antenna for high altitude airship," in *Proc. 4th Eur. Workshop Conformal Antennas*, Stockholm, Sweden, May, 2005.

Appendix

List of the components used for the antenna array building

- **Substrate**: 25N (Cirly)
- **Transformer**: TC4-14+ (Minicircuits)
- **Power splitter 2-1**: ZAPD-23+ (Minicircuits)
- **Power splitter 4-1**: ZB4PD-1750-75 (Minicircuits)

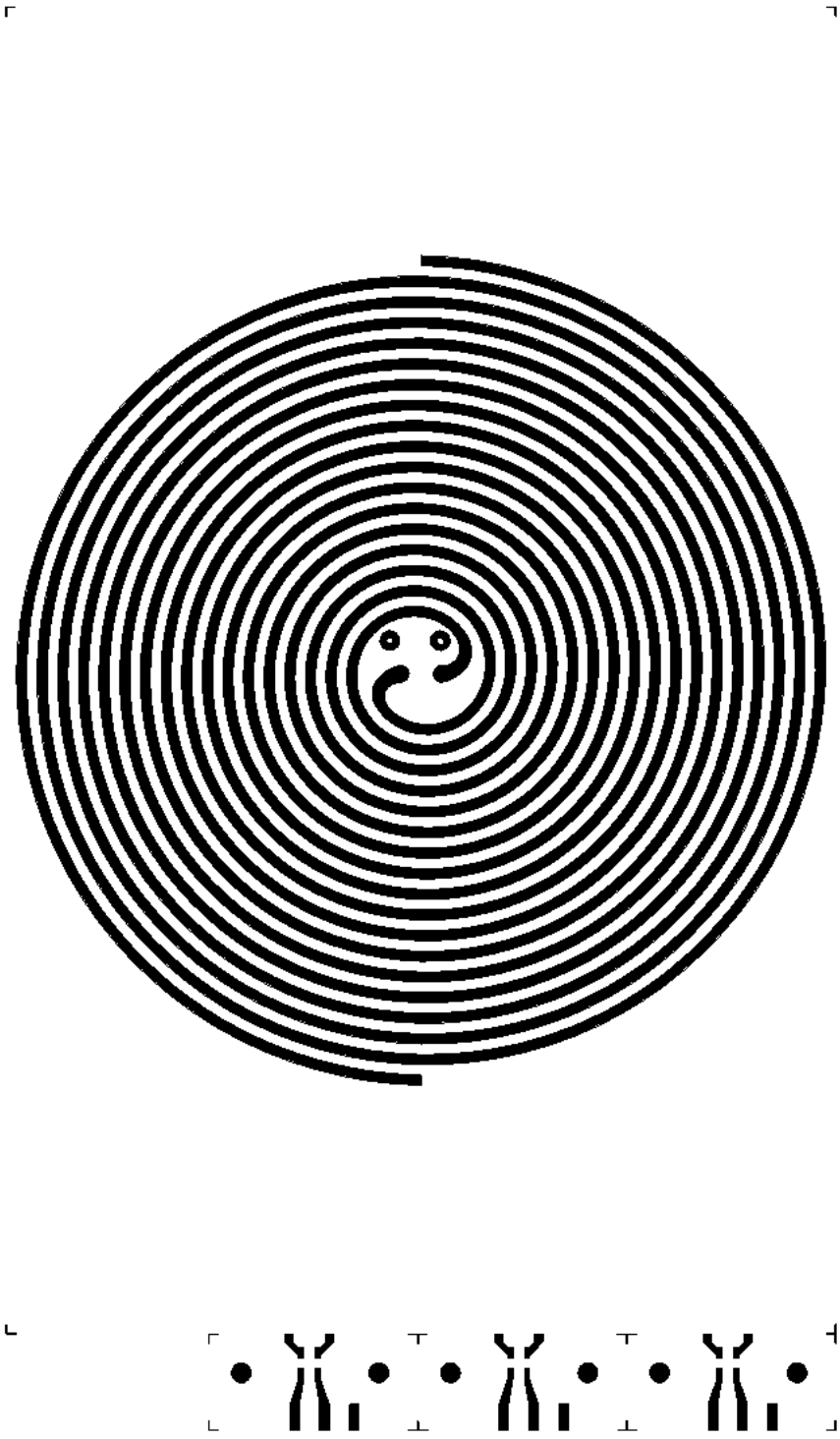

Figure 5.1: *Mask of the printed spiral, 50% rescaled.*

Bibliography

[1] P. Knott, "Design of a triple patch antenna element for double curved conformal antenna array," in *First European Conference on Antennas and Propagation (EuCAP)*, 2006.

[2] S. W. Qu and C. L. Ruan, "Effect of round corners on bowtie antennas," *Progress In Electromagnetics Research*, vol. PIER 57, p. 179 195, 2006.

[3] J. D. Kraus and R. J. Marhefka, *ANTENNAS For All Applications*, 3^{rd} ed. McGraw-Hill Companies, 2002.

[4] W. Stutzman, "Wide bandwidth antenna array design," in *Proc. IEEE Southeastern Regional Meeting*, Raleigh, NC, April 1985, pp. 92–96.

[5] J. D. Müller and K. Sarabandi, "Design and analysis of a 3-arm spiral antenna," *AP*, vol. 55, pp. 258–266, feb. 2007.

[6] K. Louertani, "Etude d'une solution coplanaire pour antenna spirale," Master Thesis, University Pierre et Marie Curie, Paris 6, SONDRA Lab., France, April-July 2007.

[7] O. Bucci, G. Francetti, G. Mazzarella, and G. Panariello, "Intersection approach to array pattern synthesis," *AP*, vol. 137, pp. 467–471, Dec. 1990.

[8] P. A. Buxbaum, "Surveillance from the stratosphere," *Military Aerospace Technology*, vol. 5, Apr. 19 2006. [Online]. Available: http://www.military-aerospace-technology.com/article.cfm?DocID=1410

[9] J. YANG, "Building a 21st century military with 19th century technology army defense agency spending millions to develop 'high altitude airships'," *ABC News*, Aug. 8 2006. [Online]. Available: http://abcnews.go.com/US/Story?id=2286835&page=2

[10] J. Wilson, "A new era for airships," *Aerospace America*, pp. 27–31, May 2004. [Online]. Available: http://www.aiaa.org/aerospace/images/articleimages/pdf/wilsonmay04.pdf

[11] L.Corey, "Integrated sensor is structure," *Proposer information pamphlet, DARPA*, sept. 24 2003. [Online]. Available: http://www.darpa.mil/DARPAtech2004/pdf/scripts/CoreyScript.pdf

[12] MyAirship, "http://www.myairship.com," 2007.

[13] Airship-Association, "http://www.airship-association.org/," 2007.

[14] Goodyear, "http://www.goodyearblimp.com/," 2007.

[15] Airshipvision, "http://www.airshipvision.org," 2007.

[16] Wikipedia, "http://en.wikipedia.org/wiki/airship," 2007.

[17] DefenseTech, "http://www.defensetech.org/archives/000816.html," 2007.

[18] B. W. G. Miner and D. Arnold, "A low cost, radio controlled blimp as a platform for remote sensing," in *Geoscience and Remote Sensing Symposium. Proceedings. IGARSS. IEEE 2000 International*, vol. 22, 2000, pp. 2308 – 2309.

[19] Voliris, "http://www.voliris.com," 2007.

[20] M. L. VanBlaricum, J. P. Reilley, M. A. Gilbert, G. F. VanBlaricum, D. C. Gammon, D. P. Cadogan, R. W. Lingo, M. S. Grahne, and W. C. Derbes, "Quick feasibility demonstration for an inflatable antenna system in space," in *Proc. of the 9th annual DARPA symposium on Photonic system for Antenna application*, Monterey, CA, feb. 1999.

[21] N. Herscovici, Z. Sipus, and S. Kildal, "The cylindrical omnidirectional patch antenna," *AP*, vol. 49, pp. 1746 – 1753, Dec 2001.

[22] R. Munson, "Conformal microstrip antennas and microstrip phased arrays," *AP*, vol. 22, pp. 74– 78, Jan. 1974.

[23] G. Caille, E. Vourch, M. Martin, J. Mosig, and M. Polegre, "Conformal array antenna for observation platforms in low earth orbit," *AP*, vol. 44, pp. 103–104, June 2002.

[24] P. Persson, L. Josefsson, and M. Lanne, "Investigation of the mutual coupling between apertures on doubly curved convex surfaces: Theory and measurements," *AP*, vol. 51, pp. 682–692, Apr. 2003.

[25] L. Josefsson and P. Persson, *Conformal Array Antenna Theory and Design*. Wiley-IEEE Press, 2006.

[26] R. Mailloux, *Phased Array Antenna Handbook*, 2nd ed. Artech House, june 2005.

[27] A. Munger, G. Vaughn, J. H. Provencher, and B. R. Gladman, "Conical array studies," *AP*, vol. 22, pp. 35–43, Jan 1974.

[28] EWCA, Ed., *Proceedings of First European workshop on Conformal Antennas*, Karlsruhe, Germany, 29 oct. 1999.

[29] A. Gustafsson, R. Malmqvist, L. Pettersson, and et al., "A very thin and compact smart skin x-band digital beamforming antenna," in *Proc. Radar Conference EURAD. First European Volume*, 2004, pp. 313–316.

[30] A. W. Rudge, *The Handbook of Antenna Design*. London: Peter Peregrinus, 1983, vol. 2.

[31] L. Josefsson and P. Persson, "An analysis of mutual coupling on doubly curved convex surfaces," in *Antennas and Propagation Society International Symposium*, 2001, pp. 342–345.

[32] A. Alu, F. Bilotti, and L. Vegni, "Method of lines numerical analysis of conformal antennas," *AP*, vol. 52, pp. 1530–1540, june 2004.

[33] V. B. Erturk, R. G. Rojas, and K. W. Lee, "Analysis of finite arrays of axially directed printed dipoles on electrically large circular cylinders," *AP*, vol. 52, pp. 2586–2595, Oct. 2004.

[34] L. Vegni and A. Toscano, "The method of lines for mutual coupling analysis of a finite array of patch antennas on a cylindrical stratified structure," *AP*, vol. 51, pp. 1907–1913, Aug. 2003.

[35] A. Ioffe, M. Thiel, and A. Dreher, "Analysis of microstrip patch antennas on arbitrarily shaped multilayers," *AP*, vol. 51, pp. 1929–1935, Aug. 2003.

[36] P. Persson and L. Josefsson, "Calculating the mutual coupling between apertures on a convex circular cylinder using a hybrid utd-mom method," *AP*, vol. 49, pp. 672–677, Apr. 2001.

[37] B. Thors and L. Josefsson, "Radiation and scattering tradeoff design for conformal arrays," *AP*, vol. 51, pp. 1069–1076, May 2003.

[38] U. Jakobus and F. M. Landstorfer, "Improved PO-MM hybrid formulation for scattering from three-dimensional perfectly conducting bodies of arbitrary shape," *AP*, vol. 43, pp. 162–169, Feb. 1995.

[39] O. Bucci, A.Capozzoli, Dapos, and G. Elia, "Power pattern synthesis of reconfigurable conformal arrays with near-field constraints," *AP*, vol. 52, pp. 132 – 141, Jan. 2004.

[40] F. Obelleiro, L. Landesa, J. Taboada, and J.L.Rodriguez, "Synthesis of onboard array antennas including interaction with the mounting platform and mutual coupling effects," *AP*, vol. 43, pp. 76–82, Apr. 2001.

[41] D. Werner, R. Allard, R. Martin, and R. Mittra, "A reciprocity approach for calculating radiation patterns of arbitrarily shaped microstrip antennas mounted on circularly cylindrical platforms," *AP*, vol. 51, pp. 730 – 738, Apr. 2003.

[42] T. Dissanayake and K. Esselle, "Assessment of antenna performance for ultra-wideband systems," in *Proc. EUCAP (European Conference on Antenas and Propagation)*, Nice France, Nov. 2006.

[43] H. G. Shantz, "Introduction to ultra-wideband antennas," in *Proc. IEEE UWBST Conference*, 2003.

[44] ——, "A brief history of uwb antenna," in *Proc. IEEE UWBST Conference*, 2003.

[45] M. Bonnedal, E. Angelopoulos, E. Antonino, P. Balling, K. Chan, R. Erickson, I. Lager, M. Mazanek, W. Srgel, E. Ubeda, and A. Yarovoy, "Activities in ACE WP 2.3-1 on wideband and multiband radiators," in *Proc. EUCAP (European Conference on Antennas and Propagation)*, Nice, France, Nov. 2006.

[46] A. Eldek, A. Elsherbeni, and C. Smith, "Wideband bow-tie slot antenna with tuning stubs," in *Radar Conference, 2004. Proceedings of the IEEE*, 2004, pp. 583–588.

[47] S. Suh, "A comprehensive investigation of new planar wideband antennas," Ph.D, Virginia Polytechnic Institute, Blacksburg, Virginia, July 2002. [Online]. Available: http://scholar.lib.vt.edu/theses/available/etd-08262002-183120/unrestricted/PHD_DISSERTATION_SUH.pdf

[48] R. F. Harrington and J. R. Mautz, "Theory of characteristic modes for conducting bodies," *AP*, vol. 19, pp. 622–628, Sept. 1971.

[49] M. F. Bataller, M. Cabedo-Fabrés, E. Antonino-Daviu, and A. Valero-Nogueira, "Overview of planar monopole antennas for uwb applications," in *Proc. EUCAP (European Conference on Antenas and Propagation)*, Nice France, Nov. 2006.

[50] N. Cohen, "Fractal antennas part 1," *Communications Quarterly*, pp. 5–236, Summer 1995.

[51] J. Romeu and J. Soler, "Generalized Sierpinski fractal multiband antenna," *AP*, vol. 49, Aug. 2001.

[52] R. H. Duhamel and D. E. Isbell, "Broadband logarithmically periodic antennas structures," in *IRE National Convention Record Part 1*, 1957, pp. 119–128.

[53] Y. Mushiake, "A report on japanese development of antennas: From the Yagi-Uda antenna to self-complementary antennas," *AP*, vol. 46, pp. 47–59, Aug. 2004.

[54] V. H. Rumsey, *Frequency Independent Antennas.* Academic Press, 1966.

[55] R. H. Duhamel, "Dual polarized sinuous antennas," United States Patent 5,146,234, Apr. 14 1987.

[56] M. Buck and D. Filipovic, "Analysis and design of a multiband, multipolarized two-arm sinuous antenna," in *Proc. 22nd Annual Review of Progress in Applied Computational Electromagnetics(ACES)*, Miami, USA, 2006.

[57] R. G. Corzine and J. A. Mosko, *Four-Arm Spiral Antennas.* Norwood: Artech House, 1990.

[58] J. Huffman and T. Cencich, "Modal impedances of planar, non-complementary, N-fold symmetric antenna structures," *AP*, vol. 47, pp. 110–116, Feb. 2005.

[59] D. King, R. Packard, and R. Thomas, "Unequally-spaced, broad-band antenna," *AP*, vol. 8, pp. 380–385, July 1960.

[60] A. Ishimaru, "Theory of unequally-spaced arrays," *IRE Trans. Antennas Propagat.*, vol. 10, pp. 691–702, Nov. 1962.

[61] J. Boyns and J. Provencher, "Experimental results of a multifrequency array antenna," *AP*, vol. 20, pp. 106–107, Jan. 1972.

[62] L. Pringle, P. Harms, S. Blalock, G. Kiesel, E. Kuster, P. Friederich, R. Prado, J. Morris, and G. Smith, "A reconfigurable aperture antenna based on switched links between electrically small metallic patches," *AP*, vol. 52, pp. 1434–1445, June 2004.

[63] E. Caswell, "Design and analysis of star spirals with application to wideband arrays with variable element sizes," Ph.D, Virginia Polytechnic Institute, Blacksburg, VA, December 2001. [Online]. Available: http://scholar.lib.vt.edu/theses/available/etd-01082002-073223/

[64] R. S. Elliot, *Antenna Theory and Design*, Revised ed. Piscataway: IEEE press, Wiley-interscience, 2003.

[65] FEKO, *EM Software & Systems-S.A.*, 32 Techno lane, Technopark, Stellenbosch, 7600 South Africa, 2004.

[66] R. C. Hansen, *Microwave scanning antennas. Vol. III, Array systems.* 111, 5th Avenue, New York: Academic press, 1966.

[67] J. K. Hsiao and A. G. Cha, "Patterns and polarizations of simultaneously excited planar arrays on a conformal surface," *AP*, vol. 45, pp. 81–84, jan. 1974.

[68] R. J. Allard, D. H. Werner, and P. L. Werner, "Radiation pattern synthesis for arrays of conformal antennas mounted on arbitrarily shaped three-dimensional platforms using genetic algorithms," *AP*, vol. 51, p. 1054 1062, May 2003.

[69] D. W. Boeringer and D. H. Werner, "Particle swarm optimization of a modified Bernstein polynomial for conformal array excitation amplitude synthesis," *AP*, vol. 53, p. 2662 2673, Aug. 2005.

[70] J. A. Ferreira and F. Ares, "Pattern synthesis of conformal arrays by the simulated annealing technique," *Electronics Letters*, vol. 33, pp. 1187–1189, July 1997.

[71] L. I. Vaskelainen, "Iterative least-squares synthesis methods for conformal array antennas with optimized polarization and frequency properties," *AP*, vol. 45, p. 1179 1185, July 1997.

[72] ——, "Constrained least-squares optimization in conformal array antenna synthesis," *AP*, vol. 55, pp. 859–867, March 2007.

[73] P. Knott, "Antenna modelling and pattern synthesis method for conformal antenna arrays," in *Antennas and Propagation Society International Symposium*, vol. 1, June 2003, pp. 800–803.

[74] H. Steyskal, "Pattern synthesis for a conformal wing array," in *Aerospace Conference Proceedings, 2002. IEEE*, vol. 2, 2002, pp. 819–824.

[75] L. Josefson and P. Persson, "Conformal array synthesis including mutual coupling," *Electronics Letters*, vol. 35, pp. 625–626, Apr. 1999.

[76] J. Gu, H. Stark, and Y. Yang, "Wide-band smart antenna design using vector space projection methods," *AP*, vol. 52, pp. 3228–3236, Dec. 2004.

[77] P. G. Elliot, "Conformal array beam synthesis and taper efficiency comparisons," in *Antennas, Radar, and Wave Propagation, ARP 2005, Banff, Alberta, Canada*, 2005.

[78] R. Guinvarc'h, "Dual polarisation wide-band interleaved spiral antenna array," in *RADAR 2007*, Edinburgh, UK, Oct. 2007.

[79] R. Haupt, "Interleaved thinned linear arrays," *AP*, vol. 53, pp. 2858–2864, Sept. 2005.

Abstract

High Altitude Airships (HAA) staying at 20km above earth's surface are currently under development in several countries. Indeed, airships seem to be an attractive solution to provide large platforms for remote sensing and telecommunication application at lower cost than satellites. In our study, the feasibility of using a smaller size commercial airship as a host platform for an antenna array is investigated, where the array is directly mounted on the airship hull. The array must be conformal, low weight and low profile and cannot use ground plane. The first issue concerns the choice of a device that fulfils both the wideband and the low level of cross-polarization performance requirements. Performances are evaluated using a commercial modeling tool and validated by measurement of a prototype. The second issue concerns the modeling of a large conformal array, which is too computationally intensive. The interactions of the antenna array with the platform are analyzed and quantified. Then an approximated method is developped and validated through comparisons with the exact method and the measurements. Finally, the feasibility of the pattern synthesis is investigated. Particular attention is paid to the polarization in a conformal configuration mechanism. The unique features of the platform, and both the array shape and the element polarization diversity serve the dual-polarization pattern synthesis.

Keywords: conformal antennas, phased-array, wideband, dual-polarization, spiral antenna, radar, airship

Résumé

Des dirigeables volant à 20 km au-dessus du sol (HAA: High altitude airship), sont actuellement en cours de développement dans plusieurs pays. Ce type de dirigeable semble être une solution très intéressante pour la télédétection et les télécommunications à faibles coûts comparé aux satellites. Notre étude porte sur la possibilité d'utiliser un dirigeable commercial de plus petite taille comme plateforme pour un réseau d'antennes posé directement sur son enveloppe. Le réseau doit être conforme, léger et compact et sans plan de masse. Le premier problème concerne le choix de l'élément de réseau permettant des performances large bande et bipolarisation. Un logiciel de modélisation est utilisé pour choisir l'antenne la plus performante et les résultats sont ensuite comparés à des mesures. L'alimentation des antennes sur le dirigeable est également discutée et une solution est proposée. Le deuxième problème concerne la modélisation d'un réseau conformé très large, très long à calculer avec le logiciel commercial. Les interactions à l'intérieur du réseau sont donc analysées et quantifiée. Puis, une méthode approchée est développée et validée par comparaison avec la méthode exacte et les mesures. Enfin, les possibilités de dépointage du réseau sont étudiées et évaluées. Les mécanismes de polarisation, dans la configuration conforme, sont analysés en profondeur. Ainsi, la synthèse de diagramme bipolarisation peut être réalisée grâce la spécificité du réseau conforme et la diversité de polarisation introduite par l'élément.

Mots clés: antennes conformes, réseau phasé, large bande, bipolarisation, antenne spirale, radar, dirigeable